NATIONAL INSTITUTE FOR FUSION SCIENCE

New Developments of Plasma Science with
Pulsed Power Technology
Mar. 5-6, 2009, NIFS

Eds. K. Kamada and T. Ozaki

(Received - Mar. 13, 2010)

NIFS-PROC-82   Mar. 17, 2010

RESEARCH REPORT
NIFS-PROC Series

TOKI, JAPAN

New Developments of Plasma Science with Pulsed Power Technology

Edited by Keiichi Kamada and Tetsuo Ozaki

March 5-6, 2009

National Institute for Fusion Science

Toki, Gifu, Japan

Abstract

In this proceedings, the papers presented at the symposium on "New developments of Plasma Science with Pulsed Power Technology" held at National Institute for Fusion Science on March 5-6, 2009 are collected. The papers reflect the present status and recent progress in the experimental and theoretical works on plasma science using pulsed power technology.

Editor's Preface

The symposium on "New developments of Plasma Science with Pulsed Power Technology" was held at National Institute for Fusion Science on March 5-6, 2009. Around 45 scientists from universities and institute joined in fruitful discussions in the symposium. Sixteen papers presented at the symposium are included in this proceedings.

The origin of this symposium can be traced back to two workshops started around 1978 at Institute of Plasma Physics, Nagoya University. One is the workshop on plasma focus organized by Prof. M. Yokoyama (Osaka University). And another workshop on intense pulsed particle beams organized by Prof. K. Niu (Tokyo Institute of Technology) and Prof. K. Yatsui (Nagaoka University of Technology) was originated from the joint experimental research using LIMAY-1. In 1992, two workshops were joined to the workshop of pulsed power and high density plasma organized by Prof T. Tazima (National Institute for Fusion Science). This workshop holds the 2 days symposium every year on the physics of high density plasmas and its applications using pulsed power technology including z-pinch, plasma focus, laser, intense particle beams etc. Around 40-50 scientists and students from 10-12 university etc. attend the symposium every year. Almost 20-25 presentations are given in a symposium and they are published NIFS-PROC since 1990.

Keiichi Kamada
Kanazawa University

Tetsuo Ozaki
National Institute for Fusion Science

Contents

List of participants

K. Takasugi	(Nihon University)
T. Yoshinaga	(Nihon University)
A. Maeda	(Nihon University)
T. Ohshima	(Nihon University)
M. Nishio	(Nihon University)
K. Horioka	(Tokyo Institute of Technology)
Y. Aoyama	(Tokyo Institute of Technology)
Y. Otsuka	(Tokyo Institute of Technology)
E. Hotta	(Tokyo Institute of Technology)
Y. Sasaki	(Tokyo Institute of Technology)
J. Kikuchi	(Tokyo Institute of Technology)
G. Imada	(Niigata Institute of Technology)
S. Furuya	(Gunma University)
Y. Uehara	(Gunma University)
T. Miyake	(Gunma University)
Y. Arai	(Gunma University)
A. Watanabe	(Gunma University)
M. Sato	(Gunma University)
M. Akiyama	(Kumamoto University)
H. Akiyama	(Kumamoto University)
T. Sakugawa	(Kumamoto University)
S. Katsuki	(Kumamoto University)
M. Yano	(Kumamoto University)
S. Kawata	(Utsunomiya University)
P. Wang	(Utsunomiya University)
T. Higashiguchi	(Utsunomiya University)
H. Terauchi	(Utsunomiya University)
H. Ito	(University of Toyama)
K. Masugata	(University of Toyama)
Z. P Wang	(University of Toyama)
K. Sugawara	(University of Toyama)
Y. Ochiai	(University of Toyama)
T. Kawashima	(National Institute for Fusion Science)
T. Ozaki	(National Institute for Fusion Science)
T. Tazima	(National Institute for Fusion Science)
Y. Soga	(Kanazawa University)
R. Ando	(Kanazawa University)
S. Odawara	(Kanazawa University)
F. Kondo	(Kanazawa University)
K. Tamura	(Kanazawa University)
T. Kurihara	(Kanazawa University)
K. Nose	(Kanazawa University)

T. Hoshiba   (Kanazawa University)
K. Misawa   (Kanazawa University)
S. Yanagi   (Kanazawa University)
K. Kamada   (Kanazawa University)

FIELD-DEFLECTION ANALYSIS OF ACCELERATED IONS IN THE DIVERGENT GAS-PUFF Z PINCH

M. Nishio, K. Takasugi* and H. Sakuma

College of Science and Technology, Nihon University, Tokyo 101-8308, Japan
* Institute of Quantum Science, Nihon University, Tokyo 101-8308, Japan

ABSTRACT

The energies of the accelerated Ar ions in the divergent gas-puff z pinch were measured with the simple field-deflection analyzer in order to explain indirectly the electron acceleration causing 250-keV hard x-ray. The model of pulsed inductive electromotive force I(dL/dt) induced by the m=0 instability was assumed as the most simple acceleration mechanism. The solid-state detector was arranged for reducing noises and the secondary-electron signals. The deflection experiments with given two electric-field-setups provided in similar results. Energies of accelerated Ar ions were likely to be lower than that of the obtained hard x-ray, even at the highest-temperature condition.

I. Introduction

Axially-homogeneous distributions of the injected neutral gas are required to achieve the uniform plasmas in the conventional gas-puff z pinches. Some hot spots, which are high-temperature and high-density plasma regions, would spot on the electrode axis in the axially-uniform condition. Plasma focus as the sterically-compressed plasma-production technique can produce the more local compression and the axially-directed plasma jets. Because the plasma focus is initiated by surface flashover, the current restriction by the pinch causes to produce another discharge path. The input energy to the plasmas produced by plasma focus technique is limited due to the re-discharge.

The gas-puff z pinch experiments with the divergent cylindrical gas nozzle have been reported in 2007 at first [1]. They produced the focused high-temperature and high-density hot spots by using hollow conical-shape Ar gas with the 10-degree divergent gas nozzles. The hot spots localization with the divergent gas puff could have been affected by the dissymmetry of the neutral gas distribution (see Fig.1). The injected energy to the plasma increased 40% compared with the conventional z pinches (0-degree gas nozzle). The most characteristic result of them is the hard x-ray emissions on the metal anode. The x-ray energy was approximately ten times higher than the charged voltage of the capacitor bank. The hard x-ray would be recognized as the Bremsstrahlung radiation caused by the impact processes between electrons and the metal electrode.

There must be some acceleration mechanism of electrons in the divergent gas-puff z pinch for the 250keV hard x-ray radiation. High-energy accelerations (high energy neutron or hard x-ray) with discharge have been also observed in the conventional discharge [2] or plasma focus
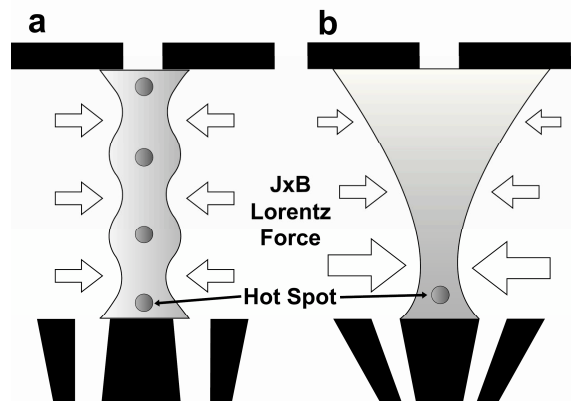
Fig. 1: (a) Conventional gas-puff z pinch configuration. Neutral gas is injected between anode and cathode electrodes with 0-degree nozzle angle. Axially-uniform gas distribution is required for scattered hotspots on the electrode axis. (b) Divergent gas-puff z-pinch configuration. Localization of hotspots is achieved by the dissymmetry of the puffed gas.

experiments [3] and so on. Although some models [4-7] are discussed, the consensus for the mechanism has not been obtained. It is not apparent whether or not acceleration mechanism of electrons in our previous work [1] is similar to that of another discharge experiments. If not similar, the difference of the divergent gas-puff experiments must be discussed with spatial and temporal distribution of the accelerated particles, plasma dynamics of divergent configuration and changes of discharge parameter.

In order to reveal the energy distribution of accelerated particles with the pinch as an entry-level experiment, we attempted to measure the deflected distance of the accelerated particles against the applied field. In this study, the model of pulsed inductive electromotive force induced by the m=0 instability [3] is assumed as the most simple acceleration mechanism. Because the direct measurements of electrons are difficult due to the design of the system, the oppositely-accelerated ion was trapped by the solid state track detector in this study.

II. Acceleration mechanism of particles

Ions have been assumed simply to be accelerated by the strong axial electric field in some pulsed power discharge. The pulsed inductive electromotive force is generated essentially due to the rapid increase of current or that of plasma inductance. Considering the z pinch as the LCR equivalent circuit, the voltage between the electrodes denotes from the circuit equation as follows.

$$V(t) = L\frac{dI(t)}{dt} + I\frac{dL(t)}{dt} + RI(t) , \qquad (1)$$

where V(t), I(t), L(t) and R show voltage, current, inductance and resistance. The first term of right side value shows the inductive voltage with time rate of current. The second term of that shows the one with time rate of inductance. Both the first term and the second one exceed the stored voltage in the capacitor bank. In the case of the rapid increment of current, the MV class voltage was achieved by using plasma opening switching [8]. In our z-pinch experiments the latter increase of inductance is considered to be more important, because the produced plasma implodes rapidly radially.

Figures 2a and 2b show the conceptual diagram of rapid current increase and the voltage induced by it, which are corresponding to the first term of eq, (1). Figures 2c and 2d show the rapid increase of inductance and the voltage caused by it, which are corresponding to the second term of eq. (1). Here L_c and L_p shows the constant of circuit inductance and the variant of plasma inductance (function of radius), respectively. In the dynamical increase of L_p by pinch (t=t_1) with the m=0 instability, the pulsed inductive voltage is applied to the pinching area. If the time scale of the generated voltage pulse is assumed to be

similar to that of pinch phenomena, the time interval would be between a few nsec and a few tens of nsec. Because the plasma inductance would not change during the stagnation stage on the z axis, the inductive voltage would decrease and turn to be negative (t=t_2) in the expansion stage. As the half cycle of discharge current sin wave is approximately 5 μsec in our usual experiments, the increase in the plasma inductance is kept until the disruption stage caused by fluid instability.

The inductance of plasma column L_p(t) is calculated from the LCR circuit equation, as the
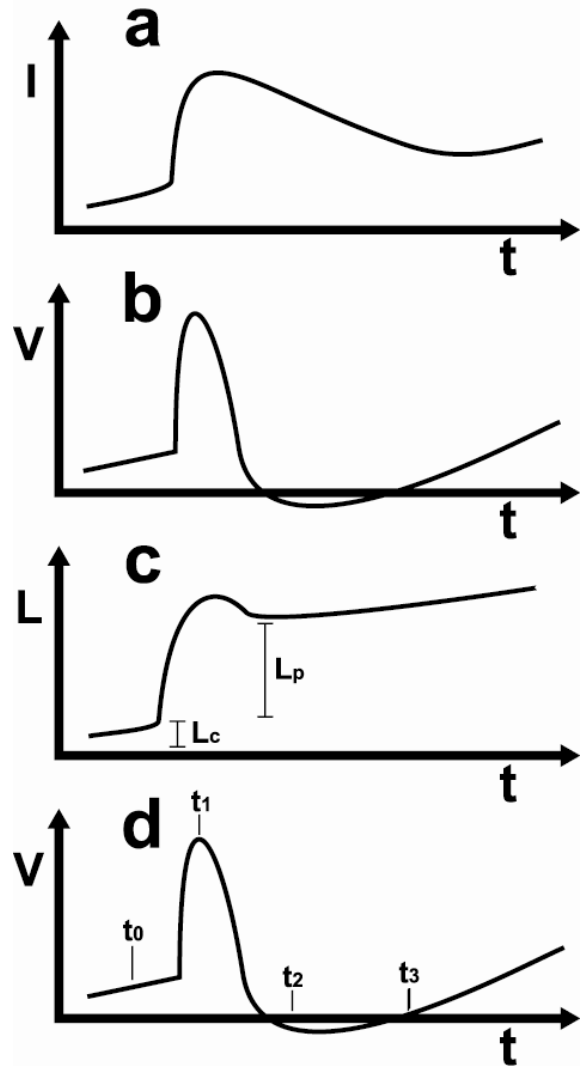
Fig. 2: (a) Rapid increment of current corresponding to dI(t)/dt. (b) Induced increase of voltage caused by current increase corresponding to LdI(t)/dt. (c) Rapid increment of inductance corresponding to dL(t)/dt. Lc and Lp shows the constant of circuit inductance and the variant of plasma inductance (function of radius), respectively. (d) Induced increase of voltage caused by inductance increase corresponding to IdL(t)/dt.

discharge circuit is assumed to be coaxial transmitting line [9]. When the radius implosion of z-pinch plasma is treated as the decrement of inner diameter of coaxial line, the inductance at load is given by

$$L_p(t) = L - L_c = \frac{\mu_0 l}{2\pi} \ln \frac{r_0}{r(t)}, \qquad (2)$$

where L, L_c, μ_0, l, r_0 and $r(t)$ show inductance of system, inductance of circuit, magnetic permeability, length of load, characteristic radius of the outer current path and radius of pinch plasma, respectively. Plasma inductance increases with growing radius implosion, and becomes the maximum at the pinch (the most compressed). Inductive electromotive force V_p of the second term of eq. (1) is calculated by using the differentiation of eq. (2) with time.

$$V_p = I \frac{dL(t)}{dt} = -\frac{\mu_0 l}{2\pi} \frac{I}{r(t)} \frac{dr(t)}{dt}. \qquad (3)$$

Because this voltage is attributed to the rapid increment of inductance during the current decrement in short time scale with the radius implosion of plasma, it is determined by only the plasma dynamics. Because this voltage pulse may be the reasonable candidate of the particle acceleration associated with pinch, we focused on the inductive voltage of the second term of eq. (1).

In order to estimate approximately the magnitude of the inductive electromotive force V_p, when typical parameters are assigned to the right side of eq. (3) as $I = 2 \times 10^5$ [A]、$l = 3 \times 10^{-2}$ [m]、$(1/r)dr/dt = -2 \times 10^8$ [/s], V_p is calculated to be 240 kV. The appropriate change rate of radius implosion is assumed in above estimation. However, the implosion rate is difficult to measure by using optical

system experimentally. In order to estimate of the magnitude of the inductive electromotive force V_p indirectly, the energy of the accelerated particles (ions) was measured in this study.

III. Experimental Procedures

The SHOTGUN-I z-pinch device at Nihon University was used as the high-voltage pulse-power supply. The energy storage section of the device consists of 30 kV 24 μF capacitor bank, and the maximum discharge current is 300 kA. The charged voltage of the bank was 25 kV (7.5 kJ) in this experiment. Details of experimental setups are similar to that of the previous work [1].

The isolated gas distribution can be formed between the electrodes with a high-speed gas valve and an annular Laval nozzle mounted on the anode [9]. Figure 1a shows the arrangements of electrodes in the usual z-pinch and the divergent gas-puff experiment. In the divergent gas-puff experiment (Fig. 1b), the hollow conical gas distribution was achieved by the divergent shaped Laval nozzle (ejection angle of 30-degree outward). The distance between the electrodes was 3 cm. Ar gas was used in this experiment, and the plenum pressure of the gas valve was 5 atm. Total discharge current was measured by the Rogowski coil located outside the chamber. Soft x-ray intensity was detected by x-ray diodes (XRDs) with Ni and Al photocathodes. The XRDs are more sensitive to high energy photons in this order. X-ray signal was detected by a scintillation probe (SCI) with a 10 μm Be filter. In order to measure high energy x-ray distribution around the device, an x-ray film cassette was prepared.

Accelerated Ar ion jets generated by pinch enable to escape from inter-electrodes into outside of
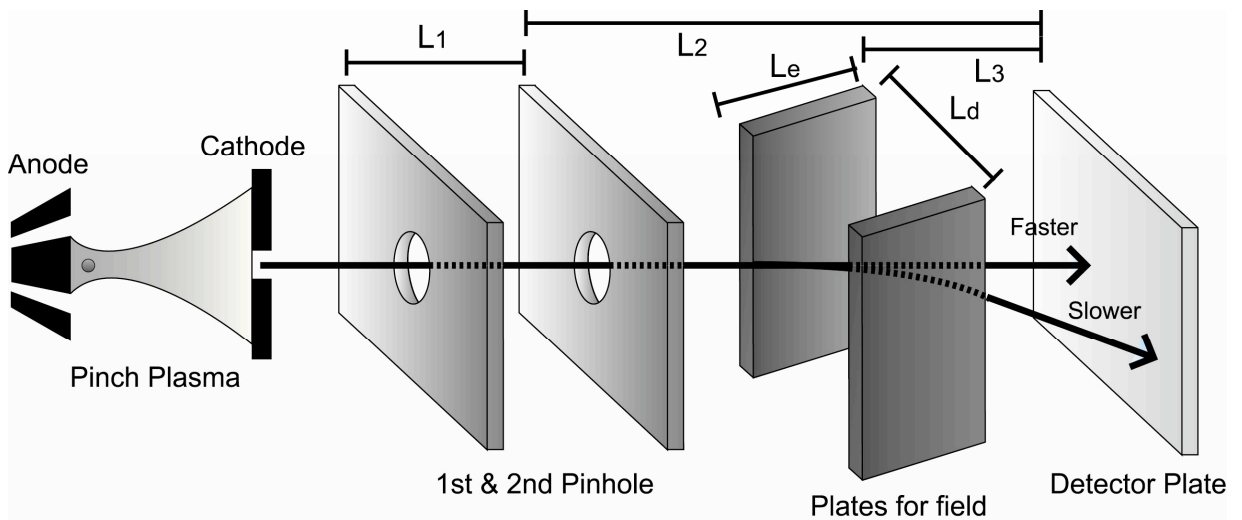
Fig. 3: Resulting injected ions through the two pinholes and are deflected by the applied electric field. Accelerated particles hit to the detector surface on the analyzer axis corresponding to the magnitude of energy. As the high energy ions impact the plate, it is etched during a proper interval for a visualization of particle tracks.

cathode. The energy of ions trapped with the detector is obtained by using field-deflection analysis [11, 12, 13]. The detector without electrical system can reduce noises and eliminate the secondary-electron signal induced by electromagnet wave [14, 15, 16]. Simple solid-state field-deflection analyzer was set up at the outer end on the discharge axis. Schematic arrangement of the analyzer is shown in Fig. 3. Resulting injected ions through the two pinholes, and hit to the detector surface after the deflection by the electric field. When the high energy ions impact the plastic plate "Baryotrak-P" (Nagase-Landauer Co., Ltd.), small invisible tracks would be generated on the surface. Those tracks become observable after etching with NaOH water solution. In order to estimate the ion energies, the deflection distances of ion tracks from the origin in the electric field (10 kV/m or 20 kV/m) were measured. Analyzer parameter are shown as follows: plate size; 30x30 [mm], distance between cathode and the plate; 800 [mm], first pinhole diameter D_1; 10 [mm], second pinhole diameter D_2; 1.2 [mm], distance between pinholes L_1; 10 [mm], distance between second pinhole and plate L_2; 110 [mm], distance between the field and plate L_3; 100 [mm], distance between electrodes L_d; 10 [mm], field length L_E; 25 [mm].

IV. Results

Typical current waveform and x-ray signals are shown in Fig. 4. When pinch happens, the current flow is limitted by necking of plasma column. XRDs and SCI signals by the radiation from hotspots occur around the pinch timing. Hard x-ray radiation as the direct result of the particle acceleration was also observed from metal area of the anode surface in this study (30-degree nozzle) as well as the previous study (10-degree nozzle) [1]. Figures 5a and 5b show x-ray film images through the pinhole. The soft x-ray radiations from hotspots (spotty) and metal anode (cloudy) are observed in Fig. 5a. The hard x-ray radiations from metal anode through the copper plate (thickness: 1mm) are observed in Fig. 5b. The energy of the hard x-ray in this study is not apparent as the measurement of x-ray adsorption with metal plate was not carried out.

The twelve plastic plates detecting ion tracks were recovered in this study. The typical ion track distributions on the etched detector surface are shown in Fig. 6. Figure 6a shows the plate when the applied voltage to the electrodes is 100 V over 30 shots. Figure 6b shows the plate at 200V over 30 shots. In both Figs. 6a and 6b, two concentrated area of ion tracks were observed. Point A would be the origin of the analyzer, where the neutral particles should have hit. Point B would be the ion track deflected by the each fields. The deflection distance with the fields of 10 kV/m and 20 kV/m (distance between electrodes L_d; 10 mm) are measured to be 5 mm and 8 mm,
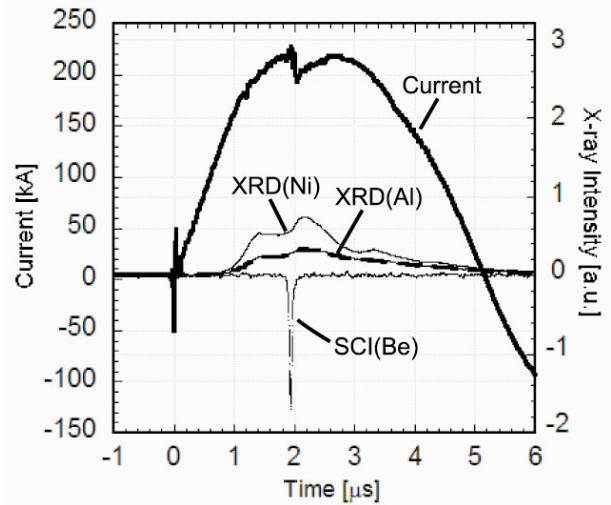
Fig. 4: Typical current waveform and x-ray signals.
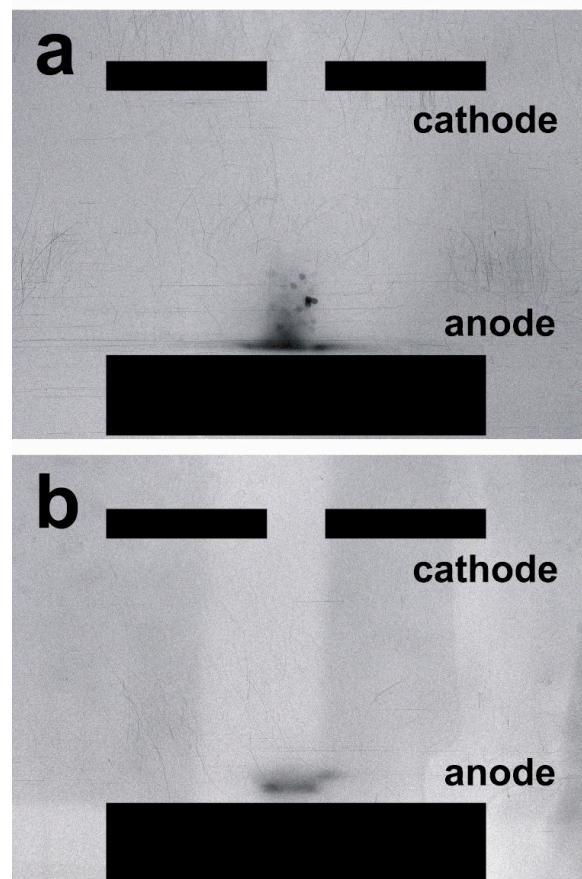
Fig. 5: X-ray film images through the pinhole. Distance between anode and cathode is 0.03 m. (a) Soft x-ray radiations from hotspots (spotty) and metal anode (cloudy) over 30 shots. (b) Hard x-ray radiations from metal anode through the copper plate (thickness : 1mm) in the same discharge with (a).

4

respectively. Those deflection distance will be used later to calculate the ion velocities and energies.

V. Discussions

The estimation of charge is needed for the energy calculation of accelerated ions. The temperature of Ar plasma generated by SHOTGUN-I z-pinch device was reported previously from the x ray spectroscopy [16]. They showed that dominant radiation in z-pinch experiment with Ar filling gas was Ar XVII (16+), Ar XVI (15+) and Ar XV (14+), and that the highest temperature of the produced plasma was between 0.6 and 1.3 keV. The temperature, however, denotes not bulk plasma which represent the entire plasma but hotspots which have highest one. Although only the upper limit of charges was set to be Ar^{16+}, the following closing-shell species of Ar ion is used as the dominant ion in each energy calculation.

As the accelerated ions were deflected from point A to point B on the plate surface by the electric field, the deflection distance are shown by

$$z = \frac{Ze}{Am_p} \frac{1}{v^2} EL_3 L_E, \qquad (4)$$

where Z, e, A, m_p, v, E, L_3 and L_e are charge number, elementary charge, mass number, unit nucleus mass, velocity, electric field intensity, distance between the field and plate and field length [10]. If the charge states of ions were assumed to be the three types Ar^{16+}, Ar^{8+} and Ar^{2+}, the corresponding ion energy can be calculated from eq. (4). The accelerated ion energies in the fields of 10 kV/m with different ion species were calculated to be 130 keV, 70 keV and 15 keV. In the fields of 200 kV/m, the energies were 170 keV, 80 keV and 20 keV. These energies are likely to be lower than that of the obtained hard x-ray, even at the highest temperature. However, it may be difficult to accelerate ions up to the same energy with 250-keV electrons due to its mass in the given interval. This could reveal only occurrence of the some kind of acceleration in the divergent z pinch experiments as
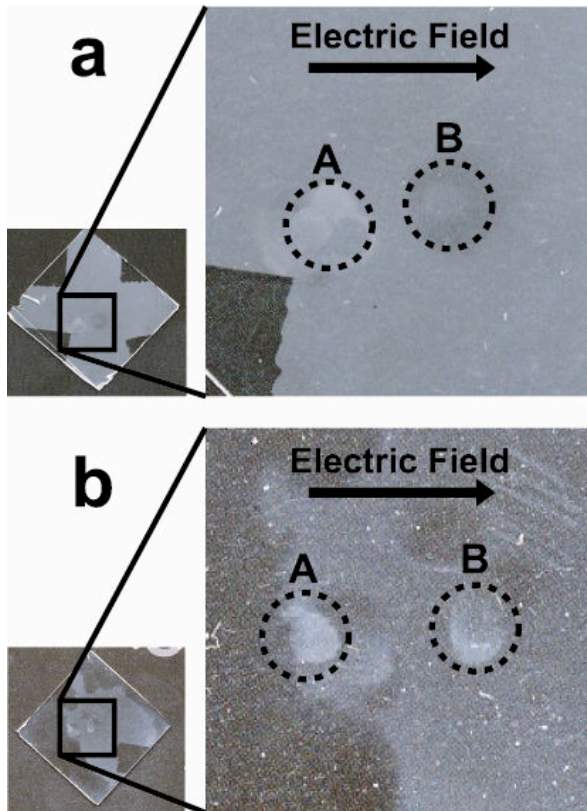
Fig. 6: Visible image of the detector plates which ions hit over 30 shots. In both images, electric fields were applied from leftside to rightside. Dashed circles show concentrated area of ion tracks. Point A would be the origin of the analyzer, where the neutral particles should have hit. Point B would be the ion track deflected by the each fields. (a) Plate when the applied voltage to the electrodes is 100 V. (b) Plate when the applied voltage to the electrodes is 200 V.
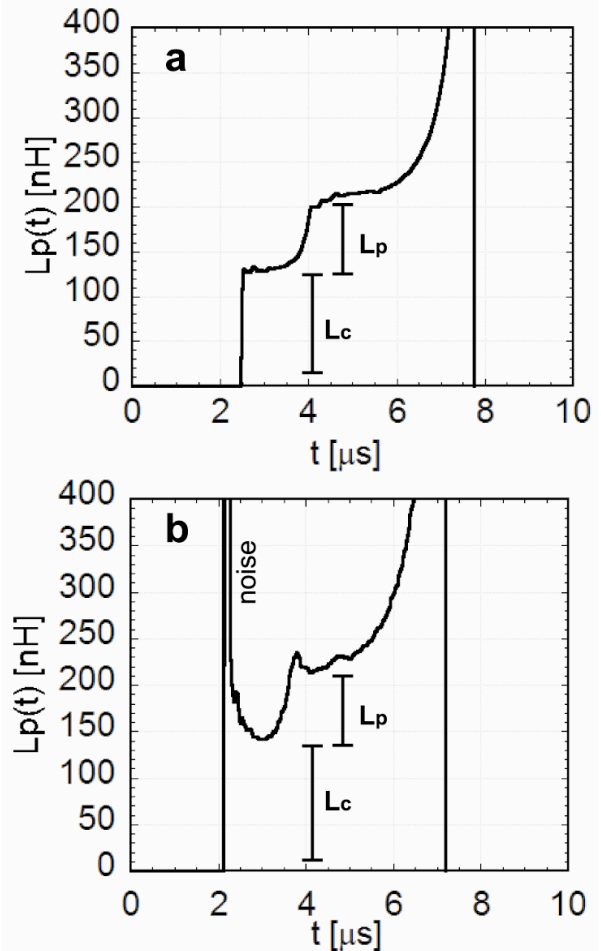
Fig. 7: Time change of calculated inductance from current waveform. The waveform data of the previous study [1] was used for the calculation of practical voltages. (a) In the conventional z pinch. (b) In the divergent z pinch (10 deg).

5

well as the previous discharge experiments. The validity of the model of the inductive electromotive force as the acceleration mechanism would warrant further discussion, even if the accelerated ions from highest temperature areas are assumed to be dominant.

As the source of high-energy ions and detailed ion energies are not determined in this study, the finding technique of ion source is needed for evolutionary deployment. The practical inductive electromotive force can be approximately estimated from the analysis of given current waveform of z pinch discharge. The waveform data of the previous study [1] was used for the calculation of practical voltages. The inductive electromotive force can be numerically obtained by the integral of current (voltage) divided by current of the moment. In Figs. 7a and 7b show the time change of inductance in the conventional z pinch and in the divergent z pinch (10 deg). The inductive voltage due to the increment of plasma inductance in each case was calculated to be 25.2 kV and 28.2 kV. Those magnitudes are much lower than that of required voltage for 250-keV hard x-ray. Rapid decrement of discharge current may have not detected because of the time resolution of used Rogowski coil. Direct measurement of the discharge voltage with pinch is required as further experiments.

VI. Conclusion

The energies of the accelerated Ar ions in the divergent gas-puff z pinch were estimated from simple field-deflection analysis in this study. This study could reveal only occurrence of the some kind of acceleration in the divergent z pinch experiments. The analyzed inductive electromotive force from the field-deflected experiments was lower than electrons producing 250-keV hard x-ray even if the ions generated from highest temperature areas were assumed to be dominant. More detailed analysis by using magnetic field as well as the electric field is needed for the determination of ion species.

References

1) K. Takasugi and E. Kiuchi, "Hard X-Ray Radiation from a Z-Pinch with a Divergent Gas-Puff", Plasma Fusion Res. Rapid Commun., Vol. 2, 036. (2007)

2) J. Fukai and E. J. Clothiaux, "Mechanism for the Hard x-ray Emission in Vacuum Spark Discharges", Phys. Rev.Lett., Vol. 13, No. 14, 863-866. (1975)

3) O. A. Anderson, W. R. Bakers, S. A. Colgate, J. Ise Jr., and V. Pyle, "Neutron Production in Linear Deuterium Pinches", Phys. Rev., Vol. 110, No. 6, 1375-1387. (1958)

4) Y. Kondo, "A Model of Charged Particle Accelerations in the Plasma Focus", J. Phys. Soc. Jpn, Vol. 53. No. 12. 4200-4209. (1984)

5) B. A. Trubnikov and S. K. Zhadanov, "Particle acceleration by Breaking of the constrictions of a z-pinch and a plasma focus", Sov. J. Phys., Vol. 43, No. 1, 48-54. (1976)

6) T. Yamamoto, K. Shimoda, K. Kobayashi and K. Hirano,. "Correlation between Plasma Dynamics and Emission of Deuteron Beam, X-rays and Neutrons in a Plasma Focus Discharge", Jpn. J. Appl. Phys., Vol. 23, No. 2, 242-246. (1984)

7) R. Deutsch. and W. Kies, "Ion Acceleration and Runaway in Dynamical Pinches", Plasma Phys. Control. Fusion, Vol.30 No.3 263-276. (1988)

8) K. Hasegawa, H. Akiyama, S. Katsuki, S. Maeda, F. Kinoshita and H. Kuribayashi, "Development of Inductive Energy Strotage Pulsed Power Genrator with Output of MV class", NIFS-PROC-23, 101-107. (1905)

9) K. Takasugi, H. Suzuki, K. Moriyama and T. Miyamoto, "Energy Transfer to Gas-Puff Z-Pinch and X-ray Radiation", Jpn. J. Appl. Phys., Vol. 35, No. 7, 4051-4055. (1996)

10) J. J. Thomson, "The Corpuscular Theory of Matter", Archibald Constable Co., Ltd., London, (1907)

11) M. J. Rhee, "Compact Thomson Spectrometer." Rev. Sci. Instru., Vol. 55. No. 8. 1229-1234. (1986)

12) X. M. Guo. and C. M. Luo, "Experimental study of Energy Spectrum of ion beams from gas-puff z-pinch plasma", J. Phys. D Appl. Phys., Vol. 29 388-391.(1996)

13) H. Neo and D. K. Park "Measurement of Argon Ion Beam and X-ray Energies in a Plasma Discharge." Physica Scripta Vol. 65, 350-355. (2002)

14) G. Gerdin, W. Styger and F. Venneri, "Faraday Cup Analysis of Ion Beams Produced by a Dense Plasma Focus." J. Appl. Phys., Vol. 52 No. 5. 3269-3275. (1980)

15) D. R. Kania and L.A. Jones "Observation of an Electron Beam in an Annular Gas-Puff Z-Pinch Plasma Device", Phys. Rev. Lett. Vol. 53 No. 2. 166-169. (1984)

16) K. Takasugi and H. Akiyama, "Energy Transfer and X-ray Radiation Characteristics of a Gas-Puff Z-pinch", Jpn. J. Appl. Phys. Vol. 43, No. 9A. 6376-6380. (2004).

Characterization and Environmental Application of Deep Ultraviolet Flash-Lamp

Yuji Otsuka, Mitsuo Nakajima, Tohru Kawamura, and Kazuhiko Horioka*

Department of Energy Sciences, Tokyo Institute of Technology,
Nagatsuta 4259, Midori-ku, Yokohama, 226-8502, Japan

A high power ultraviolet(UV)-flash-lamp(FL) system was characterized for discharge parameters; species of working gas, its pressure, input power and energy. We measured the total emission energy, the spectral photon flux, and the emission spectra as a function of the discharge parameters. We made clear that increase of highly ionized ions in the discharge plasma is important to improve the photon output efficiency in wavelength band called DUV(Deep Ultra-Violet, 180-300nm) region. We showed that spectral peak intensity shits to short wavelength with increase of the input peak power and decrease of the pressure. The ratio of photon output in DUV region increased with use of high z species. When a discharge was driven in 15Torr Xenon with charging voltage of 13kV, spectral intensity peaked at 295nm and spectral efficiency (SE) in DUV region reached 68%.

Keywords: Flash-lamp, Pulsed discharge, Deep UV, Rare gas, Dose rate effect

I. INTRODUCTION

Recently, FLs are remarked in industries because of requirements of high power UV light source, and also environmental and health concerns for the toxicity of mercury lamp [1–6]. In the field of industrial application, a fast pulse power is applied to the electrodes in a quartz tube filled with a rare gas in time scale of 10^{-3}-10^{-9}sec and the discharge in rare gas can produce intense radiation in UV and visible region depending on the discharge parameter (DP).

Figuare 1 indicates an absorption spectrum of DNA. As shown, the absorption spectrum peaks around 260nm and this wavelength region is specially called DUV in UV region [7]. Chromophores contribute to photo-degrade the chemical compounds and it's absorption spectrum also has high spectral peak in DUV region [8]. For mitigating harmful substances and applications to biotechnology, photon sources in DUV region are thought to be effective. For practical applications, it is important to improve photon emission in DUV region.

For the UV and DUV photo treatments, not only dose effects but also dose rate effect could be the factors. In fact it is reported that dose rate is effective on induced mutation by x-ray and γ-ray irradiation [7]. However, in the past short-pulse UV radiation study, the effect of dose rate on the induced mutation isn't discussed. In this study, we note that high photon flux FL has a potential to induce chemical reaction efficiently in comparison with DC lamps. For example, projects of petroleum production with industrial scale from micro algae are expect to be a possible energy source for the next generation, in which the photo induced mutation by the FL is thought to be a simple and easy means to modify it's genes. To discuss the dose rate effect, we evaluate time evolution of spectrum distribution of UV-FL in DUV region.

*Electronic address: khorioka@es.titech.ac.jp
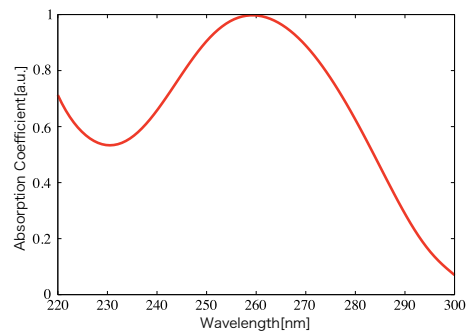
FIG. 1: Absorption spectrum of DNA [7]

Our purpose of this study is to evaluate operating characterics of UV flash lamp and to apply it to environmental and energy issues. A fast discharge FL system was constructed. In the system, the DPs, which are gas species, gas pressure, and input energy, can be varied. Light sources are characterized by three factors which are the total emission energy, the emission spectra, and the spectral photon flux. In this study, the characteristics of FL were evaluated to get an optimal condition for high photon flux and spectrum efficiency in DUV region. In addition to the basic characteristics, the application to energy and biotechnology was also discussed.

II. EXPERIMENTAL SETUP AND EVALUATION OF DISCHARGING CHARACTERISTICS

Experimental device consists of a discharge tube for plasma generation, a discharge control part, and a trigger circuit. Figure 2 shows the discharge circuit diagram of the FL. The electrostatic energy(E[J]) of the driver can be represented by $E = \frac{1}{2}CV_{in}^2$ and V_{in} is the charging voltage. When the gap switch is closed, pulsed current is driven in the discharge tube and radiation is generated from the joule heated plasma. Emission characteristics
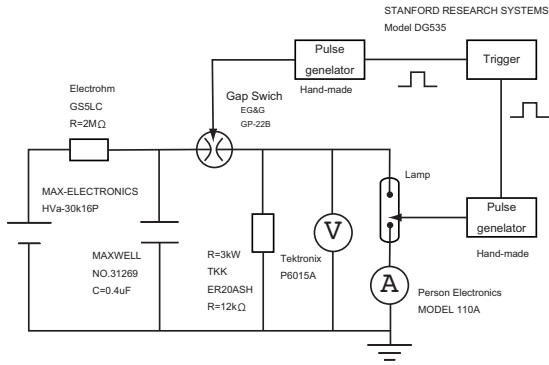
FIG. 2: Discharge circuit diagram for DUV flash-lamp

FIG. 3: Dependence of input power on Kr filling pressure

FIG. 4: Dependence of input energy on Kr filling pressure

from the plasma basically depend on plasma temperature and density, and the plasma temperature fundamentally depends on input power history to the plasma. Emission characteristics are thought to change with gas species, its pressure, and input power history. It is important to evaluate energy efficiency of the transmission from power source to the plasma. From the circuit characteristics of this experimental setup, stray inductance(L) and residual resistance(R) were estimated to be $L \sim 490nH$ and $R \leq 0.15\Omega$ respectively[9].

Figuare 3 shows the dependence of input power history on Kr pressure, where electrostatic energy was kept constant at 33.8J. It is shown that at same discharge condition, input power peak increases with pressure decrease. At Kr fill pressure of 15Torr, input power peak was estimated to be about 36MW after 0.6us from the start of discharge. At 120Torr, it was estimated to be about 29MW at discharge time of 1.1us. The FWHM(full width at half maximum) of power history are 1.0us and 1.3us respectively.

Figuare 4 shows net energy deposition to the plasma, which is calculated by integrating the input power history. It is shown that at same discharge condition, the ratio of energy input to the plasma increases with pressure. The input power waveform indicates that the matching between the discharge circuit and the plasma is improved with pressure increase. This result shows that to optimize the DP for energy density, energy conversion process between the electric circuit and the plasma should be considered.

III. EVALUATION OF LIGHT SOURCE CHARACTERISTICS

We measured the total emission energy, the spectral photon flux, and the emission spectrum as a function of the DPs. In this study, the discharge plasma was investigated as a function of gas species and gas pressure, and light source performance was comparatively evaluated. To evaluate absolute value of photons in DUV region, measurement of total emission energy is considerably im-

portant. As the light emission from the plasma extends from UV to visible region, a calorimeter(SCIENTECH, 38UV5) is used for the measurement of total emission energy.
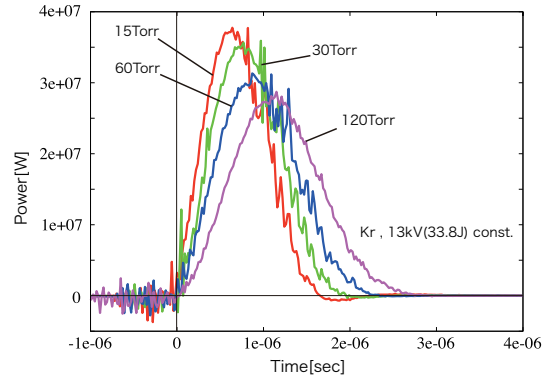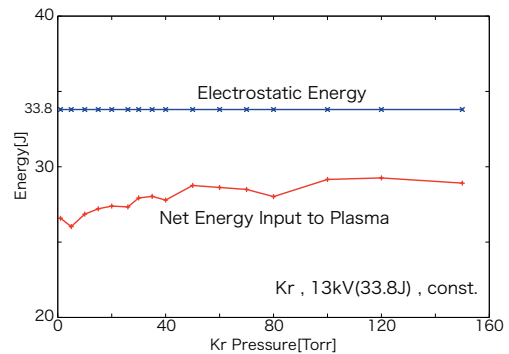
Figuare 5 shows photon output as a function of fill pressure. As shown in the figure, the total emission energy increased with pressure in both gas spieces. This result is thought that net energy input to the plasma and the number of ions increse with pressure. The emission energy from Xe was higher than that from Kr, because Xe has a lot of excitation levels.

Temporal evolutions of spectral flux and emission spectra versus the input power and gas species were evaluated by using an VUV spectrometer (Acton Research Corporation, VM-504). Table I shows specifications of the spectrometer. A photomultiplier (HAMAMATSU, R2256HA) was mounted at the exit slit and the internal space of the spectrometer was held in vacuum. Based on atomic data from NIST(National Institute of Standards and Technology), we can predict that to improve photon output in DUV region, it is important to increase emission from highly-ionized ions[10]. Development of ionization degree in the discharged Kr plasma was considered versus the gas pressure.

Figuare 6 shows temporal evolutions of spectral output from KrI, KrII, and KrIII. It is clear that emission
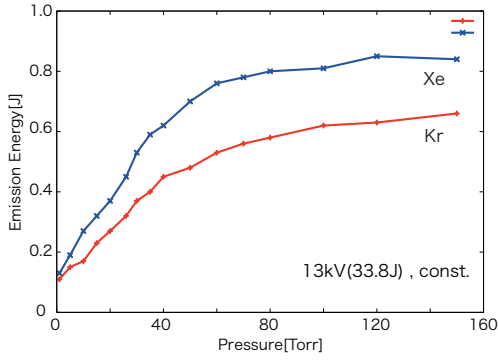
FIG. 5: Dependence of total emission energy on filling pressure

TABLE I: Specification of vacuum ultraviolet spectroscope

Grating	Resolution	Dispersion	Wavelength range
1200g/mm	6nm/mm	2.1nm/mm	115'1400nm

duration increases with pressure and the emission from doubly-ionized ions at 332.6nm increases with pressure decrease. As shown in Figuare 6(a) and (b), when fill pressure increased, the FWHM of emission increased. Because the plasma temperature doesn't rise so much, emission from lowly- ionized ions contributes strongly. As shown in Figuare 6, due to the increase of specific discharge input power; i.e., as the plasma temperature increase with pressure decrease, emission from doubly-ionized ions contributes strongly in low pressure region.

As the flash lamp plasma is expected to be optically thin, spectral fine-structure is thought to be difficult to evaluate. Therefore, we set wavelength interval of the exit slit of a spectrometer at 7.5nm, to measure the spectrum distribution. The bandwidth of the spectrometer was turned to 5nm in wavelength range of 180-600nm. It enables to measure all lines of spectrum distribution. Relative intensity was obtained with consideration of transmission of quarts, air, and window of the spectroscope; CaF_2, reflectance of spectrograph, radiation sensitivity, and the current multiplication factor of photomultiplier[11].

Figure 7 shows the time evoutions of spectrum distribution versus the gas pressure. As shown in Figure 7(a), 1.5us after the discharge, peak intensity reached at 325nm and emission from doubly-ionized ions contributed highly. The spectrum efficiency and the emission energy in DUV region were estimated to be 22% and $0.23(J) \times 0.22 = 0.05(J)$ respectively.

In Figure 7(b), we can see that 2.0us after discharge, the peak intensity reached at 375nm and emission from singly-ionezed ions contributed highly. The SE and emission energy in DUV region are estimated to be 19% and $0.62(J) \times 0.19 = 0.12(J)$ respectively. Emission energy in DUV region increased 2.4 times with pressure. This is
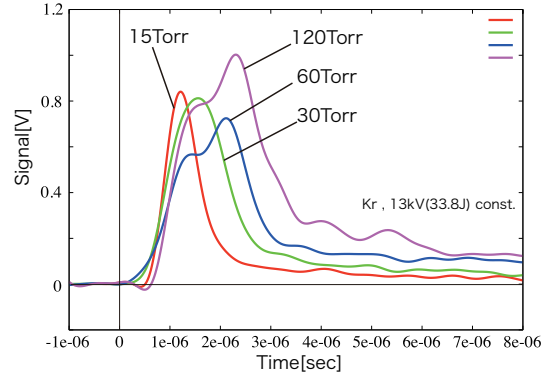
(a)Time evolution of spectral emission from KrI(587.1nm)
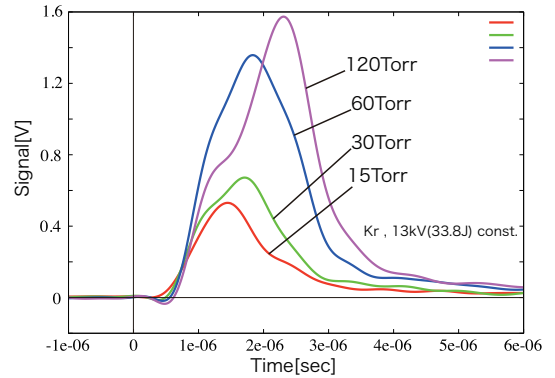
(b)Time evolution of spectral emission from KrI I(473.7nm)
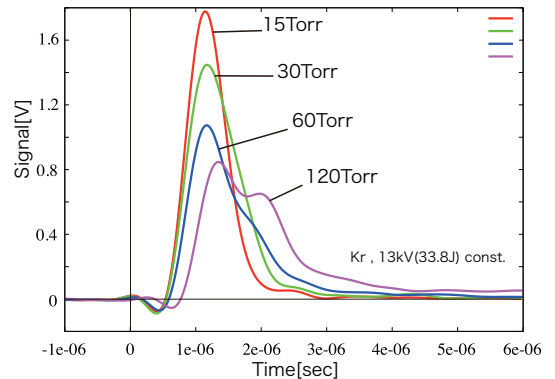
(c)Time evolution of spectral emission from KrII I(332.2nm)

FIG. 6: Time evolutions of spectral emission from neutral, singly-ionized, and doubly-ionized lines

due to increase of ions which contribute to the in-band emission. From the experimental observation, it is clear that spectral peak intensity shifts to short wavelength with pressure decrease. To obtain high photon flux and SE in DUV region, these results figured out that the FL plasma should be heated with high peak power and short pulse.

9
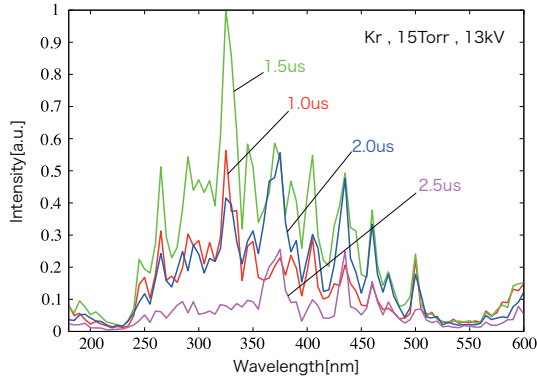
(a)15Torr Kr with charging voltage of 13kV
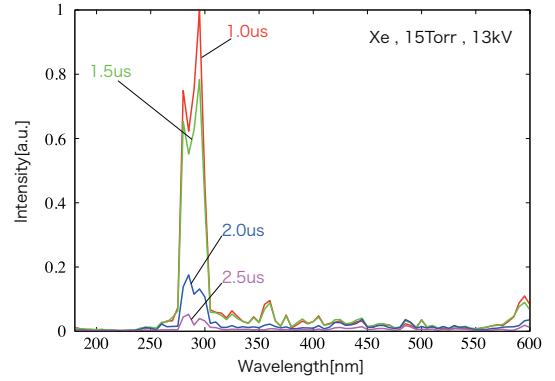
(b)120Torr Kr with charging voltage of 13kV
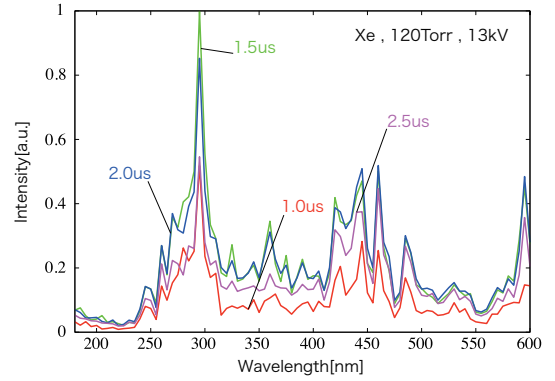
FIG. 7: Temporal evolutions of Kr emission spectrum

(a)15Torr Xe with charging voltage of 13kV

(b)120Torr Xe with charging voltage of 13kV

FIG. 8: Temporal evolutions of Xe emission spectrum

In the next experiment, we compared time evolutions of spectrum distribution for Xe. The SE in DUV region largely increased at low pressure in case of Xe and photon output similarly increased 4.4 times. It is clear that high proportion of photon output in DUV region is mainly due to high Z gas. As shown in Figuare 8(b), the intensity peaks at 295nm after 1.0us. When input power increases with pressure decrease, Xe plasma is dominant emission from doubly-ionized ions. In this study, we showed that when we drive 15Torr Xe with charging voltage of 13kV, we get high flux and SE in DUV region.

IV. APPLICATION TO ENVIRONMENTAL AND ENERGY ISSUES

Micro algae is known to store oil like substance in it's body by photosynthesis. For mitigating the global warming and oil price hike, research on the mutation for more petroleum-productive algae, which is tolerant for salt damage is proceeding recently. In this research, UV irradiation was performed to reform the DNA in botryococcus. Instead of difficult gene analysis, we just compared the survival rate against the UV irradiation. Figure 9 shows the result of UV fluence dependence on the algae
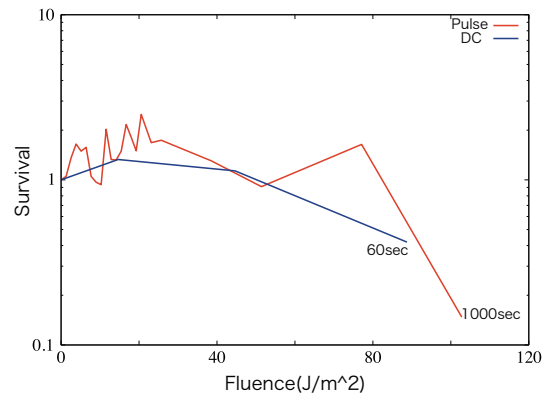
FIG. 9: UV fluence dependance of survival rate of micro algae

survival rate. Intensity is estimated to be $1.5W/m^2$ for low pressure mercury lamp. In the case of UV flash lamp, the irradiation intensity was estimated to be $0.26J/m^2$ per shot in DUV region.

V. CONCLUSIONS

The purpose of this study was to evaluate operating characteristics of low pressure, pulsed UV flash lamp and to apply it to environmental and energy issues. The light source was characterized for three factors, in which the primary experimental parameters were pressure and gas species(Kr and Xe). The results showed that to get intense photon emission in DUV region, increase of line emission from highly ionized ions is essential. At same discharge condition, it is clear that input power increases with pressure decrease and then the photon emission peak shifts to shorter wavelength region. It is also clear that the rate of emission of DUV region increases with ion mass, that is, high Z species are advantageous for the efficient emission. We showed that at 15 Torr Xe, and with input power of roughly 30MW, the SE in DUV region reached 68% and that the pulsed FL can provide highly pure and high flux light emission in DUV region.

VI. ACKNOWLEDGMENT

[1] Akihiko Tauchi, Chikako Ichimura, Kazuhiko Yoshikawa and Takeshi Sakurai, J.Illum.Engng.Inst.Jpn, Vol.92, No.2(2008)

[2] Kenneth F.McDonald, Randy D.Curry, Thomas E.Clevenger, Blaise J.Brasos, Kenneth Unklesbay, Abrahim Eisenstark, Sarah Baker, Jeffry Golden and Robert D.Morgan, IEEE TRANSACTIONS ON PLASMA SCIENCE, Vol28, No.1(2000)

[3] Kenneth F.McDonald, Randy D.Curry, Thomas E.Clevenger, Kenneth Unklesbay, Abrahim Eisenstark, Jeffry Golden and Robert D.Morgan, IEEE TRANSACTIONS ON PLASMA SCIENCE, Vol28, No.5(2000)

[4] Kenneth F.McDonald, Randy D.Curry, Patrick J.Hancock, IEEE TRANSACTIONS ON PLASMA SCIENCE, Vol30, No.5(2002)

[5] Raymond Schaefer, Michael Grapperhaus, Ian Schaefer and Karl Linden, J.Environ.Eng.Sci.6 : 303-310(2007)

[6] Keisuke Okubo : Light Edge in Japanese, optical technology journal/Feature Discharge Lamp, No.27(2004)

[7] Seiji Matsumura : Radiation Genetics in Japanese, P73'78, Syoukabo(1964)

[8] Haruo Inoue : Photochemistry in Japanese, Maruzen(1999)

[9] Yuji Otsuka : Characterization and Environmental Application of Deep Ultraviolet Flash-Lamp, Tokyo Institute of Technology Master's thesis(2009)

[10] Atomic spectra datafile, NIST(National Institute of Standards and Technology), http://physics.nist.gov/PhysRefData/ASD/index.html

[11] Glenn F Knoll : RADIATION DETECTION AND MEASUREMENT

[12] ST Pai,Qi Zhang : INTRODUCTION TO HIGH POWER PULSE TECHNOLOGY(1995)

Propagation dynamics of ultrashort laser pulse in argon gas with atmospheric-pressure

T. Higashiguchi[1,2], M. Kudo[1], T. Otsuka[1], N. Yugami[1,2],
T. Yatagai[2], and E. J. Takahashi[3]

[1]*Department of Electrical and Electronic Systems Engineering,
Utsunomiya University, Yoto 7-1-2, Utsunomiya, Tochigi 321-8585 Japan*
[2]*Center for Optical Research & Education (CORE), Utsunomiya University,
Yoto 7-1-2, Utsunomiya, Tochigi 321-8585 Japan*
[3]*Extreme Photonics Research Group, RIKEN Advanced Science Institute,
2-1 Hirosawa, Wako, Saitama 351-0198 Japan*

ABSTRACT

Self compression through filamentation, which formed by the self-focusing and plasma defocusing effect, in a free-space argon gas-filled cell has been demonstrated by use of the high energy laser pulse in a few 10-mJ energy regions. A 130-fs pulse was compressed to less than 60 fs (full width at half-maximum) with the output energy of 17 mJ at the argon gas pressure of 25 kPa, correspond to input peak power of $3.65P_{crit}$, where P_{crit} is the self-focusing critical power, through the filamentation in high energy region. Pulse splitting of the optical laser pulse was also observed due to the multiple filamentation at the focal point.

I. Introduction

Ultrashort laser pulse is provided in the strong-electric field science, such as x-ray laser,[1] high order harmonic generation,[2] and charged particle acceleration.[3] Although the development of the laser system with the energy of a few 10 mJ at the pulse width of a few 10 fs as using these experiments, that is very expensive and very complication of the optical layout. To obtain the ultrashort, intense laser pulse the pulse compression due to a self-phase modulation (SPM) and the dispersion compensation has been demonstrated.[4] The spectrum broadening produced by the SPM, through nonlinear propagation in medium has been studied. The spectrum broadening was caused by the temporal change of the refractive index of $n = n_0 + n_2I$, where n_0, n_2, and I are the linear refractive index, the nonlinear refractive index, and the laser intensity, respectively. The refractive index under the Kerr effect depends on the laser intensity. The temporal change of the optical phase produces new wavelength components to the spectrum. The effective SPM also is induced by both the optical Kerr effect and the long filamentation production when the laser intensity higher than the self-focusing critical power of $P_{crit} = \lambda^2/2\pi n_0 n_2$ in the propagation process of the ultrashort, intense laser pulse in the medium, where λ is the wavelength of the laser pulse. The laser intensity increases due to self-focusing as the pulse propagates in the medium. When its intensity is strong enough, the field ionization also occurs and a plasma produced, which acts as negative lens to defocusing the laser light. The balance between the self-focusing and plasma defocusing provides a stable formation of the filamentation, so called self-channeling, in the medium, which keeps high laser intensity around 10^{13} W/cm^2 over the Rayleigh length.

To induce the efficient SPM, a pulse compression method in a gas-filled hollow fiber has been demonstrated to produce even ultrashort femtosecond pulses.[5] A hollow optical fiber with a pressure gradient has been also used as the nonlinear medium to broaden the spectrum, resulting in the compressed pulse width of 8.4 fs with the pulse energy of 5 mJ.[6] The incident pulse energy, however, was limited to a few mJ levels due to the low damage threshold of the hollow fiber wall. When the input power higher than the critical power incidents in the gas-filled hollow fiber, the mode coupling efficiency between the laser beam and its fiber might be low due to the self-focusing, resulting in the lower transmission. To overcome low input laser energy using the hollow fiber, it is necessary to appropriate self-channeling due to the self-focusing and plasma defocusing effect that are efficiently

coupled with the high energy laser pulse. By use of two argon gas-filled cells and the chirp mirrors as the compressor, a 5.7-fs pulse with 0.38 mJ through a 10–15-cm long filamentation in the argon gas was reported.[7] This method to produce the long interaction length is extended through the formed filamentation by loose focusing. A 7.4-fs pulse with a 2-mJ energy was obtained by using the gas-cell without the hollow optical fiber-filled with noble gas and the compressor.[8] In the case of the free space filamentation, both the self compression and the pulse splitting have been also observed.[9] A previous reported experimental result, which spatiotemporal evolution of the self-compression and the pulse splitting, is limited at the input energy of less than 5 mJ. To achieve the effective self compression with a few 10-mJ high energy regions, it is important to knowledge the dynamics of the ultrashort laser pulse through the filamentation.

In this paper, we reported the self compression and the pulse splitting through the argon filamentation. We observed the 60-fs output with the 17-mJ energy, which was almost half of the 130-fs input with the input energy of 20 mJ. We also observed the splitting pulses at the low laser energy and the low argon gas pressure, which was attributed to the multiple filamentation at the focal point.

II. Experimental setup

Figure 1 shows a schematic diagram of the experimental setup. We used a femtosecond laser pulse from a chirped-pulse-amplification Ti:sapphire laser system, operating at a repetition rate of 10 Hz. The pulse width of the laser was 130 fs (full width at half-maximum: FWHM) with a maximum output energy of 40 mJ and a central wavelength of 800 nm with a bandwidth of 7 nm (FWHM). The laser pulse was focused inside a 1-m long pressurized Ar gas cell by use of a planoconvex lens with a focal length of 1.5 m. The focused laser intensity was evaluated to be higher than 1.1×10^{13} W/cm^2 at the focus, assuming no self-focusing in the present case. To measure the pulse width of the output laser, the output beam through the gas cell was injected into a single-shot, second-harmonic autocorrelator. To measure the detail characteristics of the output laser pulse, the output beam of the gas cell was diagnosed by a spectrometer and a spectral phase interferometry for direct electric-field reconstruction (SPIDER). The spectra were measured by use of a multichannel spectrometer (Ocean Optics HR-4000). The beam diameter and its profile at the focal point and an exit of the gas cell along the optical axis were measured by a charge coupled device (CCD) camera.
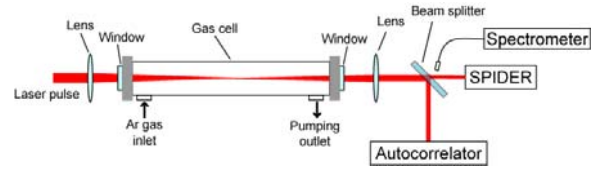
Fig. 1. Schematic diagram of the experimental apparatus.

III. Experimental result and discussion

High intensity of the laser pulse is maintained over an extended distance in the filamentation, leading to large spectral broadening through the nonlinear interaction with the gas medium. The Kerr effect depends on the laser intensity and the gas pressure in the gas-cell. Figure 2 shows the pulse splitting (a) and its self-compression (b) through the gas-cell under the different conditions. The splitting pulse in Fig. 2(a) was observed at the laser energy of 2 mJ and the Ar gas pressure of 8 kPa. The low-intensity pulse appeared faster than the main laser pulse with high intensity. The pulse widths (FWHMs) of the weak pulse ("pulse 2") and strong pulse ("pulse 1") were 130 and 100 fs, respectively. It can be seen that the pulse 1 propagates with the pulse width that is shorter than that of the initial width. The pulse 1 propagated with slower group velocity dispersion in the filamentation, which was attributed to a strong nonlinearity.[10] The remnant pulse (pulse 2) in a weak nonlinearity separates in the filamentation, leading to the pulse splitting. The pulse 2 propagated with the pulse width comparable with the initial width. The self-compressed pulse, on the other hand, was observed at the laser energy of 6 mJ and the Ar gas pressure of 70 kPa, as shown in Fig. 2(b). The pulse width of the 100 fs (FWHM) from the initial pulse width was compressed with the tail in the front of the main pulse.
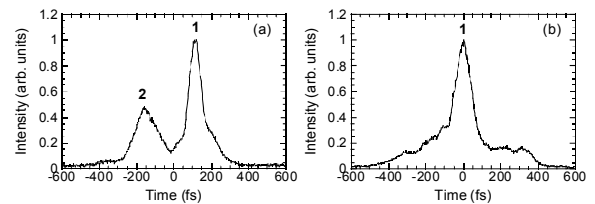
Fig. 2. Output temporal waveforms at the input laser energy of 2 mJ and the Ar gas pressure of 8 kPa (a), and its energy of 6 mJ and its pressure of 70 kPa (b), respectively.

Figure 3 shows the self-focusing critical power-normalized input power dependence of the pulse duration of the output laser pulse. Effective self-compression due to the Kerr effect was observed at $P_{in} = (3-8)P_{crit}$. The effective self-compression was observed to be $P_{in} \approx 3.65P_{crit}$, where $P_{crit} \approx 42$ GW and $P_{in} \approx 154$ GW at the input

energy of 20 mJ and the Ar gas pressure of 25 kPa. The shortest pulse duration was about 60 fs (FWHM). In the case of the low Pin less than 3Pcrit, the pulse splitting was also observed. As a result, the duration of the splitting pulse was almost same of that of the input laser pulse. Effective self-compression was not observed for $P_{in} \geq 8P_{crit}$, which was attributed to the beam diffraction and shorter filamentation length due to the plasma generation in the gas cell.
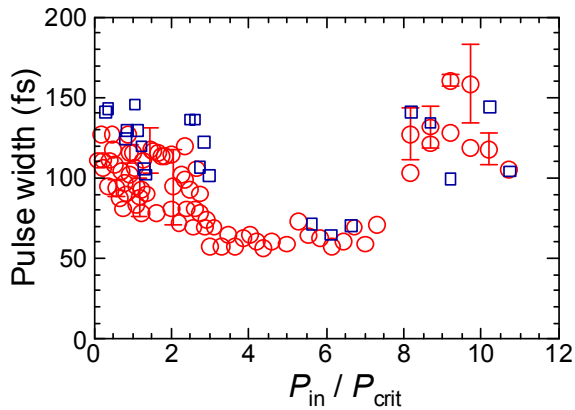
Fig. 3. Self-focusing critical power-normalized input power dependence of the pulse duration of the pulse 1 (circles) and the pulse 2 (rectangles), respectively.

The multiple filamentation of the ultrashort laser pulse was separated in the medium, resulting in the production of the multiple pulses.[11] When the pulse splitting was observed at $P_{in} \approx 0.12P_{crit}$, we measured the relative phase by use of the SPIDER. Figure 4 shows the spectrum and the relative phase at the laser energy of 2 mJ and the argon gas pressure of 8 kPa, corresponding to the temporal waveform, as shown in Fig. 2(a). The spectral bandwidth of 10 nm (FWHM) was broader than that of the input laser pulse (7 nm). In the phase spectrum, the red region covered the spectral region of the incident laser pulse, whereas the blue region extended over newly generated spectral content in the short wavelength wing of the spectrum. We believe that the phase difference was resulted in the dispersion of the plasma and the gas. The latter pulse (pulse 2) gives rise to a leading uncompressed pulse, whereas the self-compression appears to be limited to the blue region of the spectrum. The pulse splitting was observed, which was attributed to the different group velocities of the multiple filamentation.

We observed the laser beam profile at the focal point to confirm the laser beam splitting in the filamentation. Figure 5 shows the beam profile at the focal point of 165 cm from a lens inside the gas-cell

at the input powers of $P_{in} \approx 0.12P_{crit}$ (a), $P_{in} \approx 3.07P_{crit}$ (b), and $P_{in} \approx 10.23P_{crit}$ (c), respectively. We observed several hot spots as the multiple filamentation at $P_{in} \approx 0.12P_{crit}$ in Fig 5(a) and $P_{in} \approx 10.23P_{crit}$ in Fig. 5(c). On the other hand, we also observed a single filamentation at $P_{in} \approx 3.07P_{crit}$ (b). As a result, the splitting pulses were originated from the multiple filamentation through the gas-cell. The pulse duration was almost observed to be 60 fs with a single filamentation at the optimum $P_{in} = (3-8)P_{crit}$. The spectrum broadening results in the longer interaction length by the formed filamentation. The pulse splitting at $P_{in} \geq 8P_{crit}$ was also originated from multiple filamentation by propagating high intensity laser pulse.
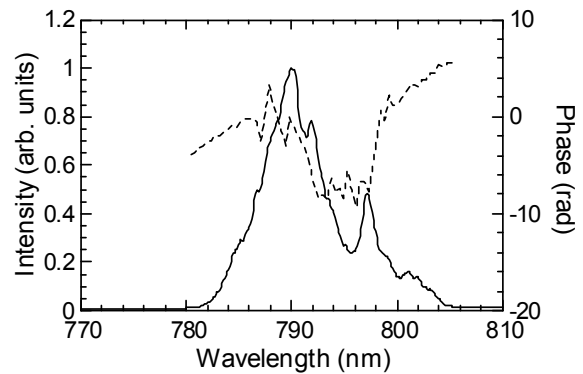
Fig. 4. Spectrum (solid line) and the relative phase (dashed line) of the splitting laser pulse at $P_{in} \approx 0.12P_{crit}$.
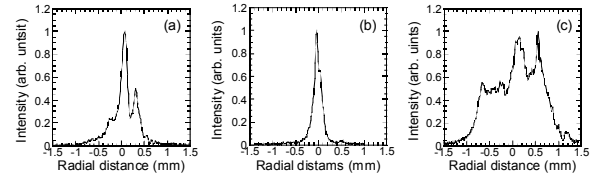
Fig. 5. The laser beam profile at the focal point in the filamentation at $P_{in} \approx 0.12P_{crit}$ (a), $P_{in} \approx 3.07P_{crit}$ (b), and $P_{in} \approx 10.23P_{crit}$ (c), respectively.

To overcome the low laser energy self-compression with a few mJ, we observe the self compression using the 130-fs laser pulse in the high energy region with the input laser energy of a few 10-mJ. The pulse duration decreased with the increase the input energy of the laser pulse. In the case of the low input energy, the duration of output pulse was almost same of that of the input pulse. At the input pulse energy of 20 mJ, the effective self-compressed pulse was observed with the duration of less than 60 fs (FWHM) with the output energy of 17 mJ at the argon gas pressure of 25 kPa, which was corresponded to $P_{in} = 3.65P_{crit}$, as shown in Fig. 6. It is expected to achieve shorter pulse width by the dispersion compensation, because the

observed pulse of 60 fs from the 130-fs input was about 1.5 times of the Fourier transform limit of 40 fs according to the spectrum of the output beam. This method without the hollow fiber could expect to be the transmission coefficient of about 100% with the input peak power of $P_{in} = (3-8)P_{crit}$ in gas-cell, but the transmittance depends on the just windows of the gas cell. On the other hand, its coefficient would be limited to be 50–70% by use of the hollow fiber. For further self compression with the input laser energy higher than 20 mJ, we may use the cascade gas-cell with long and effective interaction length with suppression of the multiple filamentation and the diffraction, which are attributed to the plasma production.
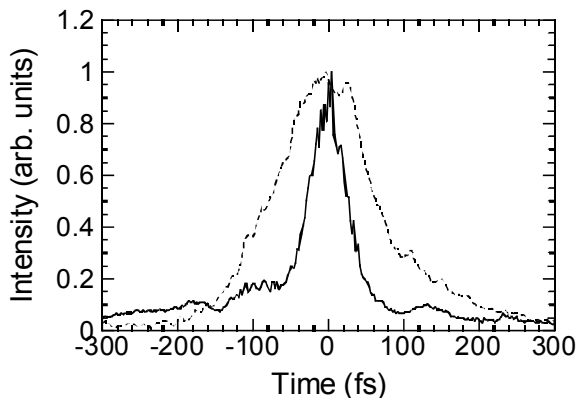
Fig. 6. The temporal waveforms of the input laser pulse (dashed line) and the self compressed output pulse (solid line) at the input laser energy of 20 mJ and the Ar gas pressure of 25 kPa, corresponding to $P_{in} = 3.65P_{crit}$.

IV. Summary

In summary, we produced the filamentation in the argon gas-filled cell without the hollow fiber by irradiating the high-intensity laser to initiate the SPM with filamentation. We observed the self compression and its splitting of the laser pulse in different P_{in}/P_{crit}. The self compression resulted in a minimum pulse width of 60 fs with the output energy of 17 mJ at the input laser energy of 20 mJ, providing one of the highest energy values ever measured. This self-compression method is very simple, and it might compress to be 30% of input pulse width by the dispersion compensation.

Acknowledgements

References
1) Y. Nagata, K. Midorikawa, S. Kubodera, M. Obara, H. Tashiro, and K. Toyoda, "Soft-x-ray amplification of the Lyman-α transition by optical-field-induced ionization," Phys. Rev. Lett. **71**, 3774 (1993).
2) E. J. Takahashi, T. Kanai, K. L. Ishikawa, Y. Nabekawa, and K. Midorikawa, "Coherent Water Window X Ray by Phase-Matched High-Order Harmonic Generation in Neutral Media," Phys. Rev. Lett. **101**, 253901 (2008).
3) W. P. Leemans, B. Nagler, A. J. Gonsalves, Cs. Toth, K. Nakamura, C. G. R Geddes, E. Esarey, C. B. Schroeder, and S. M. Hooker, "GeV electron beams from a centimetre-scale accelerator," Nature Phys. **2**, 696 (2006).
4) C. V. Shank, R. L. Fork, R. Yen, and R. H. Stolen,"Compression of femtosecond optical pulses,"Appl. Phys. Lett. **40**, 761 (1982).
5) M. Nisoli, S. De Silvestri, and O. Svelto, "Generation of high energy 10 fs pulses by a new pulse compression technique," Appl. Phys. Lett. **68**, 2793 (1996).
6) A. Suda, M. Hatayama, K. Nagasaka, and K. Midorikawa, "Generation of sub-10-fs, 5-mJ-optical pulses using a hollow fiber with a pressure gradient," Appl. Phys. Lett. **86**, 111116 (2005).
7) C. P. Hauri, W. Kornelis, F. W. Helbing, A. Couairon, A. Mysyrowicz, J. Biegert, and U. Keller, "Generation of intense, carrier-envelope phase-locked few-cycle laser pulses through filamentation," Appl. Phys. B **79**, 673 (2004).
8) S. Skupin, G. Stibenz, L. Bergé, F. Lederer, T. Sokollik, M. Schnürer, N. Zhavoronkov, and G. Steinmeyer, "Self-compression by femtosecond pulse filamentation: Experiments versus numerical simulations," Phys. Rev. E **74**, 056604 (2006).
9) M. Nurhuda, A. Suda, M. Hatayama, K. Nagasaka, and K. Midorikawa, "Propagation dynamics of femtosecond laser pulses in argon," Phys. Rev. A **66**, 023811 (2002).
10) M. Hatayama, A. Suda, M. Nurhuda, K.

Nagasaka, and K. Midorikawa, "Spatiotemporal dynamics of high-intensity femtosecond laser pulses propagating in argon," J. Opt. Soc. Am. B **20**, 603 (2003).

11) M. Mlejnek, M. Kolesik, J. V. Moloney, and E. M. Wright, "Optically Turbulent Femtosecond Light Guide in Air," Phys. Rev. Lett. **83**, 2938 (1999).

PARAMETRICAL DEPENDANCE OF COILGUN ENERGIZED BY COMMERCIAL POWER SUPPLY

Y. Uehara and S. Furuya

Gunma University, 4-2 Aramaki, Maebashi, 371-8510, Japan

ABSTRACT

The coilgun accelerates a projectile by the magnetic force produced from the current-carrying coil. We have examined the fundamental characteristic of coilgun directly energized by commercial power supply. We have successfully launched the projectile from a single coilgun and have investigated the energy conversion efficiency estimated by the velocity of projectile when the projectile, coil design and the half-wave number of applied voltage are changed. Then we have examined the behavior of a projectile using a photo diode and a laser. To increase the velocity of the projectile we have also attempted to examine a multistage coilgun.

I. Introduction

The coilgun accelerates a projectile by the magnetic force produced from a current-carrying coil and the various applications of it are possible. Fig. 1 illustrates the principle of coilgun. As a current flows through a coil, magnetic field is generated. If there is a magnetic material near the coil, it is magnetized and attracted to the coil. The projectile is accelerated to the center of coil. If the current is interrupted before the projectile arrives at the center of coil, the projectile is launched from the opposite end of coil.

The advantages of coilgun are as follows: The projectile is launched contactless, so the lifetime of the apparatus is long. No sound is produced when the projectile is launched. On the other hand, low energy conversion efficiency is the disadvantage of coilgun. Therefore, the coilgun is useful for moving a heavy load slowly, although large scale experiments to pursue high velocity have been carried out.

The previous researches on coilgun are as follows: Reference [1] deals with the design of coilgun with velocity up to 8km/s. At Sandia National Laboratories, projectiles ranging from 10g to 5kg were accelerated up to 1km/s, and Reference [2] discusses issues concerned with coilgun design and control. A simplified field-based physical model of coilgun is developed [3]. Reference [4] investigates the effects of interference between the traveling and rotating magnetic fields on the in-bore armature stability of an induction type coilgun with bore armature. Reference [5] studies the gyroscopic stabilization of projectile in double-feed induction coilguns. Reference [6] describes the characteristics and performance of coilgun for launching metal plates as an alternative to explosive launch. Reference [7] describes two grenade coilguns for

armored vehicles. Reference [8] presents a cylindrical current sheet model for the analysis and design of induction type coilguns. Reference [9] discusses the improvement of power factor related to high performance coilguns. Reference [10] describes the design and power conditioning for coilgun called the Linear Induction Launcher. As for coilgun history from thirties to seventies, refer to Ref. [11].

In general the coilgun is energized by capacitors or flywheels. With a view to applying for a low-velocity impact testing machine, we have examined the fundamental characteristics of coilgun directly energized by commercial power supply.
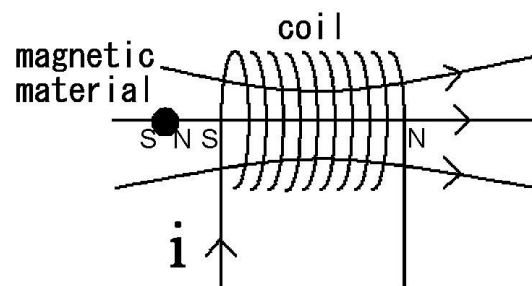
Fig.1 Principle of coilgun

II. Experimental Setup

Fig. 2 shows the electrical circuit of coilgun. The circuit is driven by a triac (SanRex, TG35C60, 600V, 35A). Fig. 3 shows the photograph of experimental setup. As shown in the figure, the apparatus is very simple. Four coils are prepared in this experiment. Fig. 4 shows the photograph of coils.

The details of four coils are shown in Table 1. In Coil4, Coil5 and Coil6, the length of acrylic pipe is 200mm and the diameter of wire is 0.3mm. In Coil7, the length of acrylic pipe is 300mm and the diameter of wire is 0.5mm. Fig 5 shows the voltage waveform across the coil. Peak current is estimated to be approximately 55A by dividing the peak voltage by the measured resistance. The behavior of projectile is examined using a photo diode and a laser. Fig. 6 shows the experimental configuration. The laser beam is irradiated perpendicular to the launch direction. The projectile can be detected by reduction of photo diode signal due to blocking of laser beam.
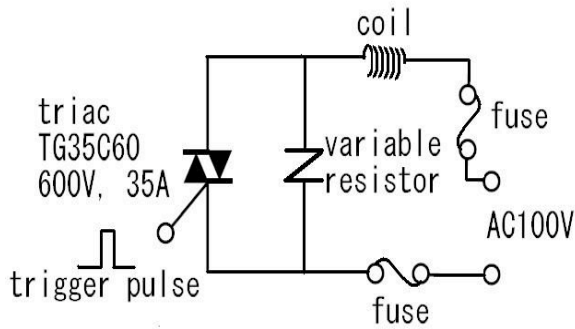
Fig.2 Electrical circuit of coilgun

Fig.4 Photograph of coils
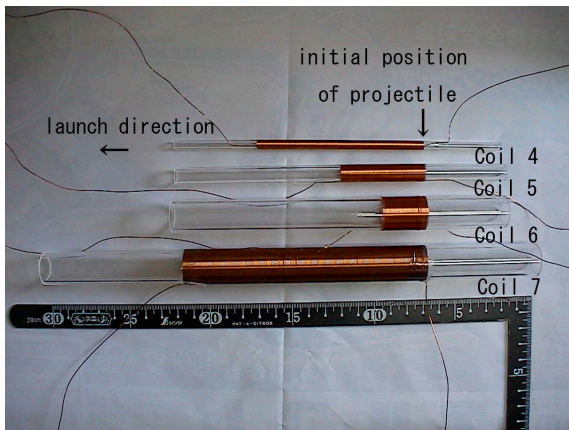
Table 1 Parameters of four coils

	outer and inner diameter of acrylic pipe (mm)	coil length (mm)	measured resistance (Ω)	measured inductance (μH)
Coil4	5×3	100	1.4	3
Coil5	10×7	50	1.3	21
Coil6	20×16	25	1.4	46
Coil7	20×16	141	1.8	162
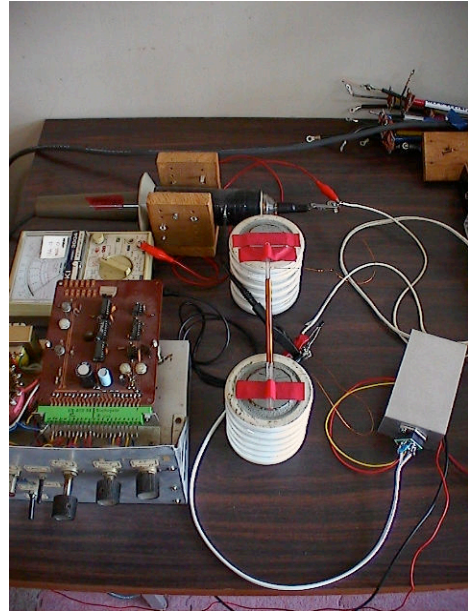
Fig.3 Photograph of experimental setup
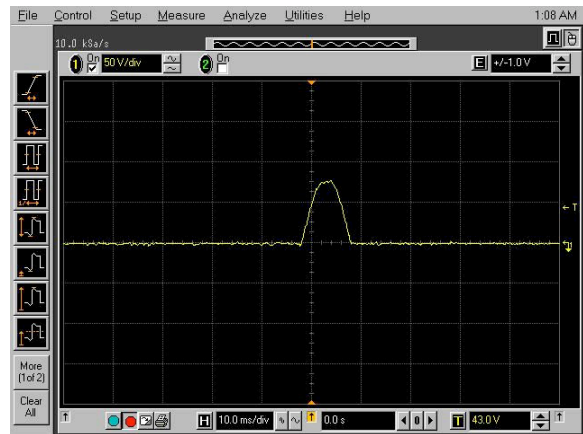
(a) Positive half-wave
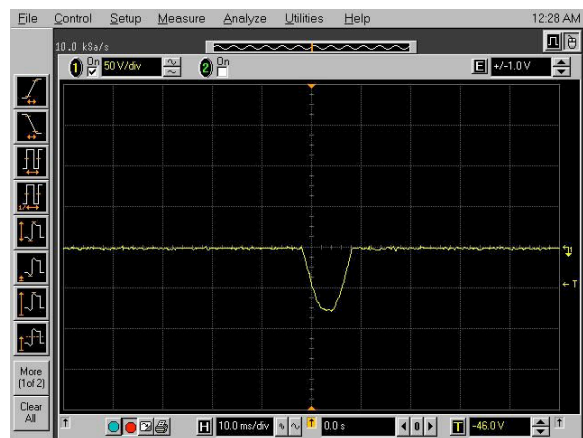
(b) Negative half-wave

Fig.5 Voltage waveform across the coil
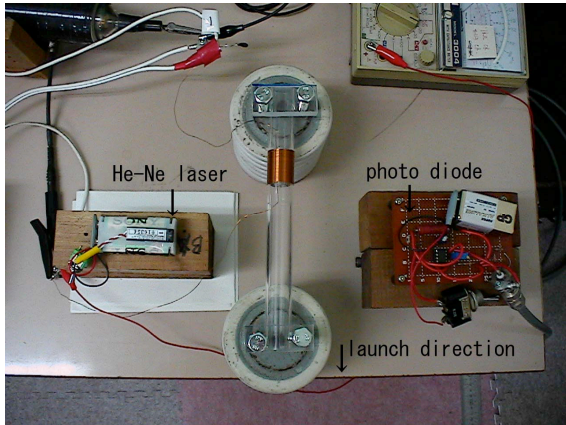
Fig.6 Photograph of experimental configuration detecting projectile using photo diode and laser

Fig.7 Flying distance of first experiment

Fig.8 Velocity of first experiment

III. Experimental Results of Single Coilgun

Six sets of experiments were carried out. First, the same projectile was launched using three coils. Then the velocity of projectile was measured. Second, three projectiles were launched using the same coil. The lengths of three projectiles are same but the diameters of them are different. Third, three projectiles were launched using the same coil. The lengths of three projectiles are different but the diameters of them are same. Fourth, the same projectile was launched using the same coil as the half-wave number of applied voltage is changed. Fifth, the time at which the projectile reached certain points from the onset of voltage application is measured using a photo diode and a He-Ne laser. Then the behaviors of the projectile are examined. Sixth, the time at which the projectile started to move from the onset of voltage application is measured using the same method of fifth experiment.

A. Launching same projectile using three coils

First, M3 stud bolt, whose length is 8mm and mass is 0.27g, was launched using Coil4, Coil5 and Coil6. The half-wave number of applied voltage was one. Fig. 7 shows the results of measured flying distance. The coil was set 690mm high above the floor. The each data is the average of five shots. 'S' in the figure means that the direction of magnetic field is the same as that of launching and 'O' vice versa. Assuming the horizontal incidence, the velocity of projectile at the exit of acrylic pipe is calculated from the flying distance and height. Fig. 8 shows the calculation results. The velocity is approximately 3m/s. The energy conversion efficiencies of Coi4S, Coil4O, Coil5S, Coil5O, Coil6S and Coil6O are 0.006%, 0.005%, 0.009%, 0.009%, 0.005% and 0.004%, respectively. The influence on the direction cannot be seen.
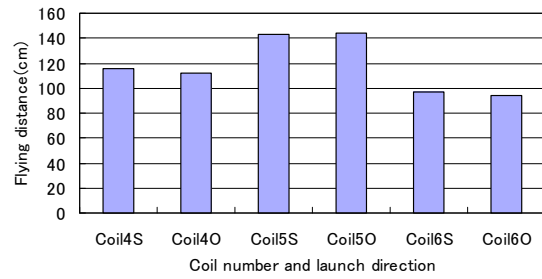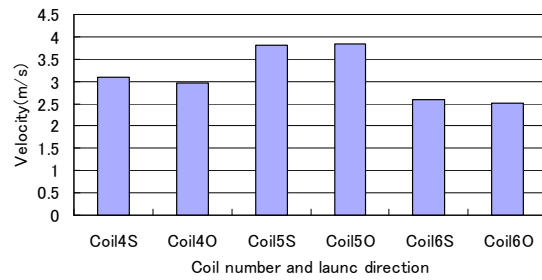
B. Changing diameter of projectile

Second, three projectiles were launched using Coil6. Three projectiles are M3, M6 and M12 steel stud bolts and their length are same, 30mm. The mass are 1.25g, 4.93g and 19.8g, respectively. The half-wave number of applied voltage was one. Fig. 9 shows the flying distances. The each data is the average of ten shots. They are almost same regardless of projectile. Fig. 10 shows the velocity of projectile. The velocity is approximately 3m/s. The energy conversion efficiencies of three projectiles are 0.03%, 0.12%, 0.39%, respectively. The energy conversion efficiency of M12 is best as the velocities of three projectiles are almost same.
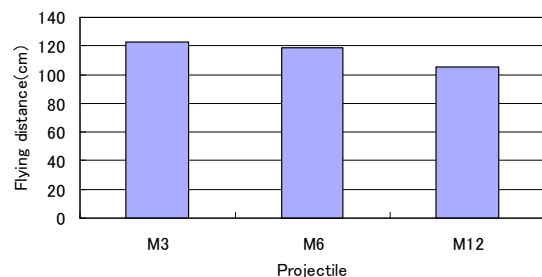
Fig.9 Flying distance of second experiment
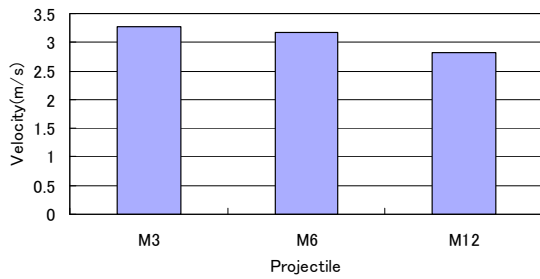
Fig.10 Velocity of second experiment

C. Changing length of projectile

Third, Three projectiles were launching using Coil5. Three projectiles are M3 stud bolts, whose lengths are 7.5mm, 15mm and 30mm, respectively. The mass are 0.304g, 0.639g and 1.26g, respectively. The half-wave number of applied voltage was one. Fig. 11 shows the results of measured flying distance. The each data is the average of ten shots. The coil was set 599mm high above the floor. Fig. 12 shows the velocity of the projectile. The velocity of projectiles is not under the influence of the length of projectiles. The energy conversion efficiencies of three projectiles are 0.02%, 0.05% and 0.08%, respectively.
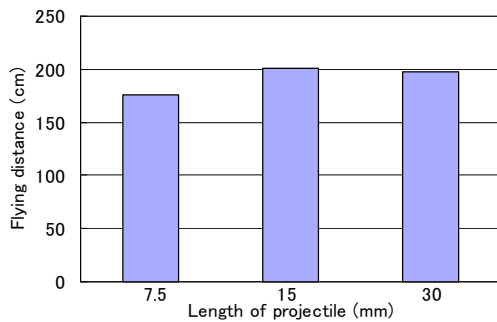
Fig.11 Flying distance of third experiment
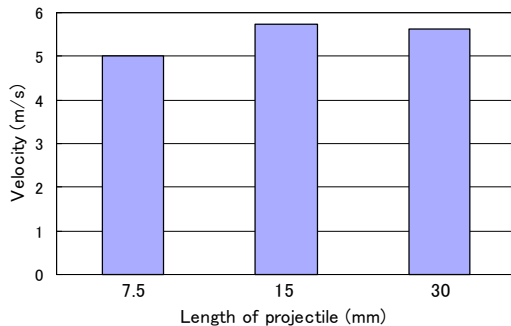
Fig.12 Velocity of third experiment

D. Half-wave number of applied voltage

Fourth, M6 stud bolt whose length is 30mm

was launched using Coil7 as the half-wave number of applied voltage was changed. The mass is 4.93g. Fig.13 shows the example of applied voltage. This figure shows the half-wave number of applied voltage is three. Fig. 14 shows the results of measured flying distance. The each data is the average of five shots. The coil was set 600mm high above the floor. Fig.15 shows the velocity of the projectile. As a consequence, the velocity of projectile is a little increased by increasing the half-wave number of applied voltage to the coil. Fig.16 shows the energy conversion efficiency. The energy conversion efficiency decreases as the half-wave number of applied voltage increases.
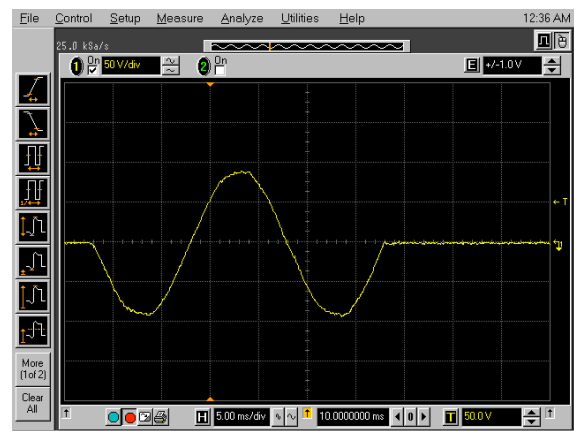
Fig.13 Example of applied voltage waveform
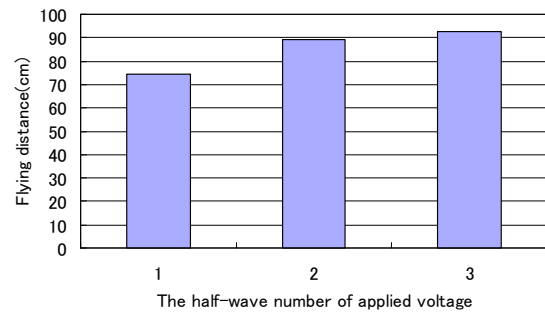
Fig.14 Flying distance of fourth experiment
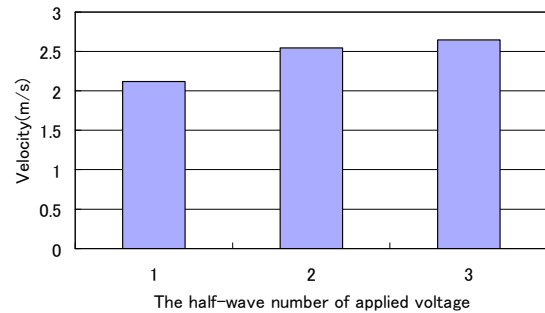
Fig.15 Velocity of fourth experiment

Fig.16 Energy conversion efficiency

Fig.18 Behavior of projectile and applied voltage waveform

E. Behavior of projectile

Fifth, M12 stud bolt whose length is 30mm was launched using Coil6. The mass is 19.8g. The behavior of projectile is examined using a photo diode and a laser. As the projectile interrupted the laser beam, the photo diode signal decreased. The laser beam was irradiated perpendicular to the launch direction. The irradiated positions are 30mm, 60mm and 90mm from the coil's edge of launch side. The half-wave number of applied voltage is one. Fig.17 shows the example of voltage waveform across the coil and the photo diode signal. This figure shows the waveform in the case of 90mm. In this figure, the upper line shows the photo diode signal and the lower line shows the voltage waveform across the coil. Fig. 18 shows the behavior of the projectile and the voltage waveform across the coil. The projectile moves as a uniform motion in the acrylic pipe. In addition, the velocity of projectile can be found by this experimental result. The velocity is the ratio of the length of projectile to the duration at which the laser beam is interrupted. The velocity of projectile is approximately 3m/s. This value of the velocity is the same that of horizontal projection method. Therefore, it is confirmed that horizontal projection method is valid.

F. Time at which projectile starts to move

Sixth, M12 stud bolt whose length is 30mm was launched using Coil6. The mass is 19.8g. To examine the time at which the projectile starts to move, the laser beam is irradiated to the edge of projectile set at initial position. As the projectile moves, the laser beam is irradiated to the photo diode and the photo diode signal appears. Fig.19 shows the voltage waveform across the coil and photo diode signal. In this figure, upper line shows the photo diode signal and the lower line shows the voltage waveform across the coil. It is interesting to note that the projectile started to move at the peak voltage each time.
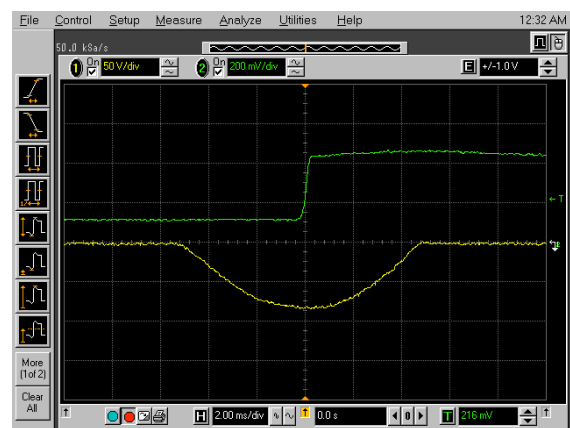
Fig.19 Voltage waveform and photo diode signal of sixth experiment

IV. Multistage Coilgun

To increase the velocity of the projectile we have made the two-stage coilgun shown in Fig.20. From the results of the fifth and sixth experiments in the previous chapter, we got the timing at which the voltage is applied to the second coil. M12 stud bolt

Fig.17 Example of voltage waveform and photo diode signal of fifth experiment

21

was launched using the coilgun. The length and mass of the bolt are 30mm and 19.8g, respectively. Fig.21 shows the voltage waveform and photo diode signal in the single-stage and two-stage operations. From the figures, the velocities in the single-stage and two-stage operations are 3.69m/s and 4.97m/s, respectively. Each data is the average of five shots. Therefore, the velocity increases by a factor of 1.35.
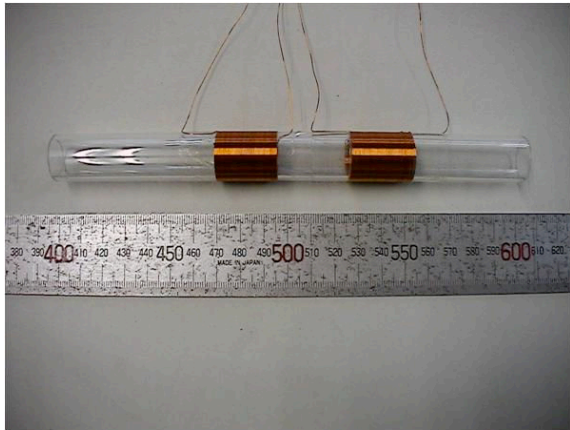
Fig.20 Photograph of two-stage coilgun

(a) Single-stage operation

(b) Two-stage operation

Fig.21 Voltage waveform and photo diode signal

V. Summary

We have successfully launched the projectile from the coilgun directly energized by commercial power supply and have completed the study of the fundamental characteristic of a single-stage coilgun. To increase the velocity of the projectile we have also attempted to examine a multistage coilgun. Accurate simulation should be done in the future to understand the experimental results.

References

1) A. Balikci, Z. Zabar, L. Birenbaum, and D.Czarkowski, "On the Design of Coilguns for Super-Velocity Launchers," IEEE Trans. Magn., vol. 43, pp. 107-110, January 2007

2) R. J. Kaye, "Operational Requirements and Issues for Coilgun Electromagnetic Launchers," IEEE Trans. Magn., vol. 41, pp. 194-199, January 2005

3) G. W. Slade, "A Simple Unified Physical Model for a Reluctance Accelerator," IEEE Trans. Magn., vol. 41, pp. 4270-4276, November 2005

4) G. Becherini, and B. Tellini, "Helicoidal Electromagnetic Field for Coilgun Armature Stabilization," IEEE Trans. Magn., vol. 39, pp. 108-111, January 2003

5) G. Becherini, "Gyroscopic Stabilization of Launch Package in Induction Type Coilgun," IEEE Trans. Magn., vol. 37, pp. 116-122, January 2001

6) P. R. Berning, C. R. Hummer, and C. E. Hollandsworth, "A Coilgun-Based Plate Launch System," IEEE Trans. Magn., vol. 35, pp. 136-141, January 1999

7) M. Liao, Z. Zabar, D. Czarkowski, E. Levi, and L. Birenbaum, "On the Design of a Coilgun as a Rapid-Fire Grenade Launcher," IEEE Trans. Magn., vol. 35, pp. 148-153, January 1999

8) J. L. He, E. Levi, Z. Zabar, L. Birenbaum, and Y. Naot, "Analysis of Induction-Type Coilgun Performance Based on Cylindrical Current Sheet Model," IEEE Trans. Magn., vol. 27, pp. 579-584, January 1991

9) P. P. Mongeau, "Inductively Commutated Coilguns," IEEE Trans. Magn., vol. 27, pp. 568-572, January 1991

10) Z. Zabar, Y. Naot, L. Birenbaum, E. Levi, and P. N. Joshi, "Design and Power Conditioning for the Coil-Gun," IEEE Trans. Magn., vol. 25, pp. 627-631, January 1989

11) H. Kolm and P. Mongeau, "Basic Principles of Coaxial Launch Technology, " IEEE Trans. Magn., vol. 20, pp. 227-230, March 1984

TREATMENT OF POLLUTED SOIL BY IRRADIATION OF PULSED, INTENSE RELATIVISTIC ELECTRON BEAM

Go Imada[1,2,*] and Hisayuki Suematsu[2]

[1]*Department of Information and Electronics Engineering, Niigata Institute of Technology,
1719 Fujihashi, Kashiwazaki, Niigata 945-1195, Japan*
[2]*Extreme Energy-Density Research Institute, Nagaoka University of Technology,
1603-1 Kamitomioka, Nagaoka, Niigata 940-2188, Japan*

ABSTRACT

Volatile organic compound (VOC) contained in soil has been treated by irradiation of pulsed, intense relativistic electron beam (PIREB). A polluted-soil treatment chamber is filled up with molded soil sample containing formaldehyde solution as a VOC, and is irradiated by a PIREB (2 MeV, 0.4 kA, 70 ns). The soil sample is mixture of a red and a black clay as supposing Kanto loam in Japan. We have obtained that 64 % of the diffused formaldehyde within the chamber is removed by firing 5 shots of the PIREB irradiation in the initial concentration of 55 ppm. The net energy efficiency of formaldehyde removal has been found to be 6.4 g/kWh at the first shot of the PIREB irradiation in the initial concentration of 300 ppm.

I. Introduction

Treatment of polluted matter by irradiation of electron beam has been attracting attention. Pulsed, intense relativistic electron beam (PIREB), in particular, is a promising candidate for the electron beam source due to its high current density, high chemical reactivity, and long range, where the range is a mean distance when the electrons will be stopped after interaction with atoms or molecules of the polluted matter. We have successfully treated a nitrogen oxide (NO_x) and a sulfur oxide (SO_x) in diesel flue gas by irradiation of a PIREB (2 MeV, 2.6 kA, 100 ns).[1,2] In these studies, a 1.6-m-long chamber was used as flue gas treatment chamber. In an atmosphere, on the other hand, the range of PIREB (electron) at 2 MeV is calculated to be 9 m[3] which is five times as long as the length of the chamber. Furthermore, the PIREB is able to penetrate liquid and solid matter. It suggests that the PIREB has great ability to treat the pollution in large or dense matter.

Volatile organic compounds (VOC), such as formaldehyde, toluene, benzene, xylene, ethyl acetate, dichloromethane, *etc*., are the organic solvents used in paint, paste, dry-cleaning solution, *etc*. Since the VOC is harmful to health and causes photochemical smog, its emission to atmosphere and discharge into soil are strictly regulated by the low. At present,

however, much industrial waste containing the VOC is dumped under the ground. Since the VOC contained in the waste is easy to volatilize into the soil, the treatment of the soil is environmental issue to solve immediately.

In this study, removal of VOC from the soil has been shown to extract PIREB's ability in the treatment of polluted matter. The soil sample containing formaldehyde solution as a VOC is irradiated with the PIREB (maximum kinetic energy of 2 MeV, peak beam current of 0.4 kA, and pulse width of 70 ns [full width at half maximum (FWHM)], and then the concentration of VOC diffused in a treatment chamber is investigated. In the above-mentioned experiments, a pulsed-power generator, "ETIGO-III"[4,5], installed in the Extreme Energy-Density Research Institute, Nagaoka University of Technology, is used for generating the PIREB.

II. Principle and advantage of VOC treatment by PIREB irradiation

Figure 1 shows the scheme of treatment of formaldehyde (CH_2O) within a soil by irradiation of the PIREB. Water (H_2O) and oxygen (O_2) species within the soil are ionized and dissociated by the collision with electron (e) of the PIREB, and then the free radicals (e.g. OH, H, and O) will be generated immediately.[6] The CH_2O is resolved by the reactions with the free radicals into H_2O, H_2, and OH. In these reactions, unfortunately, formyl radical (HCO) is

_____

*e-mail: imada@iee.niit.ac.jp
phone/facsimile: +81-257-22-8142
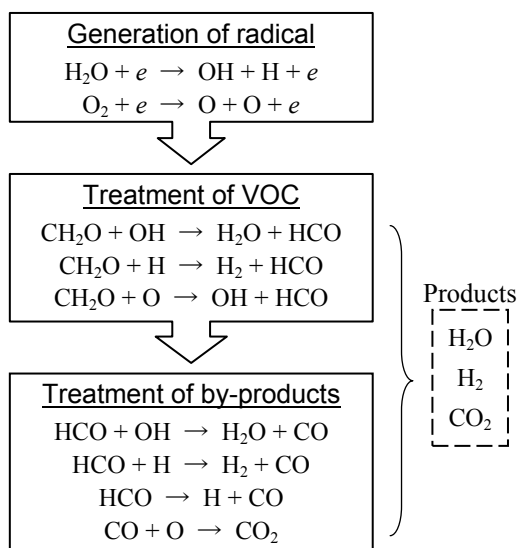
Fig. 1. Scheme of treatment of formaldehyde within soil by irradiation of electron beam.

Fig. 2. Schematic diagram of pulsed, intense relativistic electron beam (PIREB) generator, "ETIGO–Ⅲ" installed in Extreme Energy-Density Research Institute, Nagaoka University of Technology.

produced as by-products. The HCO decomposes to H and CO by itself, and also reacts with the free radicals. As a result of the reactions mentioned above, the CH_2O is treated, and the water (H_2O), hydrogen (H_2), and carbon dioxide (CO_2) are discharged as products.

In the generation of free radicals at this scheme, fortunately, the materials of radicals are H_2O and O_2 which are abundantly present in the soil and atmosphere. Therefore, some additives such as chemicals and microbes are unnecessary in this scheme. It is a big advantage of this treatment scheme. Since the current density of PIREB is sufficiently high in comparison with that of conventional direct-current electron beam or various discharges, in addition, the PIREB is able to generate a lot of free radicals simultaneously within a few nano- or micro-seconds. It suggests that the active reactions are effectively defined in time, and the undesirable excessive reactions will be controlled. Hence, the reduction of generation of by-products is prospective. Moreover, the pulsed irradiation of electron reduces the wasteful energy injection into the polluted matter. It tends to contribute the energy conservation and compact system of the pulsed power generator.

III. Experimental Setup
A. PIREB generator

Figure 2 shows the schematic diagram of PIREB generator, "ETIGO-III". It consists of a Marx generator, a pulse forming line, transmission lines, and induction acceleration cells of four stages. The Marx generator (450 nF, 34 stages) is charged up to 20 kV with the initial stored energy of 3.1 kJ (=

8.6×10^{-4} kWh), and then generates the output voltage of 680 kV. The pulse forming line converts the stored energy of the Marx generator to an output pulse having the voltage of 670 kV, current of 60 kA, and pulse duration of 100 ns. Since the output pulse of the pulse forming line is fed to the four acceleration cells through the oil-insulated coaxial transmission lines in parallel, the feed current to each cell becomes 15 kA. In each cell, three amorphous-metallic magnetic cores are installed as a 1:1 one-turn transformer producing approximately 2 MV (670 kV × 3) and 5 kA (15 kA / 3) per cell. The PIREB with the kinetic energy up to 2 MeV is generated with a field-emission foilless electron-beam diode with a hollow cathode and a ring anode set at the first acceleration cell. An axial magnetic field of 0.23 T is applied in the anode-cathode gap having the gap distance of 73 mm. The inner and outer diameters of the hollow cathode are 59.5 mm and 60 mm, respectively. Here, the diode gap is vacuumed to 0.02 Pa with an oil-diffusion and an oil-rotary pump. The inner diameter of the anode ring is 160 mm. The PIREB is guided by an external magnetic field of 0.5 T through the other acceleration cells, so that it is inductively postaccelerated with the three accelerating gaps giving the final kinetic energy up to 8 MeV. The minimum time interval of the PIREB generation is estimated to be 5 minutes which depends on a charging period of capacitor bank for the axial magnetic field.

To avoid activation of the soil sample, the first acceleration cell is only used as a PIREB source in this study. For this experiment, therefore, the maximum kinetic energy of PIREB irradiation is limited to 2 MeV.
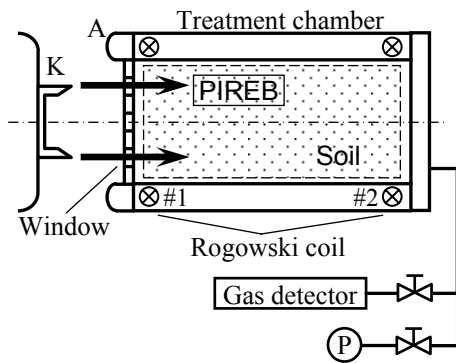
Fig. 3. Cross-sectional view of polluted-soil treatment apparatus by irradiation of PIREB. Peripheral equipment is also presented.

TABLE I
TYPICAL CONDITIONS AND ESTIMATED COMPOSITION OF SOIL SAMPLE

Conditions	
Weight ratio between red and black clay	1 : 1
Diameter	105 mm
Length	230 mm
Volume	2 L
Grain density (Specific gravity)	1 g/cm^3
Moisture	40 wt.%

Composition (molar ratio)

O: 0.48,   H: 0.31,   Si: 0.10,   Al: 0.04,
Fe: 0.02,   Ca: 0.02,   Mg: 0.02,   Na: 0.01,
K: 0.004,   Ti: 0.002,   N: 0.0002

B. Polluted-soil treatment apparatus

Figure 3 shows the cross-sectional view of polluted-soil treatment apparatus by the irradiation of the PIREB. It consists of the electron-beam diode, window, polluted-soil treatment chamber, Rogowski coils, gas detector, and oil-rotary vacuum pump. The treatment chamber is made of a stainless-steel pipe with the inner diameter of 160 mm, the length of 250 mm, and the capacity of 5 L, where the end of the pipe is terminated with a grounded stainless-steel blank flange. The chamber is separated from a vacuum part of the diode by the window attached to the anode, and is filled with the molded soil sample. To reduce the loss of PIREB current irradiated onto the soil sample, the anode is directly mounted on the other end of the chamber. A pulsed voltage of –2 MV produced with ETIGO-III is applied to the cathode-anode gap. Although the chamber can be evacuated to 10 Pa, an experiment is carried out in the atmosphere to simulate the practical treatment of polluted soil in the field. No axial magnetic field is applied to the chamber. The window consists of a titanium foil at the thickness of 40 μm with a stainless-steel punching plate at the optical transparency of 55 %. Since the pulse duration of the PIREB used in this study is observed to be of the order of 100 ns, the window is not cooled with water or coolant. At the PIREB energy of 2 MeV, the minimum kinetic-energy loss of the electron through the titanium foil is calculated to be 26 keV[3], which is negligible in comparison with the PIREB kinetic energy of 2 MeV. The electron-beam diode voltage and current are measured with a copper-sulfate-solution voltage divider and a Rogowski coil, respectively. The PIREB current emitted form the diode is observed with a Faraday cup with a pick-up coil placed on the back of the anode. The irradiated and the transmitted PIREB current for the soil sample are measured with the

Rogowski coils placed at the inlet (#1) and the end (#2) of the treatment chamber, respectively. The concentration of VOC gas volatilized from the soil sample is measured by a gas detector tube (GASTEC Co., #91L and #91M for formaldehyde) and a formaldehyde detector (NEW COSMOS ELECTRIC Co., Ltd., XP-308B) after the irradiation of the PIREB.

C. Soil sample

The soil sample is mixture of a red and a black clay as supposing Kanto loam in Japan. Some water is added to the mixture of clay to modify the moisture of the soil sample, and then a 36-%-formaldehyde reagent solution is adulterated with them. The mixture of clay is molded in a cylindrical shape, where the void ratio is estimated to be 40 %. The gross weight of the soil sample is 2 kg including 0.8 kg of water. The conditions of the soil sample are summarized in Table I, where the estimated composition of the soil sample calculated from the average composition of basalt in Japan is also shown.

IV. Results and Discussion
A. Generation of PIREB

Figure 4 shows the typical time evolution of acceleration voltage (*V*) and feed current (*I*) of the electron-beam diode, and PIREB current emitted from the diode (I_b). Here, the window is not attached to the anode to understand the properties of the diode. It is found from Fig. 4(a) that the acceleration voltage reaches –2 MV within 100 ns after rising in the voltage. The currents, *I* and I_b, also reach their peak values within 100 ns. Since the peak current of *I* and
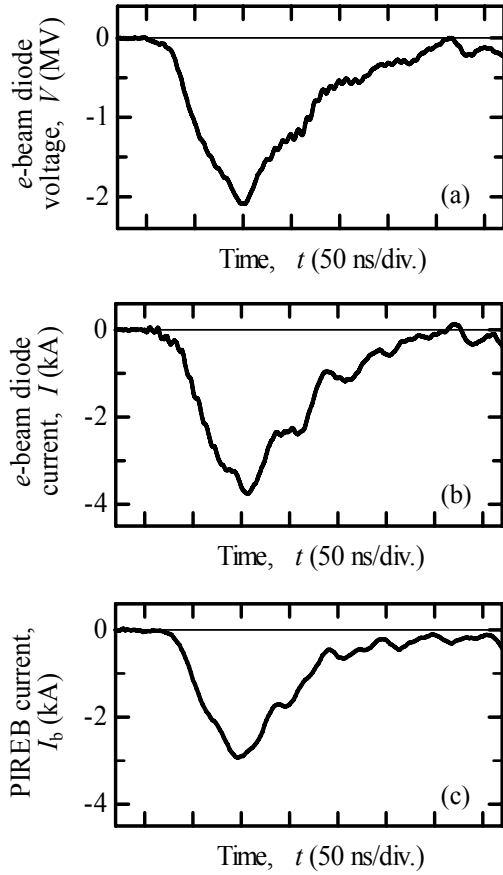
Fig. 4. Time evolution of voltage and current: (a) acceleration voltage (V) and (b) current (I) of electron-beam diode, and (c) PIREB current emitted from diode (I_b).

Fig. 5. Time evolution of PIREB current at inlet I_i (a) and end I_e (b) of treatment chamber.
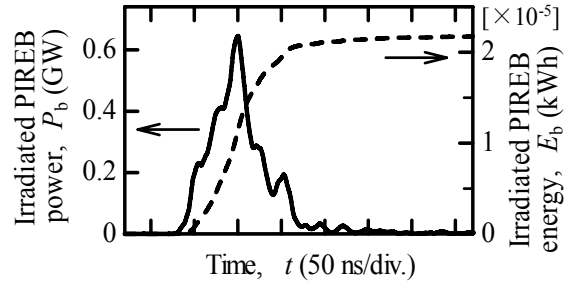
Fig. 6. Time evolution of PIREB power and energy irradiated onto soil sample.

I_b are estimated to be −3.7 kA and −3.0 kA, respectively, the conversion efficiency from the feed current to the electron-beam current is calculated to be 81 %, which is high enough to be used for the practical application of pollution treatment. The reproducibility of the PIREB generation is pretty good. We have found that the I_b remains at −3.0 kA plus or minus 0.3 kA. The pulse duration of I and I_b are estimated to be 113 ns and 100 ns (FWHM), respectively.

B. PIREB irradiation onto soil sample

Figure 5 shows the typical time evolution of the PIREB current in the treatment chamber where the molded soil sample is installed in the chamber. We have found from Fig. 5(a) that the irradiated current of PIREB onto the soil sample is estimated to be −0.4 kA. Since the window is inserted between the electron-beam diode and the treatment chamber, the PIREB irradiated onto the soil sample decreases in current. It is also found from Figs. 5(a) and 5(b) that the peak current of the PIREB decreases from I_i = −0.4 kA to I_e = −0.1 kA due to the energy deposition

into the soil sample or the dispersion and the divergence of the electron beam. The PIREB might be quenched within the soil sample before it arrives at the end of the chamber, because the I_e seems to be noise signal. The pulse width of I_i and I_e are estimated to be 70 ns and 60 ns (FWHM), respectively, which are somewhat short compared with that of I_b, because the electrons having low kinetic energy drops off in the window and the soil sample.

Figure 6 shows the typical time evolution of the PIREB power (P_b) and the energy (E_b) irradiated onto the soil sample. Here, the P_b is calculated as the product of V and I_i, and the E_b is estimated from the time integral of P_b, where the P_b and the E_b are somewhat overestimated because we neglect the kinetic-energy loss of the PIREB within the window. It is found that the peak power of the PIREB irradiated onto the soil sample reaches 0.6 GW. We have also found that the E_b in each pulse of the
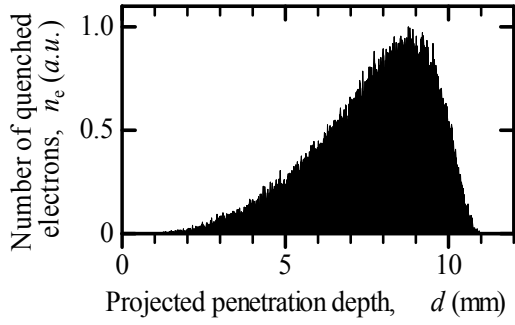
Fig. 7   Typical projected penetration depth on 2-MeV electrons into soil sample.
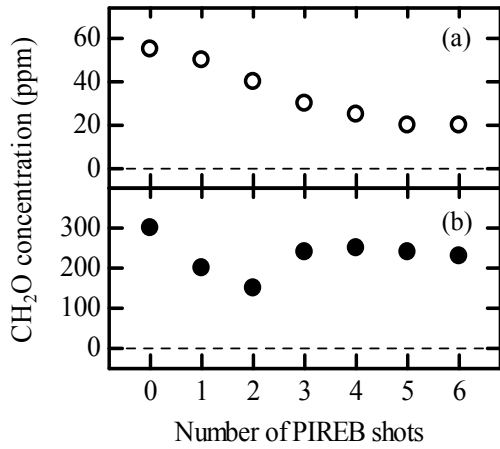
Fig. 8.   Concentration of formaldehyde (CH$_2$O) evolved from soil sample into treatment chamber as a function of number of PIREB shots for initial concentration of (a) 55 ppm (○) and (b) 300 ppm (●).
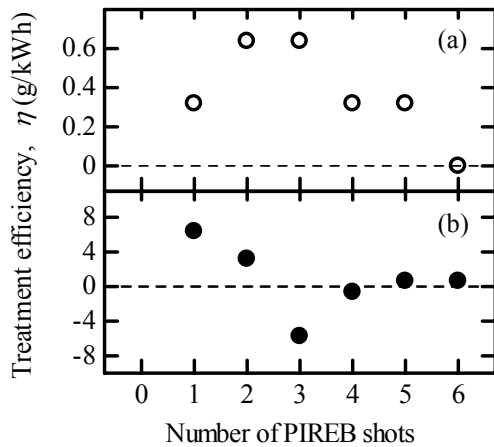
Fig. 9. Net treatment efficiency of formaldehyde (CH$_2$O) η as a function of number of PIREB shots for initial concentration of (a) 55 ppm (○) and (b) 300 ppm (●).

PIREB is estimated to be 2.1×10^{-5} kWh which is represented as only 76 J.

To confirm the active range of polluted-soil treatment within the chamber, we have calculated the electron trajectories in the soil sample. Figure 7 shows the typical projected penetration depth (d) on 2-MeV electrons into the soil sample calculated with CASINO Monte Carlo program,[7] where d is determined as the depth from the surface of the soil sample. In the CASINO program, the sample model is given by the composition and the density of the soil sample mentioned in Table I. Here, number of electron trajectories simulated is 2000, and the electrons are injected perpendicular to the soil sample. We can see from Fig. 7 that the electrons penetrate the soil sample. The maximum penetration depth reaches 11 mm. The most part of electron loses its energy within d = 5-10 mm. It indicates that the treatment reaction may occur actively under the surface of soil.

C. VOC treatment by PIREB irradiation

Figure 8 shows the concentration of CH$_2$O as a function of number of the PIREB shots for the initial concentration of 55 ppm and 300 ppm. It is found from Fig. 8(a) that in the thin CH$_2$O condition, its concentration rapidly decreases with an increase in number of the PIREB shot. Here, 64 % of the CH$_2$O is resolved by 5 shots of the PIREB irradiation. In the dense CH$_2$O condition (see Fig. 8(b)), its concentration decreases from 300 ppm to 150 ppm until the second shot of the PIREB irradiation. We have confirmed that the PIREB has ability to treat the VOC in the soil regardless of the initial concentration of formaldehyde. At the third shot of the PIREB irradiation for the initial concentration of 300 ppm, however, the CH$_2$O increases suddenly in concentration. Although the PIREB irradiation is continued, hereafter, the CH$_2$O concentration remains at constant. The precise solution to the cause of this behavior could not be obtained.

Figure 9 shows the net treatment efficiency of CH$_2$O (η) as a function of number of the PIREB shots for the initial CH$_2$O concentration of 55 ppm and 300 ppm. Here, the η is the net efficiency considering the PIREB kinetic energy only, thus, the η is defined as

$$\eta = \frac{q}{E_b},\qquad(1)$$

where q is the amount of mass of CH$_2$O removed within each shot of the PIREB irradiation. It is found that η tends to decrease with decreasing the CH$_2$O concentration except for the third and the fourth shot of the PIREB irradiation in the initial concentration of 300 ppm (cf. Fig. 8). We have found from Fig. 9(a) that η is slightly low in the thin CH$_2$O concentration. It is seen from Fig. 9(b) that η reaches

6.4 g/kWh at the first shot of the PIREB irradiation. This value seems to be somewhat low for the practical treatment of polluted soil in the field. To apply the PIREB irradiation to practical treatment, it is necessary to continue studying the improvement of treatment efficiency.

V. Conclusion

Conclusions obtained from the studies of the treatment of polluted-soil by the PIREB irradiation can be summarized as follows.

1) The volatile organic compound contained in the soil sample has been treated by the irradiation of the PIREB (2 MeV, 0.4 kA, 70 ns).

2) In the initial concentration of formaldehyde of 55 ppm, 64 % of the diffused formaldehyde within the treatment chamber is removed by firing 5 shots of the PIREB irradiation.

3) The net energy efficiency of formaldehyde removal has been found to be 6.4 g/kWh at the first shot of the PIREB irradiation in the initial concentration of 300 ppm.

The investigation of the detailed mechanism of formaldehyde treatment in the soil by the PIREB irradiation is the subject for a future study.

References

1) G. Imada and K. Yatsui, "Removal of Nitrogen Oxide in Spatially Isolated Chamber by Pulsed Intense Relativistic Electron Beam", IEEE Trans. Plasma Sci. 31(2), 295-296 (2003).

2) G. Imada and K. Yatsui, "Characteristics of Treatment of Diesel Flue Gas by Irradiation of Pulsed, Intense Relativistic Electron Beam", IEEE Trans. Plasma Sci. 34(1), 88-94 (2006).

3) ESTAR: Database for calculating stopping-power and range tables for electrons, M. Berger, S. Couresy, A. Zucker, and J. Chang (1999). [Online available: http://www.nist.gov]

4) A. Tokuchi, N. Ninomiya, G. Imada, Q. Zhu, W. Jiang, K. Masugata, and K. Yatsui, "Development of High Energy Induction Accelerator, "ETIGO-III"", Proc. 12th Int'l Conf. on High-Power Particle Beams, Haifa, Israel, 175-178 (1998).

5) Y. Oda, T. Matsuda, S. Seino, T. Ikegaki, G. Imada, W. Jiang, and K. Yatsui: "Electron Energy Measurement for Induction Linear Accelerator "ETIGO-III"", Proc. 13th Int'l Conf. on High-Power Particle Beams, Nagaoka, Japan, **2**, 544-547 (2001).

6) G. Imada, N. Morishima, and K. Yatsui, "Characteristics of Ozone Production by Intense, Pulsed Relativistic Electron Beam", Proc. 30th IEEE Int'l Conf. on Plasma Sci., Jeju, Korea, 286-289 (2003).

7) CASINO: Monte Carlo program for simulating electron trajectory in solid, D. Drouin, A. Couture, D. Joly, X. Tastet, V. Aimez, and R. Gauvin (2000). [Online available: http://www. gel.ushrbrooke.ca/casino/]

DYNAMICS OF LASER-ASSISTED DISCHARGE PLASMS
FOR EUV SOURCES

Sunao Katsuki, Nobufumi Tomimaru, Hideki Imamura, Takashi Sakugawa, Takao Namihira
and Hidenori Akiyama

Graduate School of Science and Technology, Kumamoto University
39-1 Kurokami 2-chome, Kumamoto City, Kumamoto 860-8555, Japan

ABSTRACT

This paper describes the dynamics of laser-assisted discharge plasmas for an extreme ultraviolet (EUV) source. A pulsed laser light was focused on the tin cathode surface to form vapor jet across 5 mm long anode-cathode gap where pulsed power was applied later on. Time-resolved EUV photography was conducted by using a gated EUV pinhole camera in addition to visible high speed photography. The measurement shows that the EUV is emitted only from the neck of the plasma, which is as a result of $m = 0$ magnetohydrodynamic (MHD) instability. The hot neck plasma starts showing up near the laser spot on the cathode and moves away from the cathode. This movement of the neck plasma results in the enlargement of the EUV emissive region acting as its source.

I. Introduction

A Z-pinch plasma is one of the candidates of extreme ultraviolet (EUV) sources for the next generation of semiconductor lithography[1,2]. Both the huge radiation power exceeding 180 W at wavelength of 13.5 nm in 2% bandwidth and the one year operation without maintenance are required for its commercial use. There are several key technologies to approach the commercial EUV source. Tin is the most efficient target material for 13.5 nm emission[3,4]. The rotating disc electrodes (RDE) technology[5,6] is capable of handling the huge amount of heat exceeding 50 kW due to electrical input and preventing serious electrode consumption. The laser-assisted discharge (LAD) technology[5,6] helps to produce a localized dense gas distribution near the solid or liquid target surfaces, which enables to compress the plasma quickly and efficiently in comparison with conventional gas-fed Z-pinches[7,8]. The localized gas distribution also results in stabilizing the location of high density hot plasmas. In order to improve the conversion efficiency (CE)

from the energy consumption in the plasma to the EUV emission yield, it is important to know the plasma dynamics and how the EUV emission takes place. This letter describes the dynamics of a laser–assisted discharge plasmas based on time-resolved visible and EUV photography. It also discusses a direction to improve the CE.

II. Experimental Setup and Procedure

FIG 1 shows a coaxial birdcage discharge head, which enables us to optically access the plasma easily. The discharge head consists of a planer tin cathode and a 6 mm diameter stainless steel ball anode. 7 ns long pulsed laser light (532 nm, Nd:YAG, Minilite, Continuum) was irradiated with a fluence of 10^{10} W/cm^2 to the cathode surface to deliver tin vapor jet across the 5 mm electrode gap. FIG. 2 shows the over all diagram of the experimental system. Voltage application to the gap was delayed a certain time from the laser irradiation because the ablated tin vapor jet expands dynamically and it takes hundreds ns to form the distribution for the breakdown.

In this paper we define *dt* as the time interval between the laser irradiation and the breakdown, which is one of the key factors for the plasma formation. 300 ns is the minimum value for *dt* to produce stable and reproducible discharge for the experimental condition. No discharge occurs at *dt* smaller than 250 ns. The minimum value of *dt* for the stable operation depends mainly on the gap distance, the laser irradiation fluence as well as the target material. The plasma was driven by a low inductance circuit with 42 nF capacitor bank, which is charged up to 27 kV by a repetitive pulsed power generator. The repetition rate of the operation was 10 Hz, which is determined by the laser device. The EUV emission intensity was monitored by a fast EUV photodiode (AXUV5, IRD) after passing through a spectrum band pass filter (2% at 13.5 nm) using two silicone/molybdenum multilayer mirrors. The plasma current was monitored using a calibrated pickup coil. A high speed camera (Quick E, Stanford Scientific Research) was employed to observe the visible emission from the plasma. A gated EUV pinhole camera was developed to obtain the time-resolved

EUV images of the plasma. A 50 μm diameter pinhole was covered by a 200 nm thick zirconium film to specify the wavelength range between 4 and 17 nm. The EUV emission was visualized by a two-staged micro channel plate (MCP, Hamamatsu) with a phosphor screen. The MCP was driven by a 5 ns and 2 kV handmade pulse generator based on the semiconductor driven Marx circuit[9]. Since both visible and EUV cameras work as single frame operation, a set of sequential images was obtained by the combination of images at different times in different shots, based on the reproducibility of the operation.
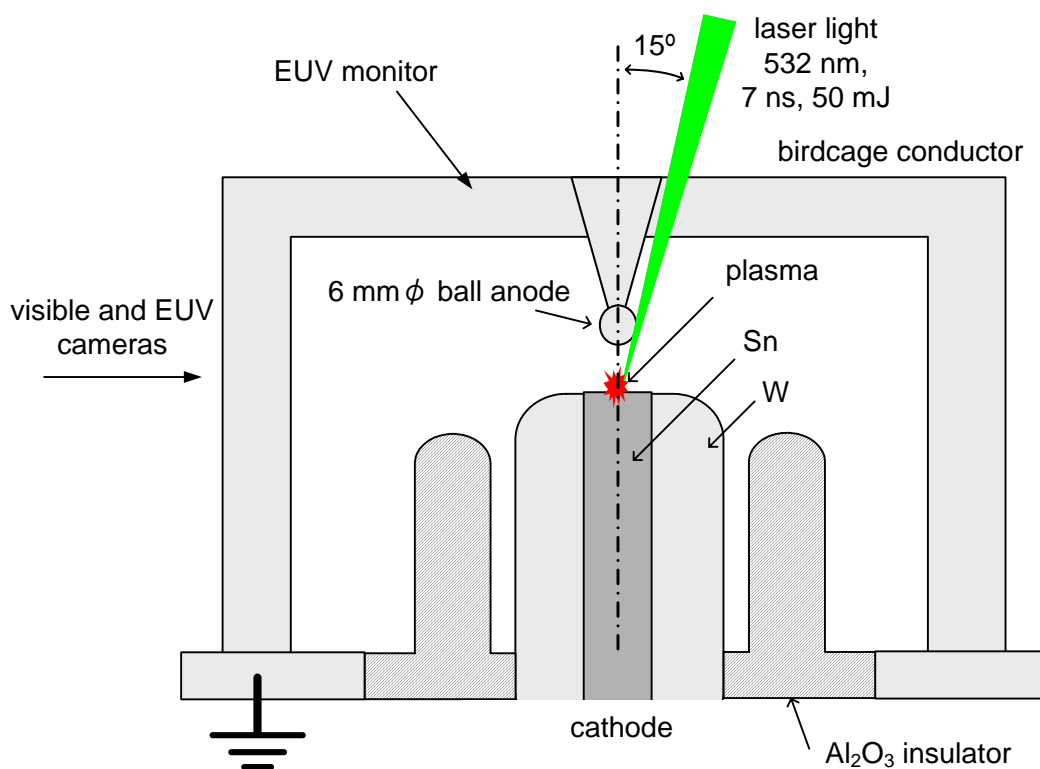
FIG. 1   Birdcage discharge head for the laser-assisted discharge.
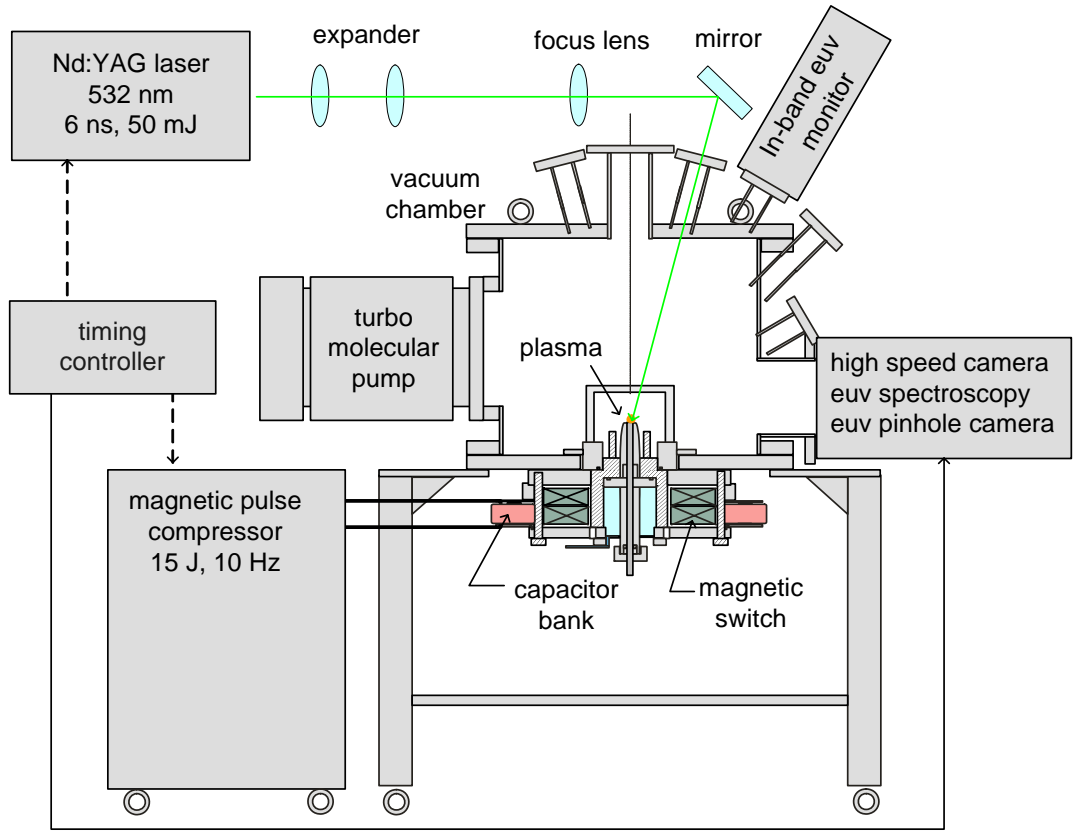
FIG. 2   Experimental setup.

IV. Results and Discussion

FIG. 3 shows the waveforms of the plasma current I_p and the signal of the EUV monitor for $dt = 300$ ns. $t = 0$ indicates the time when the current starts to increase rapidly. The EUV emission begins immediately after the current starts flowing through the plasma, and the strong emission occurs when the current becomes the maximum. The early emission is owing to the localization of gas achieved by the LADP technology. The LADP technology enables us to use extremely short current pulses to drive pinch plasmas efficiently, while the conventional gas-fed discharge needs long pulses to gather low density gas.

FIG. 4 shows the sequential time-resolved visible images of the plasma observed from the horizontal direction. The number shown in each image is identical to the time in FIG 3. At $t = 10$ ns, the emission is localized near the laser spot even after the time more than 300 ns passed from the laser

irradiation. A weak emission, which is similar to an anode column in the low pressure direct current discharge, connects the bright part to the anode. A strong pinch occurs near the laser spot on the cathode at approximately $t = 50$ ns, which is due to the $m = 0$ magnetohydrodynamic (MHD) instability[7]. Afterward the bright spot moves away from the cathode, while another plasma shows up and covers the cathode surface. A thin neck bridges two plasma clouds, and the neck moves away from the cathode together with the clouds. Finally the neck disappears at approximately $t = 110$ ns when the EUV emission is fading away. During the EUV emission the voltage of 20 kV is across the anode-cathode gap. Most of the voltage seems to occur along the neck between the clouds, resulting in the generation of huge electric field of the order of 1 MV/cm. The electric field accelerates both electrons and ions inversely between the clouds. The accelerated electrons collide with the dense gas cloud in the anode column, and the ions

bombard the cathode surface, resulting in the surface plasma showing up after $t = 65$ ns. This exploding plasma lasts for several microseconds even after the current flow ends.

FIG. 5 shows the time-integrated and sequential time-resolved EUV images of the plasmas for the same condition as those in FIGs 3 and 4. Sight of each image is identical to the rectangular box region in the left-hand image in FIG 4. Repetitive 50 shots were accumulated in each image. The time–integrated image shows EUV emissive region is widely distributed between the anode-cathode gap. Approximately 60 % of the total emission takes place at the 1.1 mm long filamentary region near the cathode, which is quite stable and reproducible. According to the time-resolved images, the EUV emission began to occur near the laser spot at $t = 50$ ns, afterwards the EUV emissive region moved away from the cathode. Instantaneous size of the EUV emissive region at $t = 80$ ns is 700×300 $(\mu m)^2$. The EUV emission faded away at approximately $t = 120$ ns. This movement coincides with that of the plasma neck in FIG 4. During the movement, the EUV emission became intense in the range including 65 and 80 ns, when also the plasma current was at the maximum level. The current density in the neck plasma is estimated to be 30 MA/cm^2. The observation suggests the possible driving force of the hot plasma movement should be the zipper effect [7]. Variation of the intensity of the images is consistent with the EUV emission intensity measurement shown in FIG 3. The comparison between the visible and EUV images indicates that EUV emission occurs only from the neck between the clouds and neither from the anode column nor from the cathode surface plasma.
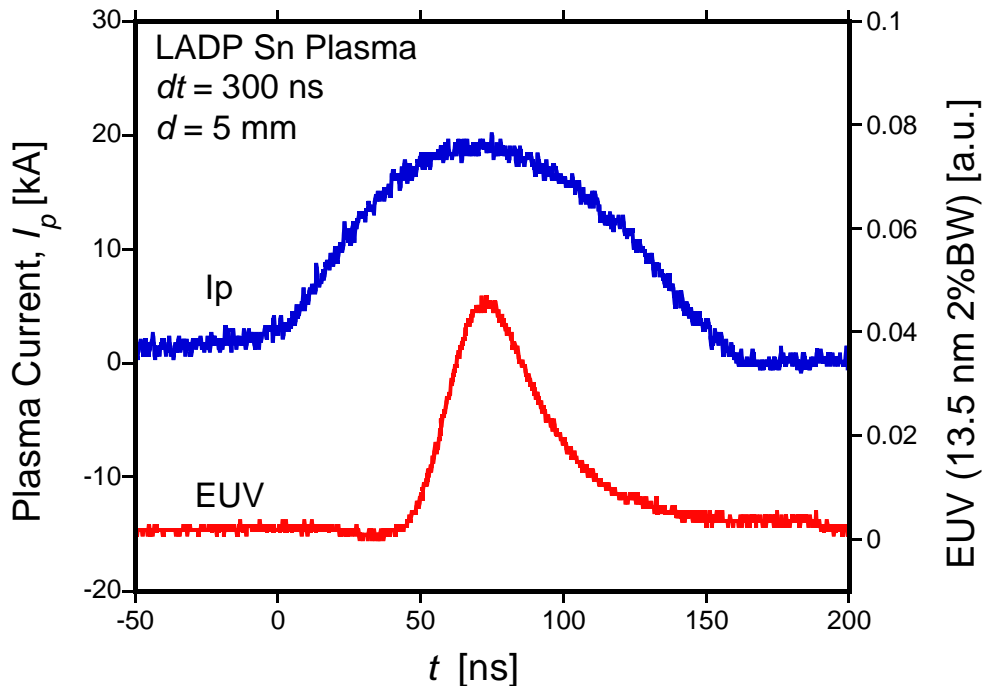
FIG. 3   Waveforms of the plasma current and the EUV emission intensity.
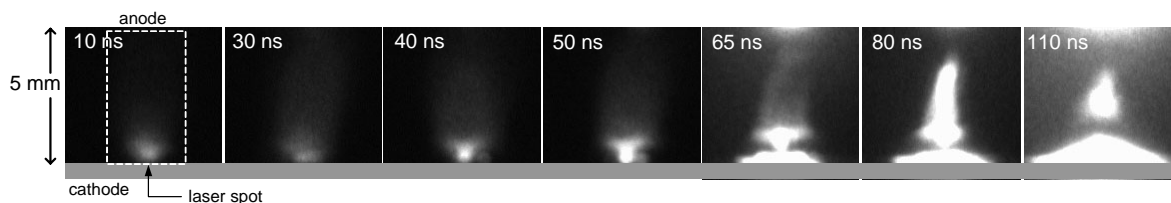
FIG. 4. Temporal variations of visible images of the laser assisted discharge plasmas taken by high speed camera with an acquisition time of 2 ns. The number in each image shows the time identical to that in FIG 3.
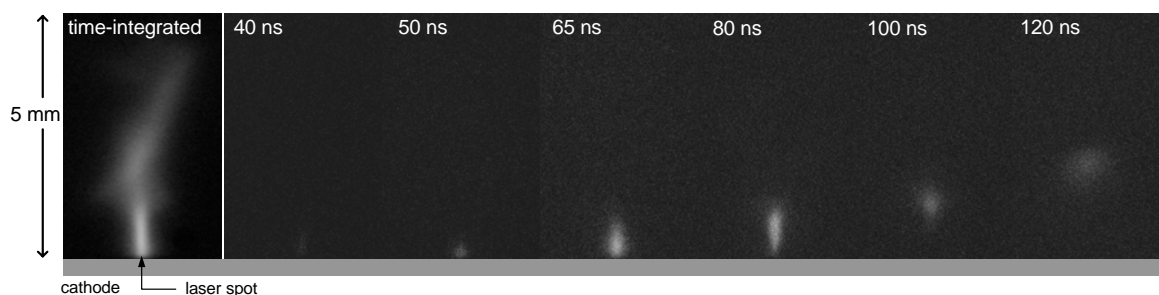
FIG. 5.   A time-integrated EUV image (LEFT) and temporal variations of EUV images of the laser assisted discharge plasmas taken by a gated pinhole EUV camera. Time resolution is 5 ns. 50 shots are accumulated in each image. The number in each image shows the time identical to that in FIG 4.

V. Conclusion

In conclusion, the time-resolved observation indicates that the laser–assisted discharge plasma behaves dynamically during the discharge. The EUV emission occurs at the hot neck part of the plasma, which moves along the anode-cathode gap. This movement of the hot plasma enlarges the EUV emissive region, which is not favorable for EUV sources. The suppression of the dynamic behavior of the hot plasma would reduce the source size and improve the conversion efficiency.

Acknowledgement

References

1) V. Banine, R. Moors, Proceedings of SPIE, 4343, 203-214 (2001)

2) V. Bakshi (ed), EUV Sources for Lithography, SPIE, Bellingham (2005)

3) G. O'Sullivan, P.K. Carroll, J. Opt. Soc. Am. 71, 227 (1981).

4) M. Lysaght, D. Kilbane, N. Murphy, A. Cummings, P. Dunne, G. O'Sullivan, Phys. Rev. A 72, 014502 (2005)

5) V.M. Borisov, J. Phys. D: Appl. Phys. 34, 3254-3265 (2004)

6) J. Jonkers, Plasma Sources Sci. Technol. 15, S8-S16 (2006)

7) M.A. Liberman, J.S. De Groot, A. Toor, R.B. Spielman, Physics of High-Density Z-Pinch Plasmas, Springer-Verlag (1998)

8) S. Katsuki, A. Kimura, Y. Kondo, H. Horita, T. Namihira, T. Sakugawa, H. Akiyama, J. Appl. Phys. 99(1), 013305 (2006)

9) T. Heeren, T. Ueno, D. Wang; T. Namihira, S. Katsuki, H. Akiyama, IEEE Trans. Plasma Sci. 33 (4), 1205 - 1209 (2005)

PHOSPHATIDYLSERINE TRANSLOCATION INDUCED BY INTENSE BURST RADIO FREQUENCY ELECTRIC FIELDS

Naoyuki Nomura, Ryoichi Hayashi, Masahiko Yano, Kazunori Mitsutake, Sunao Katsuki
and Hidenori Akiyama

Graduate School of Science and Technology, Kumamoto University
39-1 Kurokami 2-chome, Kumamoto City, Kumamoto 860-8555, Japan

ABSTRACT

This paper describes phosphatidylserine (PS) translocation in HeLa cells induced by intense burst of sinusoidal electric field (IBSEF). 200 kV/m, 50 MHz IBSEF with a burst duration of 0.2, 2 or 5 ms was applied to HeLa cells. The apoptotic activity was detected by a double staining method using annexin V-FITC and propidium iodide. The experiment shows the 2 or 5 ms long IBSEF, which gives both thermal and non-thermal effects, induced the PS externalization immediately after the exposure, while 0.2 ms long IBSEF, which is supposed to be a non-thermal exposure, induced the PS externalization gradually in time of hours, which is different from that induced by an electric pulse with a duration of nanoseconds.

I. Introduction

In the last decade biological effects of wide and narrow band electrical pulses have been intensively investigated. It is known that pulsed electric fields (PEFs) with a pulse duration exceeding 1 μs cause an increase in the permeability of cell membrane, i.e. electroporation. As the duration and the rise time of PEF are decreased to nanoseconds range, the cell response changes. Recent studies have confirmed theoretical predictions that ultra-short, high-field electric pulses can induce intracellular responses such as eosinophil sparklers[1], calcium bursts[2,3], apoptosis related reactions[3-5] in the absence of membrane permeabilization and other effects associated with electroporation. Although nanoelectropulsed cells are not porated by conventional measure, membrane phospholipid scrambling is consistently observed, indicating that nanosecond pulsed electric fields can modify the organization of the plasma membrane. Some cell types recover from the disturbance[6]. In others the distress display of phosphatidylserine (PS) on the external face of the cell persists and additional signs of nanoelectropulse-induced apoptosis appear[7]. PS externalization–the translocation of PS from its normal position on the cytoplasmic face of the plasma membrane to the exterior of the cell – has been extensively studied, as a diagnostic sign of apoptosis[8,9] and as a component of other physiological processes associated with cell senescence and phagocytic removal[10]. The ability to activate this signal remotely, with non-ionizing, non-thermal (high power, but low total energy), non-invasive electric pulses may be useful in both research and clinical settings. Because PS translocation is an early event in nanoelectropulse-induced apoptosis[11], and because considerable progress has been made toward characterization of the biophysics and physiology of this phenomenon[12], an investigation of pulse induced PS externalization should illuminate proposed mechanisms for PS transbilayer migration and provide at the same time information about the responses of cells to nanosecond pulsed electric fields. The PS translocation is immediately associated with the application of the pulse and that it is a field-driven

event, with no more than a few milliseconds intervening between the arrival of the pulse edge and the appearance of PS molecules on the external face of the cell.

We have proposed the use of Intense Burst Sinusoidal Electric Field (IBSEF)[13] as a narrow frequency band electric field instead of rectangular pulses of which the frequency spectrum is rather broad. The IBSEF enables to give a well-defined electric field in terms of frequency, amplitude and exposure time to biological targets. In our previous work we have experimentally demonstrated that non-thermal 50 MHz IBSEF with a moderate amplitude of the order of 100 kV/m and a burst duration of 0.1 ms causes the denaturalization of intracellular DNA for Chinese hamster ovary cells. The frequency of 50 MHz is sufficiently high for the electric field to penetrate through the cell membrane. Our interests are now focused on the mechanisms of the DNA denaturalization by the intracellular electric field in addition to the possibility of the apoptosis induction by using IBSEF for the purpose of cancer therapy. This paper describes the phosphatidylserine (PS) translocation, which is one of the indications of apoptosis, on HeLa cells (human womb neck cancer cells) exposed to the IBSEF.

II. Field Distribution under Alternating Voltage

Intense and short duration electric fields of both wide and narrow band frequency spectra are capable of giving unique effects to mammalian/eukaryotic cells since the biological systems are complex of the dielectric materials including organelles, lipid bilayers, various kinds of macromolecules with three dimensional structure and small molecules. Each of them is likely to have a peculiar dielectric response to alternating current (AC) external electric fields. In particular, the biological membrane works as an insulating dielectric film, which insulates the interior from the environments. FIG. 1 contains a simplified model of spherical mammalian cells, which consists of cell and nuclear membranes, cytoplasm and nucleus. Other organelles and floating molecules are excluded for simplification. This model is appropriate to discuss how much field strength takes place inside the cell. A 10 μm diameter isolated cell is suspended in the saline solution between parallel electrodes of which the separation is 20 μm. Electrical and dimensional parameters of the cell are cited from (6). Because of the limited spatial resolution, the membranes are set to be 4 times as thick as the actual value (7 nm). The voltage of 4 V corresponds to the average electric field of 200 kV/m. The field calculations are based on the finite element method for various frequencies and are summarized in FIG. 1. Electric fields were probed at cell membrane, cytoplasm, nuclear membrane and nucleoplasm. In the low frequency range below hundreds kHz, most of the voltage applied between the electrodes comes across the cell membrane since the cell membrane interrupts the conduction current. At frequency around 10 MHz the field penetrates into the cell and becomes maximum level at the nuclear membrane. The voltages across the membranes become less with increasing frequency in the range above 10 MHz. Above 100 MHz, the distribution of the electric field is determined by the dielectric constants, resulting in the larger error of the calculation due to the use of thicker membrane. FIG. 1 indicates that we can introduce the electric field into the interior of the cell by choosing the frequency to be more than 10 MHz. Since the intracellular electric field can be a stress which biological cells usually do not experienced, the new biological reactions are expected to happen.

III. Materials and Methods
A. Cell lines and culture conditions

HeLa cells (ATCC CCL2) were cultured with alpha modified eagle minimum essential medium (αMEM, Gibco) at 37°C in a humidified, 5% carbon dioxide atmosphere[14]. The cells are incubated routinely every two days before the cell culturing condition becomes 90% confluent. The cultured cells are washed twice using phosphate buffered saline (PBS), trypsinized by 10% trypsin / ethylenediaminetetraacetic acid (EDTA) solution, and resuspended 10^6 cells/ml with αMEM.

Table 1   Electrical properties of Mammalian Cell [14].

Parameters	Values
Electrode separation	20 μm
Voltage amplitude	4 V
Cell diameter	10 μm
Nuclear diameter	6 μm
Suspending medium	$\varepsilon_r = 80$, $\sigma = 1.38$ S/m
Cell membrane*	thickness = 30 nm, $\varepsilon_r = 25$, $\sigma = 2.0 \times 10^{-6}$ S/m
Nuclear membrane*	thickness = 40 nm, $\varepsilon_r = 41$, $\sigma = 3.0 \times 10^{-3}$ S/m
Cytoplasm	$\varepsilon_r = 60$, $\sigma = 0.48$ S/m
Nucleoplasm	$\varepsilon_r = 120$, $\sigma = 0.95$ S/m

* Because of the limited spatial resolution, the membranes are set to be 30 nm, which is approximately 4 times as thick as actual value (7 nm).
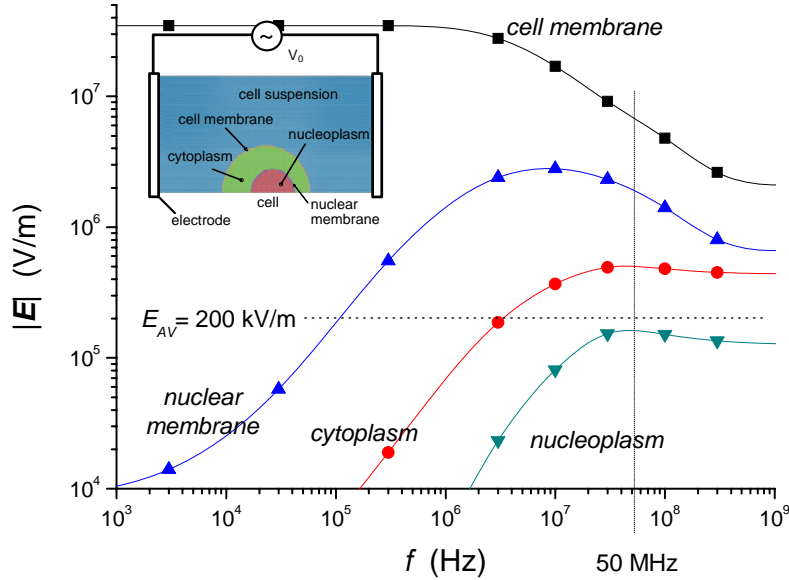
FIG. 1   Electric field distribution inside and outside biological cell membrane under alternating electric fields as a function of frequency. The average field strength is 200 kV/m.

B. Pulse generator and pulse exposures

The IBSEF exposure system, as shown in FIG. 2, consists of a signal generator (E4428C, Agilent Technologies) to provide a sinusoidal wave, a pulse generator (DG535, Stanford Research Systems) to determine the pulse duration, and an amplifier (Model 2072, EMPower RF System). The generator is connected to an exposure chamber via a 50 Ω resistive coaxial cable. The cell consists of two parallel square platinum plates as electrodes, of which the separation and cross section are 1 mm and 16 mm², resistively, forming an approximately 50 Ω resistive load. The capacitance of the electrodes was estimated to be 5 pF. The temperature increase of the suspending medium due to ohmic heating is approximately 1°C for the application of one pulse of 200 kV/m, 200 μs IBSEF. The voltage between the electrodes was monitored by a 500 MHz voltage probe (Tektronics, P6139A) at each shot. The suspension including HeLa cells was poured into the exposure chamber and was exposed to 200 kV/m, 50

36
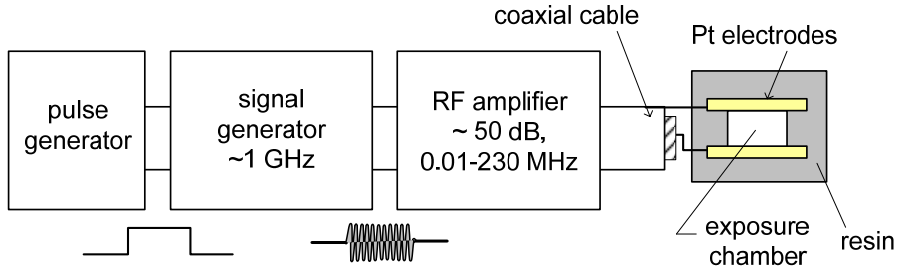
FIG. 2   Schematic diagram of the IBSEF exposure system.

MHz IBSEF with a specified burst duration. The frequency of 50 MHz enables to reduce the voltage across plasma membrane and to introduce an intense electric field to interior of the cell. The electric field of 200 kV/m is sufficiently large to cause the intracellular effect[13]. All experiments except for the incubation were conducted at room temperature (25 °C).

C. Time-lapse microscopy

The proliferation activity of the IBSEF exposed cells was observed using a time-lapse microscopy (DMI6000B, Leica) with an incubation chamber (Tokai Hit) on the stage. The IBSEF exposed suspension was scattered onto one of the partitioned culture plates in the incubation chamber. The chamber was kept at 37°C in a humidified, 5% carbon dioxide atmosphere. In order that HeLa cells adhere to the bottom, the observation was conducted at 5 hours after the IBSEF exposure. The system takes microscopic snapshots at several points simultaneously every 15 minutes for 77 hours.

D. Apoptosis detection

Phosphatidylserine (PS) is a phospholipids nutrient usually hidden in the inner-leaflet cell membranes. In an early phase of apoptosis, the PS transports to the outer-leaflet of the plasma membrane. Labeling the PS by Annexin-V-FITC enables to visualize cells in the early-to-mid phase of apoptotic cells. Propidium Iodide (PI), a fluorescent dye which is permeable to the cell, was used simultaneously to detect dead cells. The IBSEF exposed cells were incubated. At 0 (actually 15 minutes), 2 or 5 hours after the exposure, the cells were stained with both annexin V-FITC and PI (both

from WAKO) simultaneously, which fluorescence in 526 nm and 650, respectively, and afterwards were observed using a fluorescent microscopy (DMI6000B, Leica).

IV. Results
A. Time-lapse microscopy

FIG. 3 shows the microscopic snapshots of the IBSEF exposed HeLa cells cultured in the incubation chamber for approximately 60 hours. FIGs. 3(a), 3(b) and 3(c) show control, 0.2 and 5 ms long IBSEF exposed cells, respectively. HeLa cells are adhesive and are likely to attach to the glass surface of the culture dish. From the sequential observation of the images, we identify the dead cells, which have not moved for a long time. In the control sample the cells are almost confluent even some are still actively in the division phase. The number of cells exposed to the IBSEF is much less than the control, and some are dead. We counted the living cells in the snapshot images and summarized the time-lapse observations in FIG. 4. It is noted that the cell number is shown in log scale. It is natural that the number of cells increases exponentially in the nutrition rich culture condition, so we can assume the growth rate of cell number as

$$N = A\exp(Bt) \qquad (1)$$

where A is a constant depending on the initial condition, and B is the cell growth rate, which is indicated by the slope of the growth curve. The time to double the cell number, so called the doubling time, can be obtained by $\ln2/B$. The constant B and the doubling time are obtained by fitting equation (1) to the growth curve. In the control sample, the growth curve is a little saturated around $t = 50$ hours. This is

because the culture plate is nearly confluent. The growth rate and the doubling time together with the exposure condition are summarized in Table 2. The temperature increase in the medium is calculated by the energy deposition. However, the temperature increase should be spontaneous in time of ms range and much smaller than the values in Table 2 because of heat conduction to the electrode. The growth rate is evaluated in the time range 0 < t < 55 hours since the rates tend to be changed during the observation. The larger energy deposition is likely to suppress strongly the proliferation activity of the cells. For the samples exposed to IBSEF, their growth rates are likely to increase after several tens of hours, indicating that surviving cells appear to be recovering. The recovery time tends to be longer for larger energy deposition to the cells, and to be associated with the doubling time. These data imply that surviving cells, which are inactivated, might recover after they conduct their cell divisions. With the burst durations of 2 and 5 ms the IBSEF exposure is accompanied by a significant temperature increase for biological matter. We cannot distinguish the effect of electric field from the thermal effect in this experiment.

B. Phosphatidylserine translocation

50 MHz, 200 kV/m IBSEFs with various burst durations between 0.2 and 5 ms were applied to HeLa cells. Cells were stained with both annexin V-FITC and PI a certain time after the IBSEF application, and observed by a fluorescent microscope. Results of the double staining method were classified into three cases; (1) negative to both annexin V and PI, indicating living cells, (2) positive to annexin V and negative to PI, indicating cells in the early phase of apoptosis, and (3) positive to both annexin V and PI, indicating dead cells. FIG. 3 shows the microscopic images with bright field and fluorescence from either annexin V or PI for the negative control and for 0.2 ms long IBSEF application. FIG. 3 shows several cells with fluorescence from annexin V, while no PI fluorescent was observed. The percentage of the cells in the apoptotic process and the dead cells were evaluated by a cell counting. FIG. 4 shows a summary of the observation, cell percentage for the

case (2) and the case (3) as a function of post cultivation time after the IBSEF application. Each datum includes approximately 300 cells. The controlled cells did not show apoptosis or death during the observation. In the case of the 5 ms long IBSEF application, which is accompanied by an instantaneous temperature increase of the medium by approximately 20°C, approximately 40% of the cells showed the apoptosis immediately after the IBSEF application. After 5 hours the apoptosis ratio was decreased thus immediately activated apoptotic cells were dead. On the other hand, the application of 0.2 ms long IBSEF with a slight temperature increase of less than 1°C did not cause the PS externalization just after the exposure, while the percentage of the apoptotic cells was gradually increased to be approximately 15% after 5 hours. The delayed occurrence or the PS externalization implies that the non-thermal IBSEF does not directly cause the PS externalization, or apoptosis reaction, but is likely to trigger the biological process related to the PS externalization.

V. Discussion

According to the experiments of nanosecond rectangular pulsing to mammalian cells (Schoenbach et al. used 60 ns, 5 MV/m pulses[2,10] and Vernier et al. used 30 ns, 2.5 MV/m pulses[3]), intense nano-electrical pulsing induces nano-pore formation, resulting in the PS translocation due to the lateral molecular diffusion through the nano-pore. This PS translocation occurs immediately after the pulsing within a few seconds. External electrical pulses directly stimulate the cell membrane in this case. For the case of the fast rising pulse we can calculate the voltage across the plasma membrane, when a square wave pulse with voltage of $V_a = Ed$ is applied, where d is the distance between the two electrodes (FIG. 1), and E is the average electric field in the medium. Starting from the resting voltage V_r, which is of the order of 70 mV for many cells, the voltage across the plasma membrane increases with time until the end of the voltage pulse, and reaches a value of V_M +/- V_r at the poles given by [2]

$$V_M = fE(D/2)\{1 - \exp(-t/\tau_C)\} \quad (2)$$

(a) control   (b) 0.2 ms long IBSEF   (c) 5 ms long IBSEF
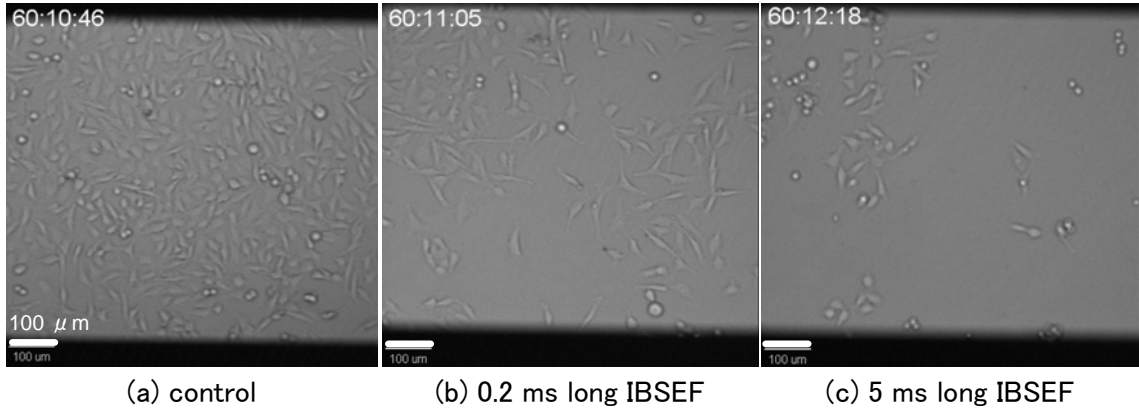
FIG. 3 Microscopic snapshots of HeLa cells approximately 55 hours after the IBSEF exposure. The number in each image shows the time from the beginning of the observation (hours:minutes:seconds).
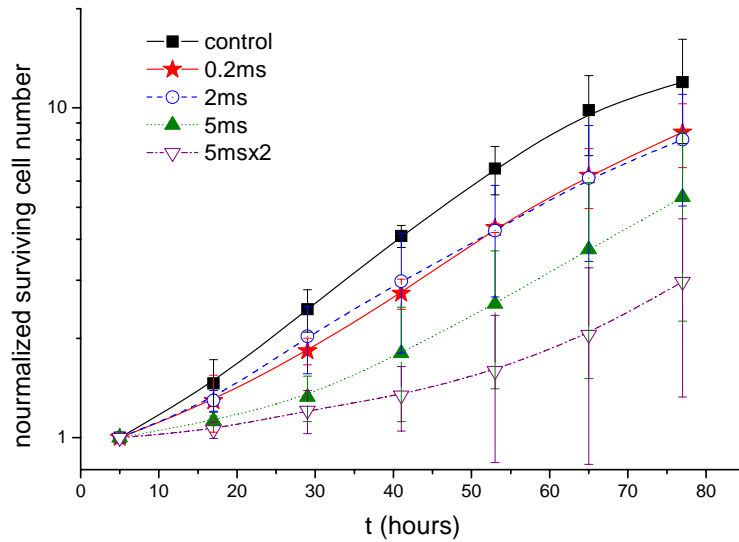
FIG. 4 Growth curves of HeLa cells exposed to 200 kV/m, 50 MHz IBSEF with application of various burst durations (one pulse of 0.2, 2, 5 ms and two pulses of 5 ms). The IBSEFs were applied at $t = 0$. The each observation starts at 5 hours after the IBSEF exposure. The cell numbers are normalized to that at 5 hours after the exposure. Each curve is the average of 5 independent trials.

Table 2 Summary of the time-lapse observation of HeLa cells exposed to the IBSEF.

Shot condition		Energy expenditure (mJ/16 μl)	Temperature increase (°C)	Growth rate B (hour^{-1})*	Doubling time (hours)*
E_{av}, f	duration × number				
	Control	-	-	0.041	17
200 kV/m 50 MHz	0.2 ms	59	0.88	0.030	23
	2 ms	590	8.8	0.028	25
	5 ms	1500	22	0.021	33
	5 ms × 2	1500 × 2	22	0.011	63

* Evaluated for the time until 50 hours.

where f is a geometry factor (1.5 for spherical cells), and D is the diameter of the cell. τ_C is the charging time constant for the plasma membrane, which is 75 ns for 10 μm diameter spherical cell floated in the 100 Ωcm resistive medium. Nanosecond rectangular pulses are extremely short duration but its frequency spectrum is broad and the electric field is in the MV/m range, resulting in the trans-membrane voltage exceeding 100 MV/m. This extremely high field forms the nano-pores, which allows only small molecules to pass thorough the pore. Molecular dynamic simulation[9] indicates that the extremely high electric field of 0.5 V/nm forms the nano-pore within only 3 nanoseconds. However, the IBSEF with moderate electric fields of 200 kV/m causes the electric field of the order of 10 MV/m on the plasma membrane, which is 1/10 for the nano-pulse application. On the other hand, high frequency alternative fields of more than 10 MHz enable to cause the intracellular electric field, which is the same level as the external electric field. This 0.2 ms lasting alternating electric field might give a stress to the cell. In the case of the 0.2 ms long IBSEF application, the PS externalization occurs gradually after the exposure, which is induced by nano-pulsing. The effect of IBSEF seems to be different from that of the nano-pulsing, and rather similar to the apoptosis process caused by conventional stimuli, such as exposure to UV, radiation, heat or chemicals.

Acknowledgement

References

1) K.H. Schoenbach, S.J. Beebe, E.S. Buescher, J. Bioelectromagnetics 22, p.440 (2001)

2) K.H. Schoenbach, et al, IEEE Trans. Dielectr. Electr. Insulat. Vol. 14, No. 5; pp.1088-1109 (2007)

3) P.T. Vernier, Y. Sunc, L. Marcua, C.M. Craft, M.A. Gundersen, Federation of European Biochemical Societies Letters 572, pp.103-108 (2004)

4) Y. Sun, P.T. Vernier, M. Behrend, L. Marcu, M.A. Gundersen, IEEE Trans. Nanobioscience, Vol. 4, No. 4, pp.277-283 (2005)

5) P.T. Vernier, A. Li, L. Marcu, C.M. Craft, M.A. Gundersen, IEEE Trans. Dielectr. Electr. Insulat. Vol. 10, No. 5; pp.795-809 (2003)

6) P.T. Vernier, Y. Sun, L. Marcu, C.M. Craft, M.A. Gundersen, Biophys. J. Vol. 86, pp.4040–4048 (2004)

7) I. Ermorina, Y. Polevaya, Y. Feldman, B. Ginzburg, M. Schlesinger, IEEE Trans. Dielectr. Electr. Insulat. Vol. 8, No. 2, pp.253-261 (2001)

8) D.A. Stewart, Jr., T.R. Gowrishankar, J.C. Weaver, IEEE Trans. Plasma Science, Vol. 32, p.1696 (2004).

9) Q. Hu, S. Viswanadham, R.P. Joshi, K.H. Schoenbach, S.J. Beebe, P.F. Blackmore, Phys. Rev. E71, 031914 (2005)

10) W. Frey, J.A. White, R.O. Price, P.F. Blackmore, R.P. Joshi, R. Nuccitelli, S.J. Beebe, K.H. Schoenbach, J.F. Kolb, Biophys. J. Vol. 90, p.3608 (2006)

11) A.G. Pakhomov, A. Phinney, J. Ashmore, K. Walker III, J. Kolb, S. Kono, K.H. Schoenbach, M.R. Murphy, IEEE Trans. Plasma Science Vol. 32, p.1579 (2004).

12) J.C. Weaver, IEEE Trans. Dielectr. Electr. Insulat. Vol. 10, No. 5, pp. 754-768 (2003)

13) S. Katsuki, N. Nomura, H. Koga, H. Akiyama, I. Uchida S.-I. Abe, IEEE Trans. Dielectr. Electr. Insulat. Vol. 14, No. 3, pp. 663-669 (2007)

14) H. He, D.C. Chang, Y.K. Lee, Bioelectrochem., Vol. 70, Iss. 2, pp.363-368 (2007)
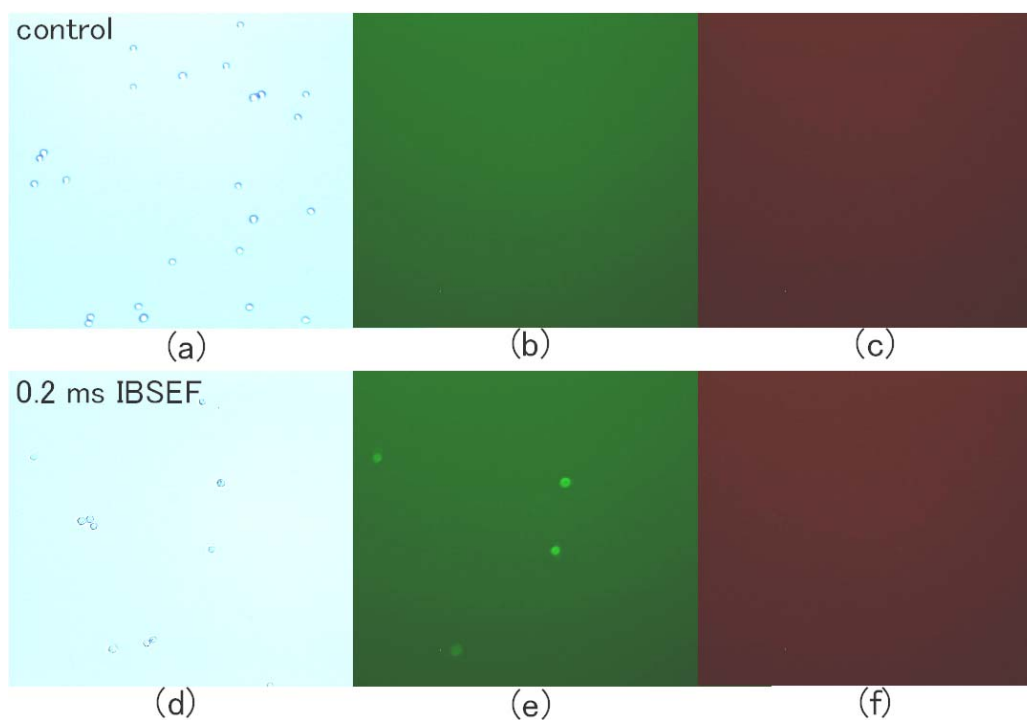
FIG. 5 Microscopic view of HeLa cells. (a) and (d) are bright field images. (b) and (e) are fluorescent images from annexin V-FITC. (c) and (f) are fluorescent images from propidium iodide. A set of (a)-(c) shows control cells, and set of (d)-(f) shows cells 5 hours after the exposure to 0.2 ms long IBSEF.
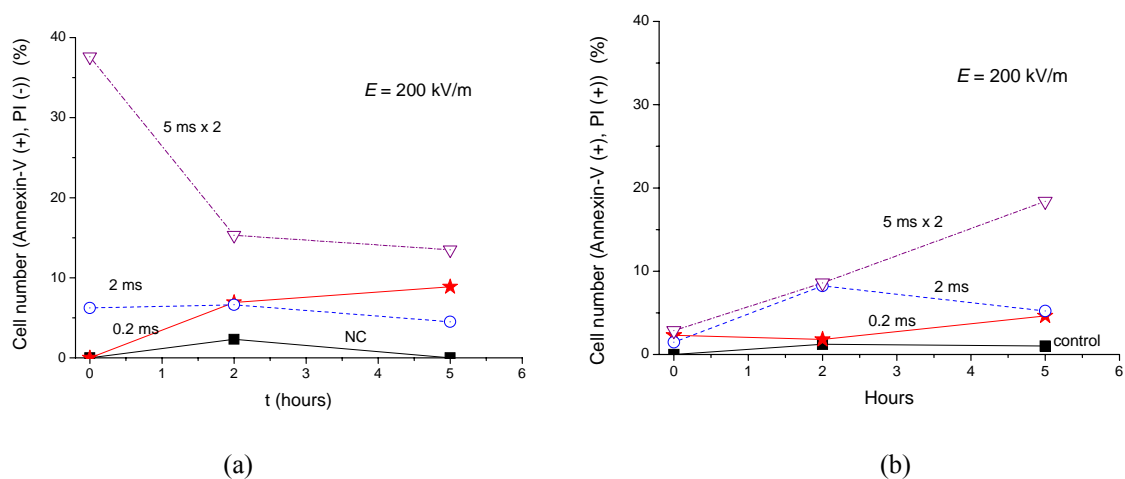
FIG. 6 Temporal variations of the percentages of the apoptotic cells (a) and dead cells (b) numbers for negative control and for the exposure to 200 kV/m, 50 MHz IBSEF with various burst duration (0.2, 2 and 5 ms ×2). Each datum represents approximately 300 cells.

EFFICIENT COLLIMATED ION BEAM PRODUCTION IN A TAILORED STRUCTURED FOIL ILLUMINATED BY AN INTENSE SHORT PULSE LASER

S. Kawata[1], Y. Nodera[1], K. Takahashi[1], A. Andreev[2], O. Klimo[3], J. Limpouch[3], Y. Ma[4], Z.M. Sheng[4], Q. Kong[5] and P. Wang[5]

[1]*Utsunomiya University, 7-1-2 Yohtoh, Utsunomiya 321-8585, Japan*
[2]*Vavilov State Optical Institute, Sankt Petersburg 199034, Russia*
[3]*Czech Technical University, Cz-115 19, Praha 1, Czech Republic*
[4]*Shanghai Jiao Tong University, Min Hang, Shanghai 200240, China*
[5]*Fudan University, Handan 220, Shanghai 200433, China*

ABSTRACT

Improvement of energy conversion efficiency from laser to proton beam is demonstrated by particle simulations in a laser-foil interaction. When an intense short-pulse laser illuminates the thin foil target, the foil electrons are accelerated around the target by the ponderomotive force. The hot electrons generate a strong electric field, which accelerates the foil protons, and the proton beam is generated. In this paper a multihole thin-foil target is proposed in order to increase the energy conversion efficiency from laser to protons. The multiholes transpiercing the foil target help to enhance the laser-proton energy conversion efficiency significantly. 2.5-dimensional (x, y, v_x, v_y, v_z) particle-in-cell simulations present that the total laser-proton energy conversion efficiency becomes 9.3% for the multihole target, though the energy conversion efficiency is 1.5% for a plain thin foil target. The maximum proton energy is 10.0MeV for the multihole target and is 3.14MeV for the plain target. The transpiercing multihole target serves a new method to increase the energy conversion efficiency from laser to ions. The multiholes target with side walls is also proposed to produce a collimated ion beam with a high energy conversion efficiency. The side walls at the target rear side shield a divergence electric field and help to produce a collimated ion beam.

I. Introduction

In recent researches, a laser intensity of $I > 10^{20}$ W/cm^2 has been achieved by the development of a laser technology. On the other hand ion beams are useful for basic particle physics. In fact, the ion beams are used for medical therapy, controlled nuclear fusion, high-energy sources, and so on[1-11]. The ion acceleration in the laser-foil interaction is expected to be a new method of ion acceleration[12-26]. One of problems in the laser-ion acceleration is the energy conversion efficiency from laser to ions, and the energy conversion efficiency is low in actual experiments.

When an intense short-pulse laser illuminates a thin foil, electrons in the foil obtain energies from the laser and oscillate around the thin foil. In the laser-foil interaction, the behavior of the electrons influences directly the ion dynamics. A part of the electrons placed at the surface irradiated by the laser

is accelerated. The electrons form a high current and generate a magnetic field[27, 28]. The electrons form a
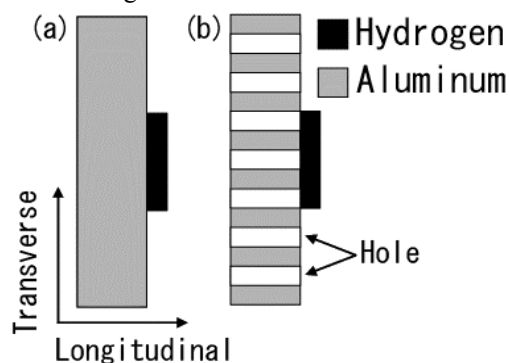
Fig. 1. Thin-foil targets: (a) a plain target and (b) a tailored microstructured multihole target. An intense short-pulse laser gives electrons its energy, and the hot electrons are accelerated. The electrons form a strong electric field, and the protons are accelerated. The target surface reflects the laser. In the multihole target, the holes transpiercing the target help to enhance the laser-proton energy conversion efficiency.
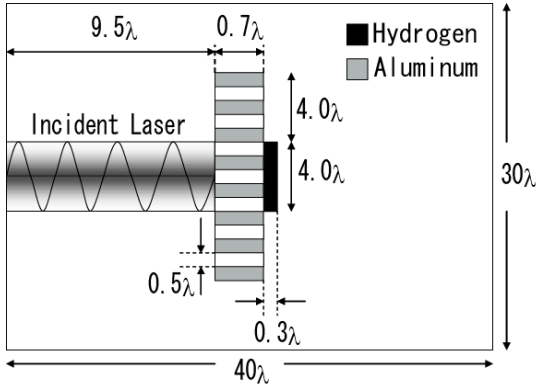
Fig. 2. A target structure used in this paper. We employ a double layer target which consists of Al and H. The Al layer has a linear density gradient in 0.5λ. The calculation area is 40λ in the longitudinal direction and 30λ in the transverse direction. There are twelve holes in the multihole target. The hole diameter is 0.5λ, and the hole distance is also 0.5λ.

strong electric field, and the ions are accelerated by the electric field. The laser gives its energy mainly to the electrons near the thin foil surface. The surface reflects the significant part of the laser energy. The energy conversion efficiency from laser to ions tends to be low. In our study, we employ an intense short-pulse laser and the double-layer hole target which consists of hydrogen and aluminum in 2.5-dimensional particle-in-cell simulations (see Figs. 1(a) and (b)). The reason why we employ aluminum is in order to prevent the target deformation. Aluminum ions are heavier than hydrogen, and the aluminum supplies electrons more than hydrogen. The maximum energy of the protons is about a few MeV in the plain target. In this paper, we perform 2.5-dimensional particle-in-cell simulations to investigate the improvement of the energy conversion efficiency from laser to protons in the laser-foil interaction[29]. We demonstrate a significant increase in the energy conversion efficiency and the maximum energy with the multihole target shown Fig. 1(b). The holes, transpiercing the foil target, help in increasing the laser energy absorption by the multihole foil target electrons[30-33].

II. Efficient Collimated Proton beam production

We investigate a significant increase in the energy conversion efficiency from laser to protons by the multihole target. The multiholes transpiercing the plain target help to enhance the energy conversion efficiency from laser to protons. The electrons in the multihole target generate the electric field stronger than that in the plain target, and the total energy of the protons and the maximum proton kinetic energy are significantly high in the multihole target. By

subwavelength micro structures[32,33], for example, the multihole target, clusters, nano-tubes, etc, the laser energy absorption is enhanced. In this paper we employ the micro structure of the multiholes to increase the laser energy conversion efficiency to protons. In the targets with microstructures, foam, carbon nano-tubes, clusters or so, the laser absorption surface becomes wider and the laser reflection and diffraction enhances the laser energy absorption efficiently[32,33]. In nature blue morpho butterfly employs the similar microstructure to absorb the sun light except the blue color. In this work we have followed the morpho butterfly microstructure to increase the laser energy absorption efficiency. In this paper we employed a normal incidence of a laser to the target surface as shown in Fig. 2.

In this paper, we perform 2.5-dimensional (x, y, v_x, v_y, v_z) particle-in-cell simulations. Figure 2 shows a conceptual diagram of the tailored micro-structured multihole target. We employ a linear density gradient in 0.5l to the target at the laser illumination surface to include a pre-pulse effect of the laser. The laser intensity is $I = 1.0 \times 10^{20}$ W/cm^2, the laser spot diameter is 4.0l, and the pulse duration is 20fs. The laser transverse profile is in the Gaussian distribution and the laser wavelength is λ = 1.053mm. In this research, we employ a double-layer target, which consists of Al and H. The heavy material Al layer prevents the target deformation and supplies more electrons compared with the H layer. The ionization degree of the Al layer is 11. The initial Al target peak density is the solid one ($n_i = 42n_c$). The H layer density is flat and $42n_c$. The initial particle temperatures are 1 KeV. Here n_c stands for the critical density. The hole size is 0.5λ and the number of holes is twelve in the target. The total energy of
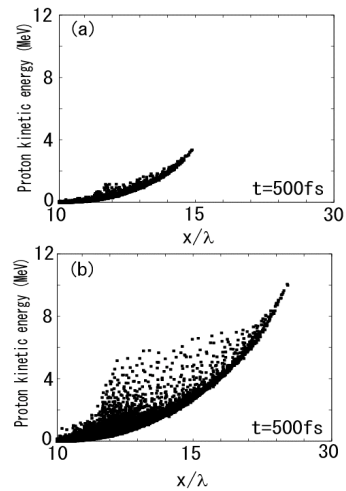
Fig. 3. Distributions of the proton kinetic energy at 500fs: (a) the plain target and (b) the multihole target. The proton kinetic energies become high significantly in the multihole target.
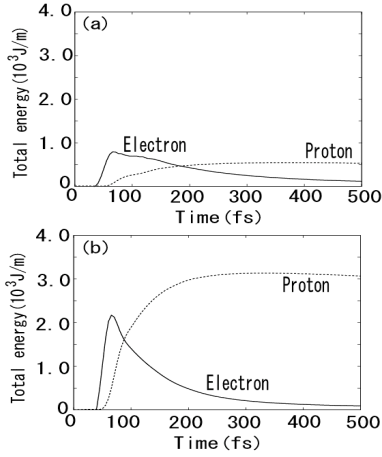
Fig. 4. Total-energy histories of the protons and electrons (a) in the plain target and (b) in the multihole target. The solid lines and the dotted lines are the histories of the electrons and the protons, respectively.

the laser in the simulation is about 3.31×10^4 J/m.

First, we demonstrate the improvement of energy conversion efficiency from laser to protons by the multihole target (Fig. 1(b)). Figures 3 show the distributions of the proton energy versus the longitudinal direction for both cases of (a) the plain target and (b) the multihole target at 500fs. The maximum energy of the protons is 3.14MeV in the plain target and is 10.0MeV in the multihole target. Figures 4 show the total-energy histories of the protons and electrons in both cases. The peak of the laser intensity irradiates the target surface at about 55fs, and the total energy of the electrons reaches the peak at about 60fs. In Figs. 4, the total energy of the protons reaches about 5.3×10^2J/m in the plain target and 3.1×10^3J/m in the multihole target at 500fs. The energy conversion efficiencies to the protons are 1.5% in the plain target and 9.3% in the multihole target. In the multihole target the laser gives the electrons its energy efficiently by the holes transpiercing the target, and the number and energy of the hot electrons increase. Figure 5 shows the hot-electron energy distributions f in both the cases at 80fs. In Fig. 5, the hot-electron temperature is 0.38MeV in the multihole target and 0.30MeV in the plain target. Figure 6 shows the histories of the accelerated-proton number in both cases, and in Fig. 6 the protons have the energy over 0.1MeV and are accelerated forward of the target. In Fig. 6 the proton number in the multihole target reaches about 2.7 times at 500fs as many as that in the plain target. In the multihole target, the strong electric field, which is about twice larger than that of the plain target, accelerates the protons significantly and contributes the increase in the accelerated-proton number. Therefore, the total proton energy is about six times as much as that in the plain target.
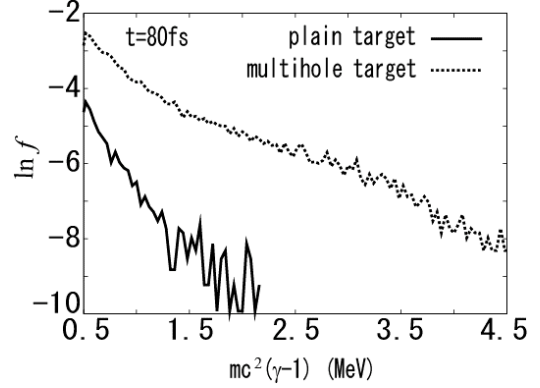
Fig. 5. Energy spectra of the hot electrons at 80fs. The solid line presents the distribution in the plain target and the dotted line shows the distribution in the multihole target.

It may be difficult to make the laser axis coincide exactly with the target center line in realistic experiments and actual uses. We investigate the effect of the change in the laser illumination point onto the multihole target. This subsection presents the simulation results for two Patterns (A and B) of the laser illumination point as shown in Fig. 7. In the Pattern A employed in the preceding subsection A, the laser axis coincides with the target center line. In the Pattern B, the laser axis coincides with the hole center. Figure 8 shows the energy spectra of the proton kinetic energy over 0.5MeV for the Patterns A and B. In Fig. 8, the spectrum for the Pattern B coincides with that for the Pattern A. The maximum energy of the protons in the Pattern B is almost the same as in the Pattern A, that is, about 9.6MeV. The total energy of the protons in the Pattern B is also almost the same as in the Pattern A. The divergence angle distributions also coincide with each other. Even if the laser axis slides on the hole target surface, the quality of the proton beam, the proton maximum energy, the proton total energy and the proton divergence distribution do not change seriously. The simulation results demonstrate the robustness of the
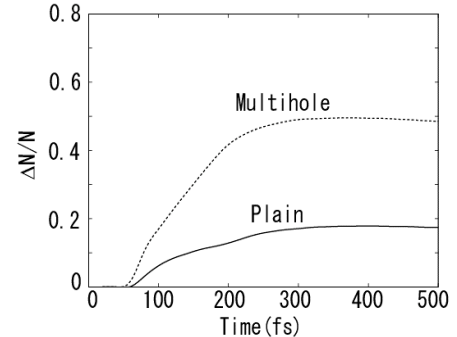
Fig. 6. Histories of the total number of the protons over 0.1MeV in the plain target and the multihole target. The solid line shows the history in the plain target and the dotted line shows the history in the multihole target. The proton number in the multihole target becomes about 2.7 times large compared with that in the plain target at 500fs.
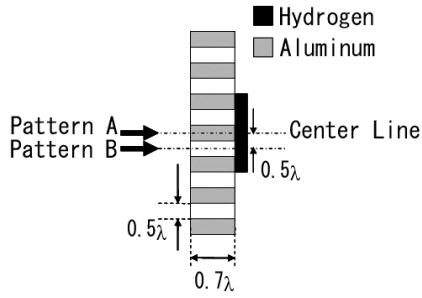
Fig. 7. The multihole target is robust against the laser alignment error. In the laser illumination "Pattern A" the laser illuminates the center of the target, and in the "Pattern B" the laser illuminates the center of the hole.

hole target against the laser alignment error.

We apply the microstructured hole target to generate a monoenergetic proton beam. In order to generate a monoenergetic proton beam, the proton layer in Fig. 1 is substituted with a CH_2 layer of the same thickness of 0.3mm[30]. As presented in Ref. 30), the protons are first accelerated and then the C ions follow the proton beam. The C beam pushes a lower energy part of the protons to generate a narrower energy spectrum (see Fig. 9). The aluminum substrate layer thickness is 1mm with the microstructure: the hole size is 190nm and the wall thickness is 60nm. The ionization degree of C is 6 in this example case. In this case the laser intensity is also $I = 1.0 \times 10^{20}$ W/cm^2, the laser spot diameter is 3.0l, and the pulse duration is 15fs. In this specific case 20% of the laser energy goes to C ions and 6% goes to protons. Totally 26 % of the laser energy is converted to high energy C and protons. When a flat target without the microstructure is employed, only 2.8% of the laser energy is converted to the ion beam energy. In addition, as shown in Fig. 10, a monoenergetic proton beam is generated efficiently[30].

III. Discussions

In this paper, we investigated a significant increase in the energy conversion efficiency from laser to protons by the tailored microstructured multihole target. The multiholes transpiercing the plain target
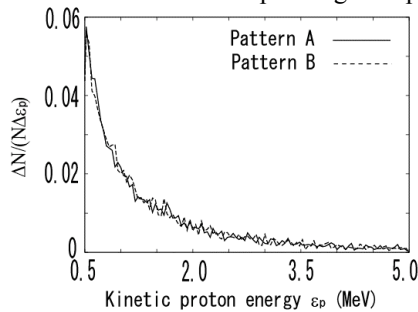
Fig. 8. Spectra of the proton kinetic energy $\varepsilon_p (> 0.5\text{MeV})$ in the Patterns A and B. The spectrum in the Pattern B coincides with that in the Pattern A.
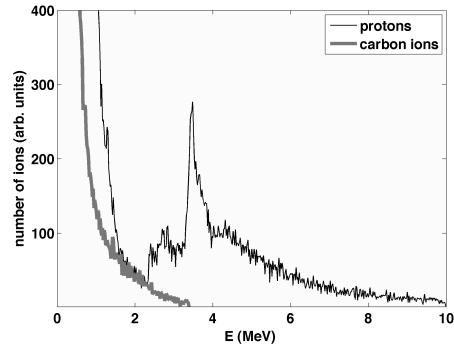
Fig. 9. A monoenergetic proton beam is efficiently generated by the tailored microstructured target with multi-species ion source. The microstructured target convertes 26% of laser energy to C ions and Protons, though the flat target converts 2.8% of laser energy to ions.

enhance the energy conversion efficiency from laser to protons. The electrons in the multihole target generate the electric field stronger than that in the plain target, and the total energy of the protons and the maximum proton kinetic energy are significantly high in the multihole target. By subwavelength microstructures, for example, the multihole target, clusters, nano-tubes, etc, the laser energy absorption is enhanced. In this paper we employ the microstructure of the multiholes to increase the laser energy conversion efficiency to protons. We also demonstrated an application of the microstructured target to a monoenergetic proton beam generation. In addition, we have also proposed another type of target to produce a collimated ion beam (see Refs. 12 and 27). In Refs. 12) and 27) the target has walls to shield a divergence transverse-electric field. By combining the wall target and the multihole target we can design a new target as shown in Fig. 10 to produce a collimated ion beam with a high energy conversion efficiency. The multihole target with the walls may serve a foil target to improve the energy conversion efficiency from
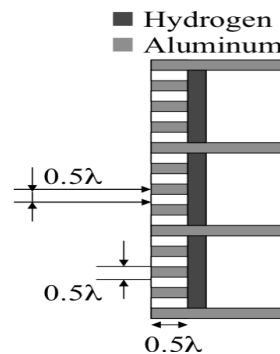
Fig. 10. A new target structure for collimated ion beam efficiently. The fine structure brings an efficient energy conversion from laser to ions, and the walls at the right side in this figure shield a divergence field to produce a collimated ion beam (see Refs. 12 and 27).

laser to ions and produce a high-energy collimated proton beam in a laser-foil interaction.

References
1) S. V. Bulanov, and V. S. Khoroshkov, "Feasibility of using laser ion accelerators in proton therapy," Plasma Phys. Rep., vol. 28, pp. 453-456, 2002.
2) M. Roth, T. E. Cowan, M. H. Key, S. P. Hatchett, C. Brown, W. Fountain, J. Johnson, D. M. Pennington, R. A. Snavely, S. C. Wilks, K. Yasuike, H. Ruhl, F. Pegoraro, S. V. Bulanov, E. M. Campbell, M. D. Perry and H. Powell, "Fast Ignition by Intense Laser-Accelerated Proton Beams," Phys. Rev. Lett., vol. 86, pp. 436-439, 2001.
3) M. Kaluza, J. Schreiber, M. I. K. Santala, G. D. Tsakiris, K. Eidmann, J. Meyer-ter-Vehn and K. J. Witte, "Influence of the Laser Prepulse on Proton Acceleration in Thin-Foil Experiments," Phys Rev. Lett., vol. 93, p. 045003, 2004.
4) Y. Sentoku, T. V. Liseikina, T. Zh. Esirkepov, F. Califano, N. M. Naumova, Y. Ueshima, V. A. Vshivkov, Y. Kato, K. Mima, K. Nishihara, F. Pegoraro and S. V. Bulanov, "High density collimated beams of relativistic ions produced by petawatt laser pulses in plasmas," Phys. Rev. E, vol. 62, pp. 7271-7281, 2000.
5) S. Ter-Avetisyan, M. Schnürer, P. V. Nickles, M. Kalashnikov, E. Risse, T. Sokollik, W. Sandner, A. Andreev and V. Tikhonchuk, "Quasimonoenergetic Deuteron Bursts Produced by Ultraintense Laser Pulses," Phys. Rev. Lett., vol. 96, p.145006, 2006.
6) A. Pukhov, "Three-Dimensional Simulations of Ion Acceleration from a Foil Irradiated by a Short-Pulse Laser," Phys. Rev. Lett., vol. 86, pp. 3562-3565, 2001.
7) A. A. Andreev, T. Okada, K. Yu. Platonov and S. Toroya, "Parameters of a fast ion jet generated by an intense ultrashort laser pulse on an inhomogeneous plasma foil," Laser and Particle Beams, vol. 22, pp. 431-438, 2004.
8) S. V. Bulanov, T. Zh. Esirkepov, J. Koga, T. Tajima and D. Farina, "Concerning the maximum energy of ions accelerated at the front of a relativistic electron cloud expanding into vacuum," Plasma Phys. Rep., vol. 30, pp. 18-29, 2004.
9) A. A. Andreev, R. Sonobe, S. Kawata, S. Miyazaki, K. Sakai, K. Miyauchi, T. Kikuchi, K. Platonov and K.Nemoto, "Effect of a laser prepulse on fast ion generation in the interaction of ultra-short intense laser pulses with a limited-mass foil target," Plasma Phys. Control. Fusion, vol. 48, pp. 1605-1619, 2006.
10) A. A. Andreev and J. Limpouch, "Ion acceleration in short-pulse laser–target interactions," J. Plasma Phys, vol. 62, pp. 179-193, 1999.
11) A. A. Andreev, T. Okada, K. Yu. Platonov and S. Toroya, "Parameters of a fast ion jet generated by an intense ultrashort laser pulse on an inhomogeneous plasma foil," Laser and Particle Beams, vol. 22, pp. 431-438, 2004.
12) M. Nakamura, S. Kawata, R. Sonobe, S. Miyazaki, Q. Kong, and T. Kikuchi, "Robustness of a tailored hole target in laser-produced collimated proton beam generation", J. of Appl. Phys., vol. 101, pp. 113305-1-7, 2007.
13) M. Hegelich, S. Karsch, G.. Pretzter, D. Habs, K. Witte, W. Guenther, M. Allen, A. Blazevic, J. Fuchs, J. C. Gauthier, M. Geissel, P. Audebert, T. Cowan and M. Roth, "MeV Ion Jets from Short-Pulse-Laser Interaction with Thin Foils," Phys. Rev. Lett., vol. 89, p. 085002, 2002.
14) J. Badziak, E. Woryna, P. Parys, K. Yu. Platonov, S. Jablonski, L. Ryc, A. B. Vankov and J. Wotowski, " Fast Proton Generation from Ultrashort Laser Pulse Interaction with Double-Layer Foil Targets", Phys. Rev. Lett., vol. 87, p. 215001, 2001.
15) E. Fourkal, I. Velchev and C.-M. Ma, "Coulomb explosion effect and the maximum energy of protons accelerated by high-power lasers," Phys. Rev. E, vol. 71, p. 036412, 2005.
16) T. E. Cowan, J. Fuchs, H. Ruhl, A. Kemp, P. Audebert, M. Roth, R. Stephens, I. Barton, A. Blazevic, E. Brambrink, J. Cobble, J. Fernandez, J.-C. Gauthier, M. Geissel, M. Hegelich, J. Kaae, S. Karsch, G. P. Le Sage, S. Letzring, M. Manclossi, S. Meyroneinc, A. Newkirk, H. Pepin and N. Renard-LeGalloudec, "Ultralow Emittance, Multi-MeV Proton Beams from a Laser Virtual-Cathode Plasma Accelerator," Phys. Rev. Lett., vol. 92, p. 204801, 2004.
17) K. Matsukado, T. Esirkepov, K. Kinoshita, H. Daido, T. Utsumi, Z. Li, A. Fukumi, Y. Hayashi, S. Orimo, M. Nishiuchi, S. V. Bulanov, T. Tajima, A. Noda, Y. Iwashita, T. Takeuchi, S.

Nakamura, A. Yamazaki, M. Ikegami, T. Mihara, A. Morita, M. Uesaka, K. Yoshii, T. Watanabe, T. Hosokai, A. Zhidkov, A. Ogata, Y. Wada and T. Kubota, "Energetic Protons from a Few-Micron Metallic Foil Evaporated by an Intense Laser Pulse," Phys. Rev. Lett., vol. 91, p. 215001, 2003.

18) E. L. Clark, K. Krushelnick, M. Zepf, F. N. Beg, M. Tatarakis, A. Machacek, M. I. K. Santala, I. Watts, P. A. Norreys and A. E. Dangor, "Energetic Heavy-Ion and Proton Generation from Ultraintense Laser-Plasma Interactions with Solids," Phys. Rev. Lett., vol. 85, p. 1654, 2000.

19) T. Nakamura and S. Kawata, "Origin of protons accelerated by an intense laser and the dependence of their energy on the plasma density," Phys. Rev. E, vol. 67, p. 026403, 2003.

20) S. V. Bulanov, T. Zh. Esirkepov, V. S. Khoroshkov, A. V. Kuznetsov and F. Pegoraro, "Oncological hadrontherapy with laser ion accelerators," Phys. Lett. A, vol. 299, pp. 240-247, 2002.

21) S. V. Bulanov, T. Zh. Esirkepov, J. Koga, T. Tajima and D. Farina, "Concerning the maximum energy of ions accelerated at the front of a relativistic electron cloud expanding into vacuum," Plasma Phys. Rep., vol. 30, pp. 18-29, 2004.

22) M. Borghesi, A. J. Mackinnon, D. H. Campbell, D. G. Hicks, S. Kar, P. K. Patel, D. Price, L. Romagnani, A. Schiavi and O. Willi, "Multi-MeV Proton Source Investigations in Ultraintense Laser-Foil Interactions," Phys. Rev. Lett., vol. 92, p. 055003, 2004.

23) F. Lindau, O. Lundh, A. Persson, P. McKenna, K. Osvay, D. Batani and C.-G. Wahlström, "Laser-Accelerated Protons with Energy-Dependent Beam Direction," Phys. Rev. Lett., vol. 95, p. 175002, 2005.

24) T. Zh. Esirkepov, S. V. Bulanov, K. Nishihara, T. Tajima, F. Pegoraro, V. S. Khoroshkov, K. Mima, H. Daido, Y. Kato, Y. Kitagawa, K. Nagai and S. Sakabe, "Proposed Double-Layer Target for the Generation of High-Quality Laser-Accelerated Ion Beams," Phys. Rev. Lett, vol. 89, p. 175003, 2002.

25) T. Esirkepov, M. Borghesi, S. V. Bulanov, G. Mourou and T. Tajima, "Highly Efficient Relativistic-Ion Generation in the Laser-Piston Regime," Phy. Rev. Lett., vol. 92, p.175003, 2004.

26) A. P. L Robinson, A. R. Bell and R. J. Kingham, "Effect of Target Composition on Proton Energy Spectra in Ultraintense Laser-Solid Interactions," Phys. Rev. Lett., vol. 96, p. 035005, 2006.

27) R. Sonobe, S. Kawata, S. Miyazaki, M. Nakamura and T. Kikuchi, "Suppression of transverse proton beam divergence by controlled electron cloud in laser-plasma interactions," Phys. Plasmas, vol. 12, p. 073104, 2005.

28) S. Miyazaki, S. Kawata, R. Sonobe and T. Kikuchi, "High-energy proton generation and suppression of transverse proton divergence by localized electrons in a laser-foil interaction," Phys. Rev. E, vol. 71, p. 056403, 2005.

29) T. Nishikawa, H. Nakano, K. Oguri, N. Uesugi, K. Nishio, and H. Masuda, "Nanohole-array size dependence of soft x-ray generation enhancement from femtosecond-laser-produced plasma", J. Appl. Phys., vol. 96, pp.7537-7543, 2004.

30) J. Psikal, V. T. Yikhonchuk, J. Limpouch, A. A. Andreev, and A.V. Brantov, Phys. Plasmas, "Ion acceleration by femtosecond laser pulses in small multispecies targets", vol.15, pp.053102-1-8, 2008.

31) M. Schollmeier, K. Harres, F. Nurnberg, A. Blazevic, P. Audebert, E. Brambrink, J. C. Fernandez, K. A. Flippo, D. C. Gautier, M. Geibel, B. M. Hegelich, J. Schreiber, and M. Roth, "Laser beam-profile impression and target thickness impact on laser-accelerated protons" Phys. Plasmas, vol. 15, pp. 0531011-12, 2008.

32) H. A. Sumeruk, S. Kneip, D. R. Symes, I. V. Churina, A. V. Belolipetski, G. Dyer, J. Landry, G. Bansal, and A. Bernstein, "Hot electron and x-ray production from intense laser irradiation of wavelength-scale polystyrene spheres" Phys. Plasmas, vol. 14, pp. 062704-1-9, 2007.

33) W.M. Wang, Z. M. Sheng, and J. Zhang, "A model for the efficient coupling between intense lasers and subwavelength grating targets" Phys. Plasmas, vol. 15, pp. 030702-1-4, 2008.

GENERATION OF INTENSE PULSED ION BEAM AND ITS APPLICATION TO MATERIALS PROCESSING

Y. Ochiai, K. Fujikawa, H. Ito and K. Masugata

Dep. of Electrical and Electronic Engineering, University of Toyama,
3190 Gofuku, Toyama 930-8555, Japan

Abstract

Intense pulsed heavy ion beam is expected to be applied to materials processing including surface modification and the ion implantation. For those applications, it is very important to generate high-purity ion beams with various ion species. A magnetically insulated ion diode with an active ion source of a vacuum arc plasma gun has been developed in order to generate pulsed metallic ion beams. When the ion diode was operated at diode voltage $\approx$ 200 kV, diode current $\approx$ 15 kA and pulse duration $\approx$ 100 ns, the ion beam with an ion current density of $>$ 200 A/cm^2 was obtained at 50 mm downstream from the anode. From Thomson parabola spectrometer measurement, the ion beam consists of aluminum ions (Al$^+$, Al^{2+} and Al^{3+}) of energy 140-780 keV and the proton impurities of energy 170-190 keV. To evaluate the irradiation effect of the ion beam, an amorphous silicon thin film of thickness $\approx$ 1μm was used as the target, which was deposited on the glass substrate. By the X-ray diffraction measurement of the films before and after the irradiation, the film was found to be poly-crystallized after 5-shots of the pulsed aluminum ion beam irradiation.

1 Introduction

Over the last three decades, there has been remarkable progress in the understanding and development of intense pulsed ion beam (IPIB) technology [1]. The primary application driving the development of this technology is inertial confinement fusion energy research [2,3]. Recently, however, these ion beams with ion energies from 50 keV to 10 MeV, ion currents from 1 kA to 10 MA, and pulse durations from 10 to 1000 ns are finding new applications in diverse fields such as materials processing [4,5]. Because of the short range of the ions in matter, its application usually involves the surface modification of materials, e.g., implantation [6], alloy mixing [7,8], defect formation [9,10] and thin film deposition [11,12]. For many of these applications, these beams are used primarily as heat sources to ablate or rapidly melt solid targets. Especially for the ion implantation process to semiconductor materials, the ion implantation and the surface annealing can be completed simultaneously, since the use of IPIB enables the accumulation of energy in very short time into the near surface region while it maintains a low substrate temperature. Therefore, IPIBs have received extensive attention as a tool for a new ion implantation technology named "pulsed ion beam implantation".

For the application of IPIBs to the semiconductor implantation, it is very important to develop the IPIB technology of generating high-purity ion beams from various species, such as nitrogen, phosphorous, boron and aluminum being useful donor and acceptor in silicon carbide (SiC). For the production of gaseous ion beams, we have developed a new type of the MID with an ion source of a gas

puff plasma gun and were successful in generating the high-purity pulsed nitrogen ion beam with an ion current density of 54 A/cm^2 and a pulse duration of 90 ns at 50 mm downstream from the anode [13].

There has been much progress in various, both scientific and technical, applications of methods of material surface modification by pulsed metallic ion beams, however, pulsed metallic ion beam production remains difficult and cannot be obtained yet. Several different methods for metal ion generation are known, such as by the use of liquid metal ion source, sputtering type ion sources, and sources using vacuum arcs and lasers. The metal vapor vacuum arc ion source [14] is the most suitable for the source of the intense pulsed metallic ion beam generation. In this kind of ion source the metal plasma can be produced from over 50 of the solid metals of the periodic table, since the vacuum arc provides both evaporation and ionization of the cathode material. The vacuum arc ion source has been used for ion implantation to modify the surface properties of materials. The ion beam current, however, is not high enough for the required ion dose and the high speed heat treatment by the irradiation of the ion beam. In order to achieve the rapid-heat treatment and the ion implantation simultaneously, we have developed a novel IPIB technology of generating intense pulsed metallic ion beams, i.e., magnetically insulated ion diode using vacuum arc plasma gun. In addition, the beam was used to irradiate amorphous silicon thin films to evaluate the iraddiation effects of IPIB. In this article, we present the experimental results about characteristics of the intense pulsed metallic ion beam including ion species, energy spectrum, reproducibility of ion beam and spatial distribution of ion current density.

2   Experimental Setup

Figure 1 shows a schematic configuration of ion diode system for intense pulsed ion beam. The system consists of a Marx generator with the stored energy of 240 J, an ion source, a magnet-

ically insulated ion acceleration gap (diode), and a stainless-steel vacuum chamber with a diffusion pump package. The Marx generator is comprised of four-stage incorporating capacitors charged up to 50 kV, charging resistors for the capacitors and SF$_6$-filled field-distortion gap switches. The output parameters of the Marx generator are voltage of 200 kV, current of 15 kA and pulse duration of 100 ns [full width at half maximum (FWHM)]. In order to produce the pulsed metallic ion beam, the vacuum arc plasma gun is used as the ion source and installed inside the anode. In the experiment the vacuum chamber is evacuated to 5 × 10^{-3} Pa.
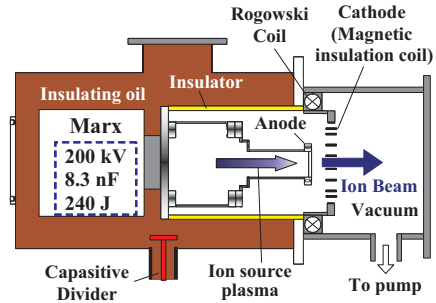
Fig.1 Schematic drawing of ion diode system used in the present studies.

The diode voltage (V_d) and diode current (I_d) are measured by the capacitive voltage divider and Rogowski coil, respectively. The values of diode voltage and diode current are calculated by the ratio factor of the voltage divider (20000) and the coefficient of the Rogowski coil (27 kA/V). A biased ion collector (BIC) is used for the measurement of the ion current density of the IPIB. The collector of BIC was biased at a voltage of -200 V to remove accompanying electrons.

The detail components of the ion diode is illustrated in Fig. 2. The ion diode consists of a cylindrical anode of 115 mm length by 60 mm diameter and a cathode of grid structure. Anode-to-cathode gap spacing for the beam is adjusted to 10 mm. The top of the anode is a stainless-steel plate of 60 mm diameter, in which a hole of 30 mm diameter is drilled at the central area of the anode in order to allow the source plasma to be injected into the anode-cathode gap. The cathode
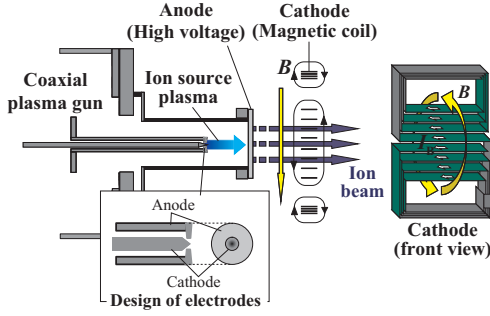
Fig.2 Schematic configuration of magnetically insulated ion diode with vacuum arc plasma gun. The inset shows the electrode design of vacuum arc plasma gun.

has a grid structure for the ion beam extraction with a total cathode transparency of about 90 %. In order to generate a transverse magnetic field in the anode-cathode gap to suppress the electron flow, the cathode also acts as a multi-turn magnetic field coil. Thus, as shown in Fig. 2, the cathode (coil) has a shape like 8-character, one end of which is connected to the vacuum chamber, and is made of phosphor bronze strip of 10 mm width and 1 mm thickness. A capacitor bank with capacitance of 250 μF and charging voltage of 3 kV is used to apply a pulse current to the coil. Just before application of the accelerating voltage, the uniform magnetic field of 0.7 T in the acceleration gap is produced by a pulse current up to 10 kA with rise time of 50 μs passing in the cathode loop. At peak of the magnetic field, a positive voltage supplied from Marx generator is applied to the anode. Electrons are prevented from crossing the anode-cathode gap by the applied magnetic field, but the more massive ions, only very weakly deflected by the magnetic field, have approximately linear trajectories.

A vacuum arc plasma gun is used as the source of the pulsed metallic ion beam. As shown in the inset of Fig. 2, the plasma gun has a pair of coaxial aluminum electrodes, i.e., an inner electrode of 200 mm length by 6 mm outer diameter and an outer electrode of 10 mm inner diameter. The inner electrode is placed to reduce the gap length to 1 mm on the top of the outer electrode. In the vacuum arc plasma gun the dense metal-

lic plasma is produced by an ionization of cathode materials evaporated from cathodic spots of the vacuum arc discharge. The ion species is determined by the material of the electrode. The plasma gun power supply is a 3.3 μF capacitor bank charged to 30 kV. The capacitor bank is connected anode to cathode and is triggered by applying 15 kV spark between the cathode and the trigger electrode of the field-distortion switch. The pulse current produced by the capacitor bank is fed through inductively isolated coaxial cables, since the vacuum arc plasma gun is placed inside the anode where the high-voltage pulse is applied.

The ion current density of the source plasma produced by the plasma gun was evaluated by a BIC placed on the central axis at 50 mm downstream from the top of the plasma gun where the anode is placed in the acceleration experiment. Figure 3 shows the typical waveforms of the discharge current (I_p) and the ion current density (J_i), where the capacitor banks for the plasma gun was charged up to 30 kV. As seen in Fig. 3, the discharge current I_p has a sinusoidal waveform of peak current 12 kA and quarter cycle 6 μs. The ion beam with a peak current density 158 A/cm^2 and a pulse duration of 2.5 μs is observed at about 7.5 μs after the rise of I_p. This result suggests that it takes 7.5 μs for the ion beam produced in the plasma gun to reach the acceleration gap. Assuming that the plasma is produced at the rise of I_p, the delay time between Ip and Ji gives the drift velocity of 6.7×10^3 m/s, which corresponds to the ion energy of 6 eV.
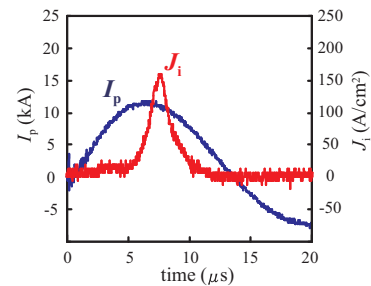
Fig.3 Typical waveforms of discharge current I_p and ion current density J_i of vacuum arc plasma gun.

3 Experimental Results

Figure 4 shows the typical waveforms of the diode voltage (V_d), the diode current (I_d) and the ion current density of the accelerated ion beam (J_i). Here, the Marx generator was charged up to 50 kV and fired at a delay time of 7.5 μs after the rise of the discharge current of the plasma gun. The ion-beam current density J_i is measured by the BIC placed at 50 mm downstream from the surface of the anode on the axis. As seen in the Fig. 4(a), V_d rises in 50 ns and has a peak of 220 kV, whereas I_d rises with V_d and has a peak of 12 kA at $t = 75$ ns. It can be clearly seen from Fig. 4(b) that the ion beam of the ion current density 230 A/cm^2 and pulse duration 40 ns (FWHM) is obtained at 45 ns after the peak of V_d.
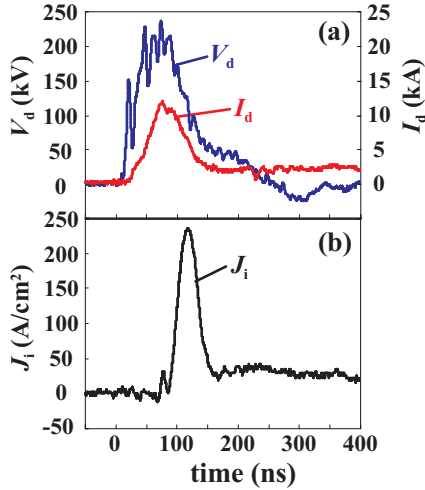
Fig.4 Typical waveforms of (a) diode voltage V_d, diode current I_d and (b) ion-beam current density J_i.

In order to evaluate the ion species and the energy spectrum of the ion beam, the Thomson parabola spectrometer (TPS) was used. Figure 5 shows the schematics of TPS. The TPS is constructed of a 1st pinhole, a 2nd pinhole, a magnetic deflector, an electric deflector and an ion detecting plate of CR-39. A small portion of the ion beam is collimated by a pair of pinholes with diameter of 0.3 mm. The collimated beam is passed through deflection plates having parallel magnetic field of 0.8 T and the electric field of 0.6 MV/m transverse to the beam direction.

Hence, ions are deflected by the electric field and the magnetic field, respectively and the deflected beam components trace out parabolas in the plane perpendicular to their paths. The parabola is dependent on each value of charge-to-mass ratio included in the beam. The particle positions are recorded on CR-39 plastic, which is etched in a NaOH bath to make the tracks visible. The ion species is identified by comparing these measurements with knowledge of the atomic composition in the source plasma. The energy spectra are determined from the relative number of tracks at different positions along either the magnetic or the electric field axes. The detector is located at 50 mm from the anode to avoid detector saturation and pinhole closure due to plasma formation. The spot formed by undeflected charge exchange neutral beams is useful for orientation of the CR-39 films during scanning.
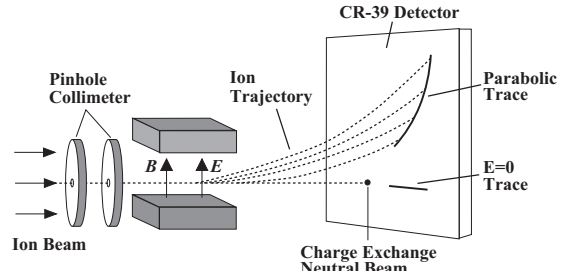
Fig.5 Schematic of Thomson parabola spectrometer.

Figure 6 shows an example of the track pattern recorded on the CR-39 detecting plate along with the calculated trajectories of various ion species. Here, E and Z in Fig. 6 are the ion energy in keV and charge state of ions, respectively. The tracks show that proton and singly, doubly and triply ionized aluminum are present. We can evaluate the ion number ratio on each ion species by counting the track number, since each ion track on CR-39 is formed by an irradiation of single ion. Table I summarizes the energy range and the number ratio of each ion species evaluated from the track pattern. As shown in the table, the energies of singly, doubly and triply ionized aluminum ions were found to be 140-290 keV, 220-580 keV and 290-780 keV, respectively. The maximum energy
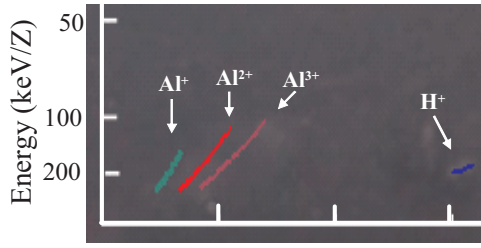
Fig.6 Example of ion track pattern on CR-39 film measured by the Thomson parabola spectrometer. The lines represent calculated track trajectories for the indicated ion species.

of Al^{3+} ions coincides with about triple the peak of the diode voltage as expected for the triply charged component. On the other hand, the high-energy end of the traces of singly ionized nitrogen ions is around 290 keV/Z, which is larger than the peak value of the diode voltage ($V_d \approx 220$ kV). These high-energy Al^+ ions are considered to be produced by the charge exchange of doubly and triply ionized aluminum ions. As seen in Fig. 6, the aluminum ions spectrum consisting of singly, doubly and triply ionized aluminum ions has a broad peak centered from 120 to 250 keV/Z. Hence, we see that the aluminum ions are originally accelerated at the ionization state of Al^+, Al^{2+} and Al^{3+} and charge-exchanged in the drift region. The energy of hydrogen ions was found to be 170-190 keV in Table 1, which was in good agreement with the diode voltage measured with the voltage divider. The proton seems to originate from absorbed matter on the surface of anode and cathode and on the electrode of the plasma gun.

Table.1 Energy and number ratio of each ion species evaluated by TPS.

Ion species	Energy (keV)
Al^+	140-290
Al^{2+}	220-580
Al^{3+}	290-780
H^+	170-190

Figure 7(a) shows the dependence of the ion beam current density of the ion diode (J_i) on the shot number. The experimental parameters are the same as those mentioned previously in this paper. As seen in Fig. 7(a), the accelerated ion-beam current density J_i is poorly reproducible and ranges from 0 to 260 A/cm^2. The average value of J_i in 60 shots is calculated to be 108 A/cm^2. In order to find out the reason of the shot-to-shot fluctuation of J_i, the reproducibility of the ion current density of the vacuum arc plasma gun (J_{si}) was evaluated. The experimental results are displayed in Fig. 7(b). It is clearly seen from Fig. 7(b) that there is a lot of scatter in the ion current density of the plasma gun and the reproducibility of J_{si} is very poor. The ion current density J_{si} ranges from 20 to 300 A/cm^2 and the average value of J_{si} in 40 shot is calculated to be 174 A/cm^2. It is thought that the poor reproducibility of the accelerated ion-beam current density is caused by the shot-to-shot fluctuation of the plasma source produced in the plasma gun.
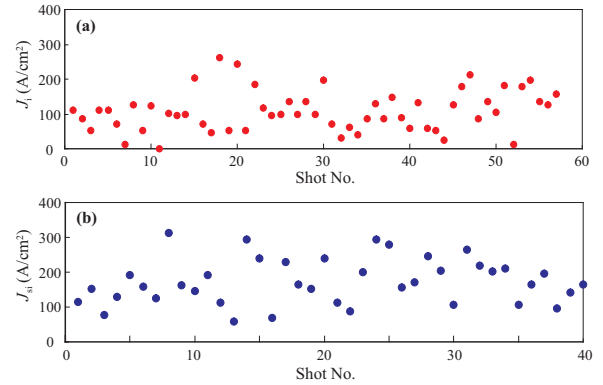
Fig.7 Dependence of (a) accelerated ion-beam current density J_i and (b) ion current density of source plasma J_{si} on shot number.

The above experimental results show that the pulsed aluminum ion beam fills the requirement, i.e., high ion current density and short pulse duration, that the rapid-heat treatment and the ion implantation can be carried out simultaneously. As seen in Fig. 7, however, the obtained ion beam has the poor shot-to-shot reproducibility and the nonuniform spatial distribution. The precise parameters are important for materials processing in industrial application. To realize good reproducibility of the diode's operation, we are planning to evaluate the plasma source produced

in vacuum arc plasma gun in detail and modify the shot-to-shot reproducibility by optimizing the electrode structure of the plasma gun, since the poor reproducibility of the ion current density is caused by the shot-to-shot fluctuation of the plasma gun. In addition, there seems to be some room for making improvements in the beam purity to apply the pulsed heavy ion beam to the ion implantation for semiconductor materials. In order to improve the purity of IPIB, we are developing a new type of pulsed ion beam accelerator named bipolar pulse accelerator [15].

To evaluate the annealing effect of the pulsed ion beam to the materials, amorphous silicon thin films was used as targets. The films have a thickness of 1 μm and fabricated on the glass substrate. The target was placed at 50 mm downstream from the anode. Figure 8 shows the X-ray diffraction pattern of the target before and after five shots of irradiation. As seen in Fig. 8, no diffraction peak is observed in the target before the irradiation. In contrast three peaks of Si(111), Si(220) and Si(311) were observed on the target after the irradiation. The results clearly indicate that the amorphous silicon thin film was poly-crystallized by the irradiation of the pulsed ion beam.
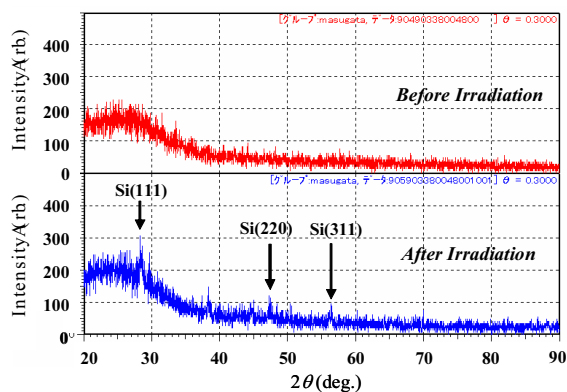
Fig.8 X-ray diffraction pattern of the amorphous silicon thin films before and after the ion beam irradiation.

4 Summary

We have developed the magnetically insulated ion diode with an ion source of a vacuum arc plasma gun in order to generate the pulsed metallic ion beam. When the ion diode was operated at a diode voltage of about 220 kV, a diode current of about 12 kA and a pulse duration of 100 ns (FWHM), the aluminum ion beam with an ion current density of about 230 A/cm^2 and a pulse duration of 40 ns was obtained at 50 mm downstream from the anode. The energy and ion species of the ion beam were evaluated by the Thomson parabola spectrometer and we found that the ion beam consisted of Al$^+$, Al^{2+} and Al^{3+} ions with energy of 140-780 keV and impurity of proton with energy of 170-190 keV. To evaluate the irradiation effect of the ion beam to solid material, amorphous silicon thin film of thickness 1 μm was used as the target, which was deposited on the glass substrate. We found that the film was poly-crystallized after five shots of irradiation.

In the application of IPIBs to materials processing, not only the element effects of foreign species, but also the heating effects of ion beam irradiated on the surface of the target are very important and available. The new type of the MID with two types of plasma gun as the ion source, i.e., a gas puff plasma gun and a vacuum arc plasma gun, enables us to produce the high-purity IPIB with various ion species. Therefore, the application of IPIB technology can simultaneously achieve the advantages of rapid-heat treatment and ion implantation.

References

[1] V. M. Bystritskii and A. N. Didenko, *High-Power Ion Beams.* American Institute of Physics, New York, (1989).

[2] S. Humphries, Jr, Nucl. Fusion, **20**, pp.1549-1612, (1980).

[3] J. P. VanDevender and D.L. Cook, Science, **232**, pp.831-836, (1986).

[4] K. Yatsui *et al.*, Phys. Plasma, **1**, pp.1730-1737, (1994).

[5] D. J. Rej *et al.*, J. Vac. Sci. Technol. **15**, pp.1089-1097, (1997).

[6] W. Chu, S. Mader, E. Gorey, J. Baglin, R. Hodgson, J. Neri, and D. A. Hammer, Nucl. Instrum. Methods, **194**, pp.443-447, (1982).

[7] R. Fastow and J. W. Mayer, J. Appl. Phys., **61**, pp.175-181, (1987).

[8] Y. Nakagawa *et al.*, Nucl. Instrum. Method B, **39**, pp.603-606, (1989).

[9] A. D. Progrebnyak, Yu. P. Sharkeev, N. A. Makhmudov, G. V. Pushkareva, and Sh. A. Tukhtaev, Phys. Status Solidi A, **123**, pp.119-130, (1991).

[10] A.N. Didenko *et al.*, Mater. Sci. Eng. A, **115**, pp.337-341, (1989).

[11] Y. Shimotori, M. Yokoyama, H. Isobe, S. Harada, K. Masugata, and K. Yatsui, J. Appl. Phys., **63**, pp.968-970, (1988).

[12] G. P. Johnston *et al.*, J. Appl. Phys., **76**, pp.5949-5954, (1994).

[13] H. Ito, H. Miyake and K. Masugata, Rev. Sci. Instrum., **79**, pp.103502-1 - 103502-5, (2008).

[14] I. Brown, Rev. Sci. Instrum. **65**, 3061-3081 (1994).

[15] H. Ito, K. Igawa, I. Kitamura and K. Masugata, Rev. Sci. Instrum., **78**, pp.013502-1 - 013502-5, (2007).

FABRICATION OF DLC FILM BY PULSED ION-BEAM ABLATON IN A PLASMA FOCUS DEVICE

Z.P. Wang*, H.R. Yousefi, Y. Nishino, D.X. Cheng, M. Gemmei, H. Ito, K. Masugata

Department of Electric and Electronic system Engineering, University of Toyama, 3190 Gofuku, Toyama 930-8555, Japan

ABSTRACT

The pulsed intense ion beam (proton beam), which is emitted from a plasma focus (PF) discharges perform with hydrogen gas, have been used to ablate the graphite target depositing diamond-like carbon (DLC) films on Si substrates. The substrates were mounted on a holder, which allowed for deposition at positions between normal and 20° off-normal to the target. The samples were removed for analysis after 10 and 20 shots. Nano-particles were observed in the films by field-emission scanning electron microscopy (FE-SEM). Raman spectra indicate that sample of 20° off-normal possesses the highest sp^3 content among these three samples. Highest hardness of this position was later found by nano-indentor.

I. Introduction:

The dense plasma focus (DPF) is well known as a compact and an efficient pulsed source of x-rays [1], neutrons [2, 3], relativistic electrons and energetic ion beams [4, 5]. The current sheath dynamics in Plasma Focus (PF) allows the formation of high temperature $(1-2\ keV)$ and high-density $(\sim10^{25}-10^{26}\ m^{-3})$ plasma column at the end of radial collapse phase [6]. The plasma column then disintegrated due to plasma instabilities, which generate energetic ions and relativistic electrons. The plasma jet and energetic electrons are responsible for the ablation of the anode material and the ablated material is deposited on the substrate [7]. The DPF device has been experimentally proved to be able to emit ions of characteristic energy from hundreds of kev to tens of Mev [8, 9].

The first DLCs were prepared as thin films by Aisenberg and Chabot using ion beam deposition [10]. So far several techniques have been developed to grow these films, including chemical-vapor deposition (CVD) and physical-vapor deposition (PVD). Polycrystalline diamond films have been deposited using a variety of CVD methods at high temperatures [11]. These methods have achieved high-quality diamond films at deposition rates of up to 1 mm/h on small-area $(-cm^2)$ substrates. Rates drop to below 1 μ m/h for larger area substrates (>100 cm^2). CVD methods can create amorphous carbon (DLC) films, if low substrate temperatures (<400℃) are employed [12, 13].

The wide spread use of DLC has been limited

by poor adhesion of these films to substrates, because of large compressive stresses induced in the films during the deposition process [14]. The DPF is a promising source in this respect offering room temperature deposition of thin films having better adhesion to the substrate owing to the broad energy spectrum of its ion streams [15]. Moreover, as a source of pulse energy beams, the DPF device shares some common characteristics with respect to pulsed laser deposition (PLD), including high deposition rate, possible film deposition under a reactive background gas pressure [16], direct ion irradiation process [7], deposition of materials having high melting temperature as compared to the continuous deposition techniques [17]. Besides, there is also big potential for DPF device to achieve larger deposition area than PLD.

C.R. Kant et al. reported crystalline graphite thin films deposition on silicon and quartz substrates using argon ions of DPF [17]. Deposition of DLC films on silicon substrates by ablation of graphite anode material with the help

S. Zeb et al [18]. This paper reports the deposition and characterization of DLC films on Si (100) substrates using the pulsed proton beam emitted from DPF device. Crystal structural, bonding structural, morphological and mechanical properties of deposited films are studied.

II. Experimental Procedure

The pulsed ion beam, are produced by a 20kJ Mather-type DPF device, has been used in the present experiment. The arrangement of the experiment set-up is shown in **Fig.1**. The plasma focus (PF) device consists of an inner electrode (anode) and an outer electrode (cathode). The anode is made of copper with diameter and length of 50mm and 243mm, respectively. The top of the anode is made into hollow geometry. The detailed parameter of the shape of the anode is shown in **Fig2. (a)**. It is necessary to mention that the anode material will be ablated by the electrons that emitted from the pinch [19]. As a consequence, this impurity will be deposited on the substrates. In this experiment, the hollow in the anode is made as bigger and deeper as possible to reduce

Fig. 1. The schematic of the dense plasma focus device employed for DLC film deposition

of pulsed electron beam in a 1.45 kJ DPF device under nitrogen environment has been reported by

(a)   (b)
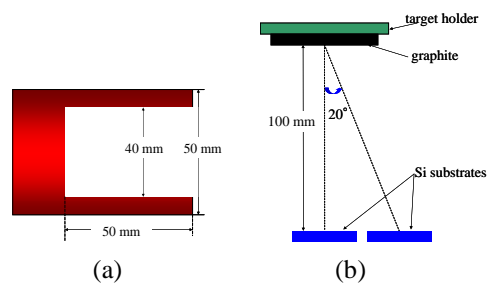
Fig. 2 (a). Feature geometry of anode.

Fig. 2(b). Feature geometry between target and substrates.

As a target, high purity graphite disc of 50 mm diameter and 5 mm thickness, was placed into the chamber at 150 mm from anode tip along

axial direction. The carbon films were deposited on commercially available one sided polished Si (1 0 0) wafer, which was cut into square shape biscuits of 15 mm × 15 mm and then was cleaned ultrasonically in acetone. The substrates were blown-dry and then set into the chamber with the help of a sample holder, bearing two samples at angular position of normal and 20° off normal to the target. Detailed parameter is shown in **Fig. 2 (b).** Generally after each fresh loading of samples for thin-film deposition, it takes some DPF shots to condition the plasma focus device for optimized efficiency. In order to prevent the samples from being exposed to weak focusing, a shutter is used before proper focusing was obtained [7].

For films deposition, the chamber was first evacuated up to 4×10^{-5} mbar and H_2 was introduced as working gas at the optimum pressure of 3mbar. The work of optimization of the PF device at various working gas pressure has been done by monitoring the rogowski coil current and ion current density. When the pulse trigger is switched on, the discharge starts over the insulator surface and then the plasma sheath comes off and is accelerated axially by the magnetic field auto-generated by the current (Lorentz force). After the current sheath runs over the upper end of the central electrode (anode), the plasma is compressed in a small region (the focus or pinch). According to the plasma instabilities, the pinch column collapsed and beams of ions (proton in our case) and electrons were generated [5].

After PF system reached the optimum condition, 10 and 20 fires were chosen for DLC

formation. In this experiment, energetic pulsed ions emitted from plasma focus were used to ablate the graphite target and forming the carbon ablation plasma. The ionic, atomic, and molecular carbon species in the ablation plasma offered good carbon ion source for DLC formation. The as-deposited samples were later investigated by X-ray diffractometer (XRD, XRD-6000, Shimadzu), Field-Emission Scanning Electron Microscopy (SEM, JSM-6700F JEOL), Raman spectroscopy (NRS-1000, Japan Spectroscopic Co., Tokyo, Japan) and Nano-indentor (Fisher scope, H100C).
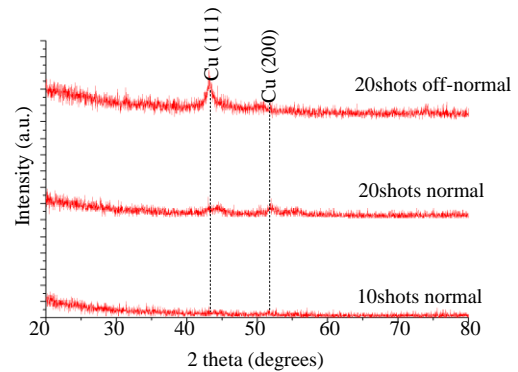
Fig. 3. XRD patterns of samples deposited at: 10 shots normal, 20 shots normal and 20 shots off-normal.

III. Results and Discussion

1. XRD results

Samples treated at normal position for 10 and 20 shots along with sample at 20° off-normal were chosen for characterization. XRD spectra were taken over the range of $2\theta = 20{-}80°$ at a scan rate of 0.2°/min. **Fig. 3** shows the XRD patterns of as-deposited samples under different conditions of 10 shots normal, 20 shots normal

| | 10 shots normal | 20 shots normal | 20 shots off-normal |
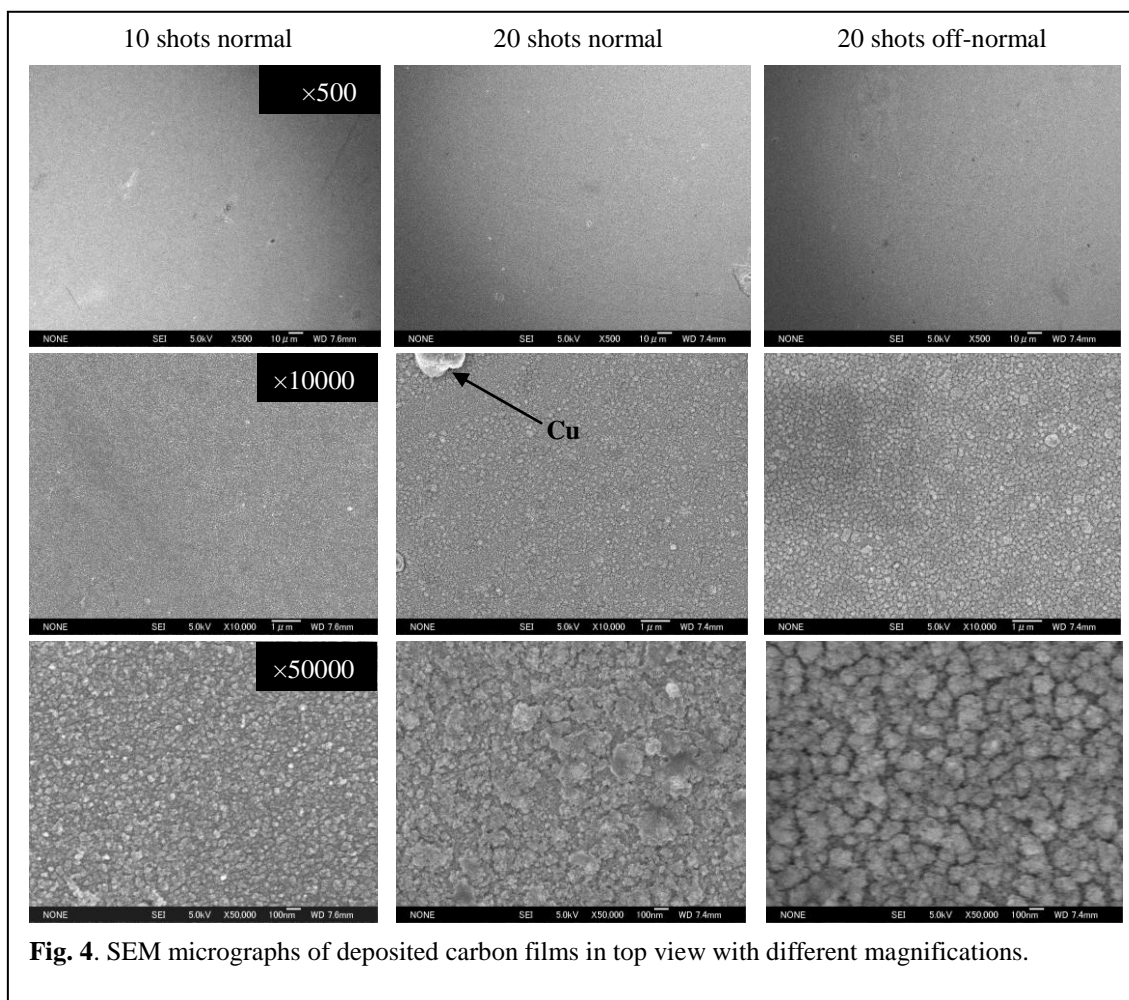
Fig. 4. SEM micrographs of deposited carbon films in top view with different magnifications.

and 20 shots off-normal. The diffraction peaks which observed at $2\theta = 43.3°$ and $50.4°$, corresponding to (111) and (200), of copper. The presence of these copper peaks indicates that copper impurity was found in the samples. Actually, it is well known that energetic electrons are generated in a PF and irradiate the anode [20]. The irradiation of the electrons will heat the anode and release absorbed molecules on the anode or evaporate the metallic ions. Hence, the irradiation seems to be the cause of the production of impurities. These impurities were also observed in the previous experiment did by K. Takao et al with nitrogen filling gas [21]. Besides, no obvious carbon peak was found in the samples, which indicates that the amorphous carbon films were achieved.

2. SEM results

Surface morphology of deposited films at the positions of 10 shots normal, 20 shots normal and 20 shots off-normal with different magnification were provided in **Fig. 4**. The fist line of SEM micrographs displayed the overall surface situation under the magnification of 500, which indicates that reasonably smooth surface without cracks or pits were obtained in the deposited samples. The middle line of SEM micrographs showed more featured surface morphology under the magnification of 10000. Some micro-sized

spots popped up on the surface of the deposited samples, which is speculated to be Cu micro-particles after ion irradiation. Such kind of situation was also reported by M.V. Roshan et al while irradiating aluminum by PF device [19]. This observation perfectly matches with the previous conclusion gained from XRD results. Granular surfaces were observed in the last line of SEM micrographs. These nano-sized agglomerates of deposited films at the position of 10 shots normal and 20 shots off-normal exhibit homogeneous distribution of grains. On the other hand, the surface of deposited film at the position of 20 shots normal doesn't perform the same homogeneousness as the other two samples although the grain is growing bigger as compared with the sample of 10 shots normal. It is inferred that the emergence such unhomogeneity in the sample of 20 shots normal owing to melting, which may due to the overheating process of energetic carbon ions with maximum ion energy flux in the carbon ablation plasma. Mean grain size observed from the SEM images, for DLC layers formed at 10 shots normal, 20 shots normal and 20 shots off-normal were found to be of the order of 30 nm, 60 nm and 90 nm, respectively.

3. Raman results

Raman spectroscopy was performed, because it is sensitive to the diamond-like bonding character in the films. Raman spectra of deposited films under different conditions are shown in **Fig. 5**. The spectra have been displaced vertically for clarity. The spectra consist of two broad peaks present at about 1580 cm^{-1}, corresponding to G band and at 1332 cm^{-1} corresponding to D-band

[10]. G peak position (Raman shift) and band intensity ratio (I_D/I_G) are used for explanation, which are plotted in **Fig. 6**. Obviously, sample of 20 shots off-normal owns the lowest G peak position and intensity ratio. Although Raman spectra do not quantitatively indicate the ratio of sp^2 to sp^3-bonded carbon in DLC, it has been suggested that the sp^2-bonded carbon fraction increases as the Raman shift of the DLC band
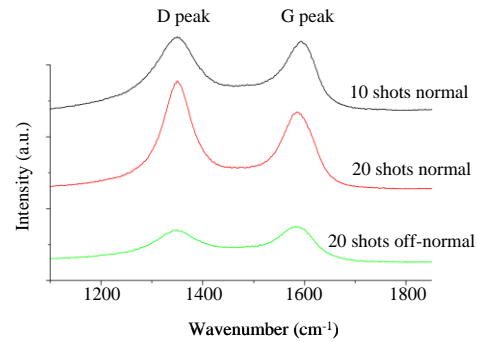
Fig. 5. Raman spectra of films deposited at: 10 shots normal, 20 shots normal and 20 shots off-normal.
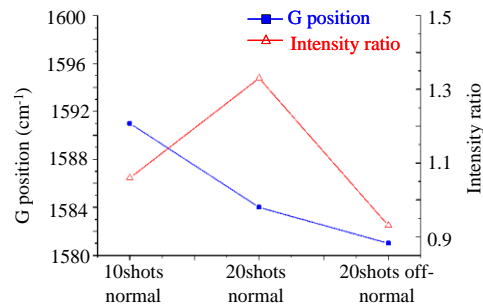
Fig. 6. Profile of G peak position and band intensity ratio.

increases [22]. Besides, decrease of band intensity ratio (I_D/I_G) is indicative of a relative increase in the diamond (sp^3) content, since the band intensity ratio (I_D/I_G) is inversely proportional to

sp^3/sp^2 ratio of carbon bonding [18]. Consequently, the sample of 20 shots off-normal is extrapolated to possess higher mechanical hardness than the other two samples, because of the higher sp^3 content. There is no evidence of crystalline diamond, which displays a narrow Raman band at around 1330 cm-1, present in any of the spectra.
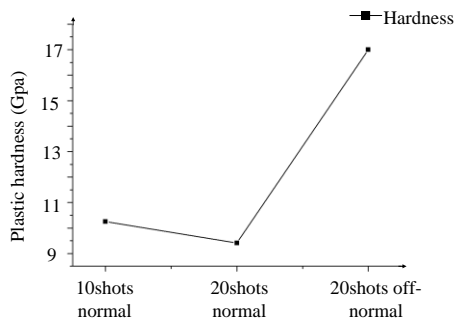
Fig. 7. Variation of plastic hardness for samples deposited at: 10 shots normal, 20 shots normal and 20 shots off-normal.

4. Hardness results

Studies of film plastic hardness with a Nano-indentor found that sample of 20 shots off-normal possesses the highest hardness among the three samples shown in **Fig. 7**. This result has been speculated previously by Raman data. Meanwhile, these results are in good agreement with the Hall-Petch behavior (with grain size below 100 nm) [23], which gives out that the hard materials always decrease in strength of crystalline with reduced grain size. Hardness which estimated through grain size from SEM showed that the sample of 20 shots off-normal should own the highest hardness, which accords with the hardness results. On the other hand, over-heated process may lead to the lower hardness in the sample of 20 shots normal as compared with the sample of 10 shots normal.

IV. Conclusion

Carbon films produced through the ablation of graphite by intense pulsed ion beam using a 20 kJ PF device is reported. Copper impurities, which were found in XRD results, were subsequently observed in SEM micrographs. All the films showed reasonably smooth surface with nano-sized agglomerates. Studies on Raman spectra by analyzing Raman shift and band intensity ratio inferred that sp^3 content in the sample of 20 shots off-normal should be highest. Hardness results indicate that sample of 20 shots off-normal owns the highest plastic hardness among these three samples. Hardness results also showed very good agreement with SEM and Raman results. Over-heated process is believed to be the reason of poor hardness of the sample of 20 shots normal.

Reference:

1) Hussain S, Ahmad S, Sharif M, Sadiq M, Waheed A and Zakaullah M 2006 *Phys. Lett.* A **349** 236–44

2) Zakaullah M, Waheed A, Ahmad S, Zeb S and Hussain S 2003 *Plasma Sources Sci. Technol.* 12 443–8

3) J M Koh, R S Rawat, A Patran, T Zhang, D Wong, S V Springham, T L Tan, S Lee and P Lee 2005 *Plasma Sources Sci. Technol.* **14** 12-18

4) H.R. Yousefi, S.R. Mohanty, Y. Nakada, H. Ito and K. Masugata Phys. Plasmas 13, 114506 (2006)

5) Soto L 2005 *Plasma Phys. Control. Fusion* 47 A361–81

6) L.Y. Soh, P. Lee, X. Shuyan, S. Lee, R.S. Rawat, IEEE Trans. Plasma Sci. 32 (2004) 448.

7) Z.P. Wang , H.R. Yousefi, Y. Nishino, H. Ito, K. Masugata, Physics Letters A 372 (2008) 7179−7182

8) Bhuyan H, Mohanty S R, Borthakur T K and Rawat R S 2001 *Indian J. Pure Appl. Phys.* **39** 698–703

9) Kelly H, Lepone A, Marquez A, Sadowski M, Baranowski J and Scladnik-Sadowska E 1998 IEEE Trans. Plasma Sci.26 113

10) J.Roberson, Materials Science and Engineering R 37 (2002) 129-281

11) C.P. Klages, Appl. Phys. A 56, 513 (1993)

12) L. Holland and S. M. Ojha, Thin Solid Films 58, 107 (1979)

13) H. Vora and T. J. Moravec, J. Appl. Phys. 52, 6151 (1981).

14) Bong Geun Choi, Jae Kwang Kim, Won Jae Yang and Kwang Bo Shim, Journal of Ceramic Processing Research. Vol. 6, No. 2, pp. 101~105 (2005)

15) I.A. Khan, M. Hassan, R. Ahmad , A. Qayyum, G. Murtaza, M. Zakaullah, R.S. Rawat, Thin Solid Films 516 (2008) 8255 −8263

16) R.S. Rawat, Applied Surface Science 255 (2008) 2932–2941.

17) C.R. Kant, M.P. Srivastava, R.S. Rawat, Phys. Lett. A 226 (1997) 212-216.

18) S. Zeb et al., Mater. Chem. Phys. 103 (2007) 235

19) M.V. Roshan et al. / Applied Surface Science 255 (2008) 2461−2465

20) Zakaullah M, Akhtar I, Murtaza G and Waheed A 1999 Phys. Plasmas 6 3188

21) K. Takao et al. Plasma Sources Sci. Technol. 12 (2003) 407–411

22) N. H. Cho, D. K. Veirs, J. W. Ager III, M. D. Rubin, C. B. Hopper, and D. B. Bogy, J. Appl. Phys. 71, 2243 (1992)

23) C.S. Lu, Y.W. Mai, Y.G. Shen, J. Mater. Sci. 41 (2006) 937.

ADVANCED FUELS FUSION IN HIGH DENSE PLASMA LIKE -PLASMA FOCUS DEVICE

H. R. Youse , T. Haruki, J. I. Sakai, H.Ito, and K. Masugata

Department of electric and electronic system, Faculty of Engineering,
University of Toyama, 3190 Gofuku, Toyama 930-8555, Japan
(Dated: June 1, 2009)

In order to understand the heating process during $proton - boron^{11}$ ($P - B^{11}$) fusion in a high density pinched plasma, we investigate the coalescence of two current loops, consisting of two ion species (protons, boron), using an electromagnetic relativistic particle-in-cell code. We found that the boron and protons can be heated up to energies of respectively MeV and $400 keV$, in the direction perpendicular to the current. The electron temperature in the x- and y-direction is approximately 100 keV. The heating mechanism is due to the generation of transverse electric elds by the spacial charge separation of the two ion species. The plasma is con ned near to the core of pinched lament by a 180 million gauss magnetic eld. We found that the ratio between the output fusion power density and the initial input energy density is approximately 330. We conclude that $P - B^{11}$ fusion using a high density plasma in a plasma focus device is achievable.

PACS numbers:

I. INTRODUCTION

For more than 50 years, research towards a fusion reactor has been pursued in most of the industrialized countries in the world [1]. Most of the current studies and experiments on nuclear fusion are devoted to the Deuterium-Tritium (DT) fuel cycle, which emits 80% of its energy in the form of high-energy neutrons, since it is the easiest way to reach ignition. There are two significant disadvantages to the DT cycle; radiation damage and radioactive waste products [2]. It would therefore be desirable to achieve controlled fusion with other more advanced fuels, which minimize the production of neutrons. Recently, this goal has become more urgent, due to the lack of su cient safe and clean energy production in the world. Currently, the most promising advanced fusion fuels are $proton - boron^{11}$ [P+$B^{11} \rightarrow 3\alpha$ (8.7MeV)] and $deuterium - helium^3$[D+$H_e^3 \rightarrow$ p (14.7MeV) $+\alpha$ (3.7MeV)]. However, the cross-section for these fuels is appreciable only when the ion-temperature T_i exceeds 100 keV for $P - B^{11}$, and 50 keV for $D - H_e^3$ [3, 4]. The main obstacle for using the H_e^3 is scarcity of H_e^3 on Earth [5]. Hydrogen-boron fuel generates nearly all its energy in the form of charged particles, not neutrons, thus minimizing or eliminating induced radioactivity [6]. For $P - B^{11}$, Dawson [7] pointed out that the bremsstrahlung power loss at temperatures of 200 keV is greater than the power generated by fusion, which makes self-burning unlikely. To avoid the bremsstrahlung losses, the electron temperature T_e must be much lower than the ion temperature T_i, but not too low since the fusion byproducts are preferentially stopped by the ions [7, 8]. Son et al. [11] emphasize the point that accessing a regime in which $T_i >> T_e$ is always useful for achieving controlled fusion. In view of this, the electron temperature must be in a narrow range around 100 keV to retain the possibility of self-burning [7, 8-10]. To reduce bremsstrahlung losses, which mainly depend on the boron number density n_B (because of Z^2), compression of the fuel to an ultra dense state to create hot spots is required [11]. This can be achieved in a dense plasma focus [12, 13] where, for self-burning fusion, we aim to obtain a ratio of fusion power density to bremsstrahlung power density (W/P_B) of approximately one. The ratio of boron to proton number density (n_B/n_p) in the present simulation was calculated by use of following equations: the fusion power density (c.g.s.) for $T_i \geq 200$ keV is $W(erg/cm^3 s) = 5.4$ $10^{-21} n_p n_B$, while the Bremsstrahlungpower density (c.g.s.) is $P_B(erg/cm^3 s) = 1.5$ $10^{-25}(1+5\epsilon)(1+25\epsilon)$ $n_p^2 T_e^{1/2}(1+2T_e/m_e c^2)$, where $\epsilon = n_B/n_p$, T_e and $m_e c^2$ must be given in eV [14]. The boron to proton number density ratio was set to $n_B/n_p = 1/9$.

Recently Sandia National Laboratories reported an ion temperature T_i of over 200 keV; a record temperature for a magnetically con ned Z-pinch plasma [15]. However, fusion with such fuels requires average ion energies above 100 keV in a dense plasma. In plasma focus (PF) type discharges, the initial breakdown occurs across the insulator in the from of laments. These laments are blown o the insulator by the magnetic pressure, and 1 s after breakdown merge to form a uniform thin parabolic current sheath between the electrodes. The plasma sheet carrying the current is formed between the anode and cathode. The **J** **B** force causes this current to move to the anode end, generating pairs of laments in the process. The plasma sheet and laments contract towards the center and energy is transferred from the outer region to the central region. The plasma sheet and laments continue contracting into the center to make the pinch. The experimental results indicated that local electron concentrations in the hot spots or plasmoids can exceed $10^{20} - 10^{21} cm^{-3}$, while the local electron temperatures can obtain values above 1 keV [12, 13].

II. SIMULATION MODEL

In this study, we attempt to answer the important question of whether sufficient heating can occur during $P - B^{11}$ fusion. In continuation from previous work [16, 17], we have simulated the coalescence of two current loops, consisting of two high density ion plasma species (protons, boron), using an electromagnetic relativistic Particle-In-Cell (PIC) code.

We have redesigned the original *TRISTAN* code [18] into an object-oriented type PIC code, in order to treat multi-species plasmas and various ions heavier than protons. The numerical scheme is identical to the original *TRISTAN* code. In PIC codes, both the electron and ion dynamics are described as particles, with equations of motion given by: $d_t \vec{v}_{si} = (q_s/m_s)(\vec{E} + \vec{v}_{si} \times \vec{B})$ with $d_t \vec{r}_{si} = \vec{v}_{si}$. These equations are solved for each particle along with with Maxwell's equations: $\partial_t \vec{E} = c^2 \nabla \times \vec{B} - (1/\epsilon_0)\Sigma_s \vec{j}_s$ and $\partial_t \vec{B} = -\nabla \times \vec{E}$. The subscript s and i denote respectively the plasma species ($s = p$ for protons, B for boron, and e for electrons) and the i-th particle index. In addition to the above mentioned equations, $\nabla \cdot \vec{B} = 0$ and $\nabla \cdot \vec{E} = \rho_e/\epsilon_0$ are automatically satisfied at all times due to the nature of the numerical scheme (ρ_e is electric charge density). Initially, the plasma is charge neutral.

The lengths of the system in two dimensions are $L_x = L_y = 500\Delta$ (not including ghost cells), where $\Delta = 1$ is the spatial grid size which corresponds to the Debye length. Proton, boron and electron plasmas are initially uniformly distributed throughout the system. In order to produce two current loops oriented in the z direction, we drive the electric field E_z circularly at two locations: $(x_d, y_d) = (190\Delta, 250\Delta)$ and $(310\Delta, 250\Delta)$. The external driving of E_z is imposed between $\omega_{pe}t = 2.5$ and 25.0 as follows: $E_z = 0.5E_{ext}[tanh((t - 50)/20) - tanh((t - 500)/20)] \times 0.5[tanh((r_1 + r_d)/5) - tanh((r_1 - r_d)/5) + +tanh((r_2 + r_d)/5) - tanh((r_2 - r_d)/5)]$ where the radius of the circle excitation is set at $r_d = 50\Delta$, $r_1 = \sqrt{(x - 190)^2 + (y - 250)^2}$, and $r_2 = \sqrt{(x - 310)^2 + (y - 250)^2}$. Periodic boundary conditions are applied to both the electromagnetic fields and the particles.

The other parameters are as follows: the simulation time step $\omega_{pe}\Delta t = 0.05$ ($\Delta t(= 1)$ is the time interval of the calculation), The electron skin depth $c/\omega_{pe} = 10\Delta$, the mass ratios $m_B/m_p = 11$ and $m_p/m_e = 1836$, and finally the electric charge $q_p = -q_e, q_B = 5q_p$ (we consider fully ionized boron). As discussed in the introduction, we choose the ratio of boron to proton number density as $n_B/n_p = 1/9$. Therefore, the particle number densities per cell are given by $n_p : n_B : n_e = 90 : 10 : 140$. The initial temperature, $T_p = T_B = T_e$. The electron thermal velocity to the speed of light is $v_{te}/c = 0.1$. In this paper, time is normalized by the electron plasma frequency, ω_{pe}, while the spatial scale is normalized by the electron skin depth, $d_e (= c/\omega_{pe})$.
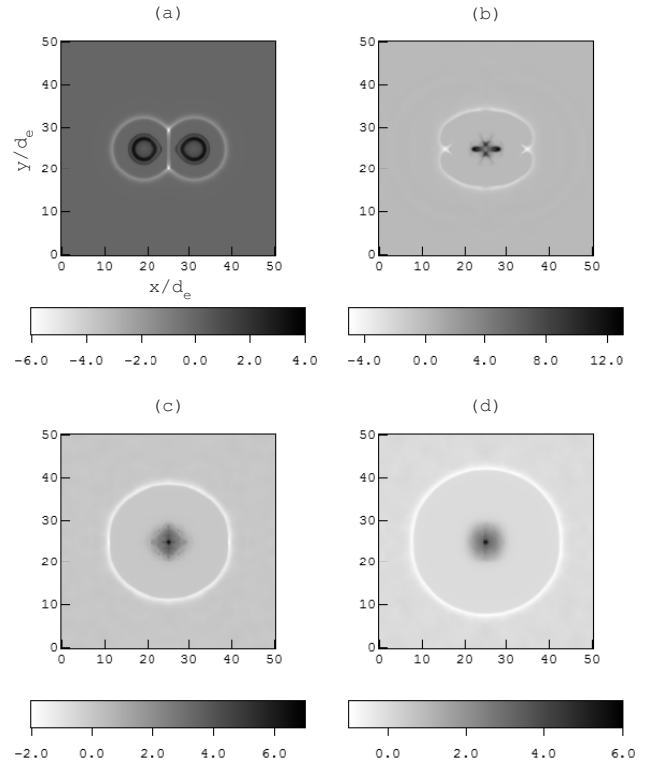
FIG. 1: Time evolution of the spatial distribution of current density $j_z/(n_e qc)$ at (a) $\omega_{pe}t = 10$, (b) 30, (c) 250, and (d) 500.

III. SIMULATION RESULTS

We present the dynamics of the current coalescence process in Fig.1, where the time evolution of the spatial distribution of the current density $j_z/(n_e qc)$ is shown at (a) $\omega_{pe}t = 10$, (b) 30, (c) 250, and (d) 500. Before $\omega_{pe}t = 10$, we observe return currents surrounding the locations of the external electric field driving. As seen in Fig.1, two shell-like current loops, with return currents, begin to coalesce with the core parts of currents merging into one. The average current density J_z obtained from the simulation is approximately $2.0n_e qc$, which gives $J_z \simeq 2.8 \times 10^{19} statampare/cm^2$, if we use $n_e = 10^{18}cm^{-3}$. Currently, for typical pulsed generators used for plasma focus devices, the total current is approximately 1 MA. Assuming that the number of filaments is 48 and the radius of each filament is $10^{-3}cm$, then the current density J_z for each filament is $J_z = 2 \times 10^{19} statampare/cm^2$, which is comparable with our simulation results. The azimuthal magnetic field produced by the pinched current arises between the inner (dark) and outer (white) circular current filaments. The resulting Lorentz forces therefore explain the expansion of the outer filament, as well as the contraction of the inner one. In Fig. 2 we show simulation results of the spatial distribution of number density for (a) protons, (b) boron, and (c) electrons. In (d) we show the electric field vector E_x/E_0 vs. E_y/E_0 at $\omega_{pe}t = 250$. n
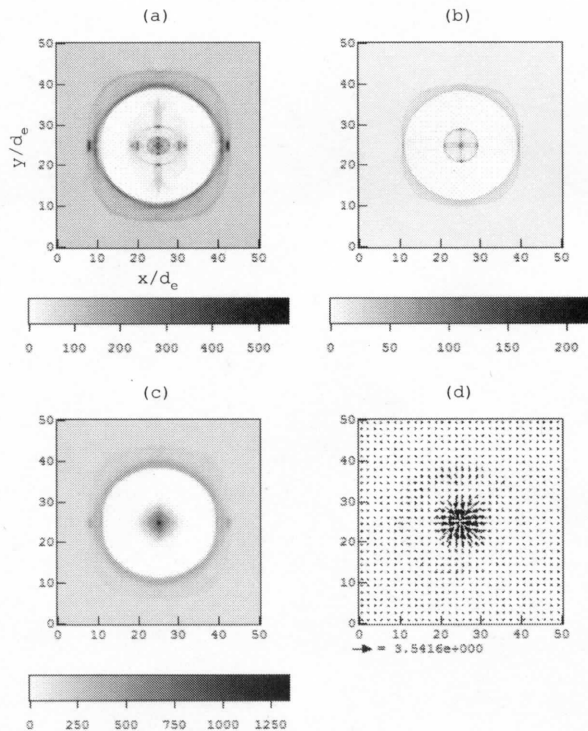
FIG. 2: Simulation results of the spatial distributions of (a) proton, (b) boron, and (c) electron number densities n, and (d) the electric field vector E_x/E_0 vs. E_y/E_0 at $\omega_{pe}t = 250$. n is the number of particles per cell and $E_0 = m_e c \omega_{pe}/q$.

FIG. 3: Phase-space plots of $V_x - X$ for electrons (top), boron (middle) and protons (bottom), at $\omega_{pe}t = 250$.

is the number of particles per cell and $E_0 = m_e c \omega_{pe}/q$. As seen in Fig.2(c), most electrons are concentrated near the center of the system, due to self-pinching. The maximum electron density becomes more than ten times than the initial value. A small portion of the electrons are located outside of the ring-shell structure where the return current exists. The heavy boron and protons are distributed both inside and outside of the core electrons. The heavy ion distribution is not completely canceled by the core electrons, resulting in the strong transverse electric fields, as seen in Fig. 2(d). The electric field vectors show that near the center the electrons are rich, while outside the core the positive ions are rich. In the discussion section, these transverse electric fields are shown to play an important role in the heating of the heavy ions.

Figure 3 shows the phase space plots of $V_x - X$ for electrons (top), boron (middle) and protons (bottom), at $\omega_{pe}t = 250$. As seen in this figure, the most heated proton and boron particles are located near the center of the system.

Figure 4 shows the velocity distribution functions of (a) protons, (b) boron, and (c) electrons at $\omega_{pe}t = 500$. The solid, dotted, and dashed lines show the x, y, and z components of the velocity, respectively. The notation f means the particle number, while the velocity is normalized by the speed of light. Both protons and boron are heated mainly in the x- and y-directions, with each hav-

ing both high and low temperature distributions. The peak temperatures of the protons and boron are respectively 400 keV and 1 MeV. The electron temperature in the x- and y-direction is approximately 100 keV. The dominant heating of both boron and protons occurs in the x- and y-directions, as seen in Fig.3 (middle and bottom). The heating mechanism is due to the electric field perpendicular to the current (z-direction), as seen in Fig. 2(d). This electric field is generated by charge separation between the core electrons and heavy ions.
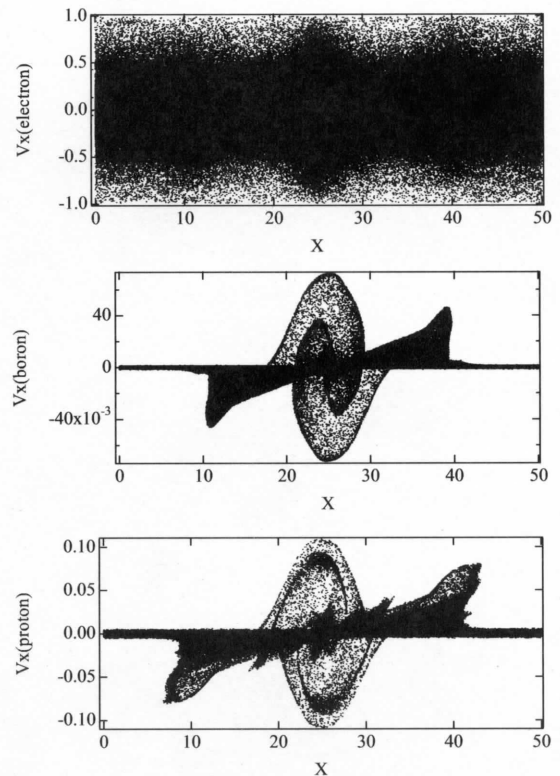
The strong pinched current can generate magnetic fields (B_x and B_y) of ≈ 180 Mega gauss, if we take the plasma density as $n = 10^{21} cm^{-3}$. The pinched plasma is confined by this self-generated magnetic field. In real 3-D configurations kink and sausage instabilities are possible, therefore we need to explore the loop coalescence in a fully 3-D simulation. One possible stabilizing effect in this configuration is the existence of the return current outside the current filament.

Finally, we estimate the ratio between the output fusion power density and the initial input energy (from the external electric field). The fusion power density is given by $5.4 \times 10^{-21} n_p n_B (erg/cm^3 s)$ which gives us $\approx 2.4 \times 10^{20} (erg/cm^3 s)$, if we use $n_p = (9/14)10^{21} cm^{-3}$ and $n_B = (1/14)10^{21} cm^{-3}$, assuming that the final pinched electron plasma density is $n_e = 10^{21} cm^{-3}$. The initial

FIG. 4: The velocity distribution functions of (a) protons, (b) boron, and (c) electrons at $\omega_{pe}t = 500$. The solid, dotted, and dashed lines respectively show the x, y, and z components of the velocity. The notation f means the particle number, and the velocity is normalized by the speed of light.

IV. CONCLUSIONS

We numerically investigated the coalescence of two current loops, consisting of two high density ion plasma species (protons and boron), using an electromagnetic relativistic particle-in-cell code. We attempted to understand the heating processes that occur during $P - B^{11}$ fusion in a pinch plasma. We found that the boron and the protons can be heated up to respectively MeV and 400 keV temperatures, in the direction perpendicular to the current. The electron temperature in the x- and y-direction was approximately 100 keV. The heating mechanism is due to transverse electric elds generated by the spacial charge separation, due to the existence of two ion species. The present simulation results indicate that we could obtain the required conditions for $P - B^{11}$ fusion; ion temperature greater than 100keV, and a large temperature di erence between electrons and ions. The self-generated magnetic eld of 180 Mega gauss can con ne the plasma near the core of pinched lament. We found that the ratio between the output fusion power density and the initial input energy to the plasma (from external electric eld driving) is 330. We conclude that $P - B^{11}$ fusion using a high density plasma in a plasma focus device is achievable.

[1]N. Rostoker, M. W. Binderbauer, and H. J. Monkhorst, Science 278 (1997) 1419.

[2] G. L. Kulcinski and J. F. Santarius, Nature 396 (1998) 724.

[3] G.H. Miley, H. Towner, N. Ivich, Fusion cross-sections and reactivities, Report C00-2218-17 (1974).

[4]J.R. Mcnally, Nucl. Fusion 11 (1971) 187.

[5] T.Honda, Y.Nakao, Y.Honda, K.Kudo, Nucl.Fusion 31 (1991) 851.

[6] V.S.Belyaev,A.P.Matafonov, V.I.Vinogradov et al.,Phys. Rev. E 72 (2005) 026406.

[7] J. Dawson, Fusion, Academic Press, New York, Vol. 2 (1981).

[8] S. Eliezer, J.M. Martinez-Val, Laser Particle Beams 16 (1998) 581.

[9] C. Sche el, R.J. Stening, H. Hora, et al., Laser Particle Beams 15 (1997) 565.

[10] Y. Setsuhara, H. Azechi, N. Miyanaga, et al., Laser Particle Beams 8 (1990) 609.

[11] S. Son, N.J. Fisch Physics Letters A 329 (2004) 76.

[12] P.Silv and M.Favre J.Phys.D:Appl..Phys. 35 (2002) 2543.

[13] L. Jakubowski, M.J. Sadowski and E.O. Baronova, Nucl.Fusion 44 (2004) 395.

[14] J.M.Martinez-val, S.Eliezer, M.Piera,G.Velarde Physcs Letters A 216 (1996) 142.

[15] M. G. Haines, P. D. LePell, C. A. Coverdale, B. Jones, C. Deeney, and J. P. Apruzese, Phys.Rev.Lett. 96 (2006) 075003.

input energy is given by the time and space integral of $J_z E_z$. Here we use the electromagnetic eld energy produced by the current J_z instead of the time and space integral of $J_z E_z$. The electromagnetic eld energy density per surface of the simulation domain is given by $E_{input} = 4 \cdot 10^2$, where it is normalized by the electron thermal energy density $(0.5 m_e n_e v_{th}^2)$ per surface of the simulation domain. Therefore, $E_{input}/\tau_d L^3 (erg/cm^3 s)$ where τ_d is the input energy period given by $\tau_d = 22.5/\omega_{pe}$ and L is the length of the current lament. If we use $L = 10cm$ and an initial electron thermal energy of 10eV, then we obtain the input energy density as $7.1 \cdot 10^{17}(erg/cm^3 s)$. Finally, the ratio between the output fusion power density and the initial input energy density is $2.4 \cdot 10^{20}/7.1 \cdot 10^{17} = 330$. The Bremsstrahlung-power density (c.g.s.) is $P_B(erg/cm^3 s) = 1.5 \cdot 10^{-25}(1 + 5\epsilon)(1 + 25\epsilon) \quad n_p^2 T_e^{1/2}(1 + 2T_e/m_e c^2)$ that can be estimated as $P_B = 1.5 \cdot 10^{20}(erg/cm^3 s)$. This value is less than the fusion power density, $2.4 \cdot 10^{20}(erg/cm^3 s)$.

[16] T.Haruki, H.R.Youse , K.Masugata, J.I.Sakai, Y.Mizuguchi, N.Makino, and H.Ito, Phys. Plasmas 13 (2006), 082106.

[17] Y. Mizuguchi, J.I.Sakai, H.R.Youse , T. Haruki, and K.Masugata, Phys. Plasmas 14 (2007), 032704.

[18] O. Buneman, Computer Space Plasma Physics:Simulation Techniques and Software, Ed. H. Matsumoto and Y. Omura (Terra Scienti c Publishing Company) (1993).

Plasma Dynamics in Counter-Facing Plasma Guns

Yutaka Aoyama*, Mitsuo Nakajima, and Kazuhiko Horioka*

*Department of Energy Sciences, Interdisciplinary Graduate School of Science and Engineering,
Tokyo Institute of Technology, 4259 Nagatsuta, Midori-ku, Yokohama 226-8502, Japan*

A plasma focus system, which consists of a pair of counter-facing coaxial plasma guns, has been developed and the behavior of current sheets in the plasma gun was investigated using a fast framing camera and an EUV photo-diode. With a trigger assist of flashover on the insulator surface and a connection of outer electrodes, current sheets were induced to collapse and shrink to the center of the electrodes, which made an ellipsoidal high energy density plasma. In case of the collapse mode, we have observed multi-EUV emissions with several μsec duration, which indicate that the current path can compress and confine the plasma at least for several μsec. This plasma focus system is expected to drive a long-lifetime and efficient extreme-ultraviolet plasma source.

Keywords: Plasma confinement, EUV light source, Plasma focus, High energy density plasma

I.   INTRODUCTION

Both high average power and high conversion efficiency are needed for a practical light source of EUV (Extreme Ultra-Violet) lithography. Mo/Si multi-layered mirror has been developed to the lithography which has sensitivity in 13.5 nm$\pm$ 1 %(in-band range). High energy density plasmas have been investigated for the bright and cost-effective in-band EUV source. The plasma light source is needed to improve the conversion efficiency because of a huge heat load onto the components.

The plasma conversion efficiency (P.C.E) can be represented as

$$P.C.E = \frac{P_{out} \times S.E. \times}{P_{in} \times T} \tag{1}$$

where, P_{in} is power into the light source plasma, T is the time duration of input power, P_{out} is total radiation power, $S.E$ is spectral efficiency represented by $S.E = P_{inband}/P_{out}$ and   is the EUV emission duration. Input energy are mostly run away with heating and ionizing the plasma in early stage of the plasma formation and the compressed plasma should expand immediately due to internal pressure and instability of fast pinching plasma. Then the P.C.E of conventional EUV source is dominated by a very short lifetime   of the pinching plasma. On the other hand, it was estimated that the P.C.E approaches to S.E when   come to several μsec [1, 2]. Therefore, prolonging the lifetime   is considered to be the most feasible way to improve the P.C.E.

Spectral efficiency essentially depends on the plasma element and condition. So far, Xe, Sn and Li have been investigated[6–11] because they have relatively a lot of spectrum in the in-band region. The optimum electron density is estimated to be $n_e \sim 10^{18} cm^{-3}$ and electron temprature $T_e \sim 30$[eV] for Xe and Sn, $n_e \sim 10^{18} cm^{-3}$ and $T_e \sim 18$[eV] for Li plasma. Therefore, light source plasma should have high energy density, high controlla-
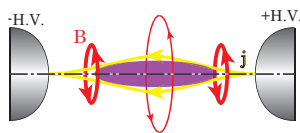
FIG. 1: Image of 2-dimensional compression and plasma confinement between the center electrodes
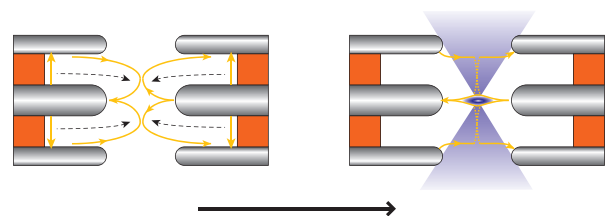
FIG. 2: A schematic diagram of plasma behavior in counter-facing plasma guns

_____

*Electronic address: `khorioka@es.titech.ac.jp`

bility and stability.

Laser Produced Plasma (LPP) makes the EUV emission plasma with high power laser[3, 4]. As the LPPs don't have plasma controllability, the laser heated plasma freely expands. On the other hand, Z-pinch is used for Discharge Produced Plasma (DPP), which is basically 1-demensional compression scheme and can't confine the plasma for $\sim \mu$ sec because of axial fast pinch instability. In addition, thermal velocity of the EUV plasma is estimated to be up to ~ 1 cm/μsec for axial direction. Therefore 2-demensional (axial and radial) compression is required to prolong the life time of EUV plasma.

We have confirmed that the plasma lifetime can be prolonged about twice of conventional pinch plasma with quasi-2-dimensional (oneside-axial and coaxial) compression with a tapered capillary discharge. In this paper, we show that high energy density plasma can be confined for several μsec by a 2-dimensional compression. We propose a DPP source composed of counter-facing plasma guns for the plasma confinement and investigate the plasma dynamics in it.

II. COUTER-FACING PLASMA GUNS

The concept of 2-dimensional compression is shown in Fig.1. An ellipsoidal current path is expected to be able to make a 2-demensionally confined plasma, i.e., self-magnetic pressure compress radial direction and magnetic pressure gradient suppresses the particle loss to axial direction. The ellipsoidal current is robust against the plasma instability because this form is considered to be intrinsically stable against MHD(Magneto Hydro-Dynamics) instability. In order to make the current path, a plasma focus system consists of a pair of counter-facing coaxial electrodes was developed. The outer guide electrodes are grounded to the same earth and the center bar electrodes are applied high voltages with reversed polarity. Current sheets are made at the insulator surfaces and electro-magnetically driven to the center of the electrodes by the magnetic pressure. When we make proper discharge conditions, the current sheets are expected to collapse and shrink to the center of the electrodes.

The behavior of current sheet collapse is schematically shown in Fig.2. The current sheets are expected to bridge the center electrodes after the collapse because the center electrodes are charged with opposite polarities. After the connection, the current path forms a stable shape to compress and confine the plasma both in radial and axial directions. In order to realize this scheme, there are 4 important points: (1) uniform current sheet formation along the surface of insulator; (2) rundown of the current sheet toward the center of the gaps with low jitter; (3) reconstruction of the current distribution after the sheet collision; (4) formation of an ellipsoidal high-energy density plasma and maintaining it for a long period in the center gap.

In this paper, the counter-facing plasma guns are investigated with particular emphasis on these 4 points, using high speed framing photography and EUV measurements.

III. EXPERIMENTAL SETUP

The plasma gun consists of a pair of coaxial electrode, one of which is faced to the counter electrodes with 4mm gap. Then the focus system has a pair of ground electrodes with 10 mm inside diameter, and a pair of center-bar electrode 5mm in diameter. As an assist of breakdown, the insulator surfaces were coated with a quasi-conductor layer consisted of carbon nano clusters and an insulating oil. The circuit capacitance is 2×0.4 μF, charged voltages are nominally $\pm$ 15 kV. To increase the period of the discharge, we put inductance of 0.4-1.3 μH into the discharge circuit. Initial filling gas pressure has been kept about 230 [mTorr] with continuous Xe gas supply and a pumping.

Currents have been monitored with Rogowski coils (model 110, PEASON ELECTRONICS) placed near the capacitance ground sides.

A high speed framing camera (IMACON468, DRS HADLAND) has sensitivity in optical wavelength, which can take 4 frame images, 80 nsec after the trigger signal. Exposure time for the framing images is 10 nsec. The framing camera was usually set on the right angle of electrode axis, through the observation window.

An EUV photo-diode (AXUV20HS1, IRD) has sensitivity in 11 $\sim$ 17 nm bandwidth with a sensitivity peak about 13 nm and nsec time resolution. The EUV diode was set on the opposite side of the framing camera and 100 mm apart from the plasma spot. In order to trap high speed electrons and the plasma, a transverse magnetic field of 5 k-gauss was applied with permanent magnets.
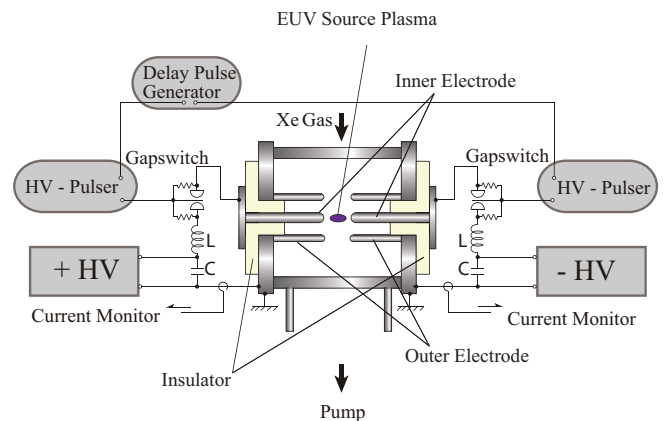
FIG. 3: Apparatus of discharge system

(a)Without trigger assist   (b)With carbon coating
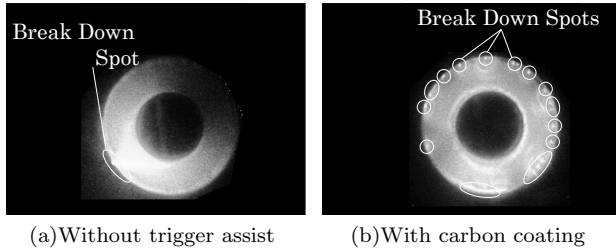
FIG. 4: Framing images (front-view) of the insulator surface of coaxial electrodes immediately after breakdown, without (a) and with (b) breakdown assist

(a)Collapse mode (1)   (b)Collapse mode (2)

(c)Connection mode (1)   (d)Connection mode (2)
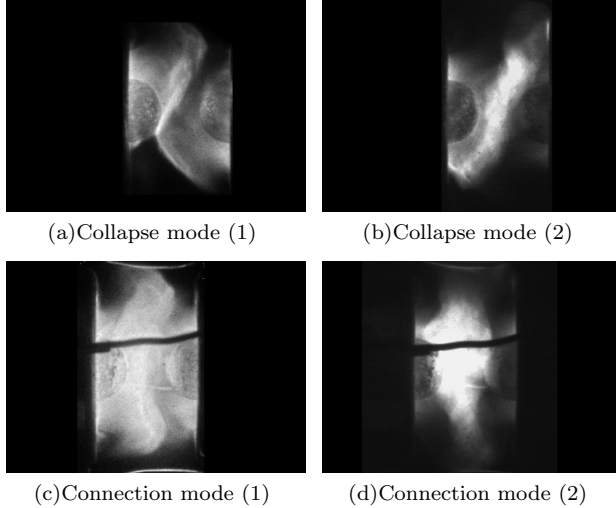
FIG. 5: Framing images (side-view) of plasma behavior in collapse (a),(b) and connection (c),(d) modes with and without the connection of outer electrodes

IV. RESULTS AND DISCUSSION

A. Current sheet uniformity

Framing images of the insulator surface are shown in Fig.4. They are taken from the axial direction of coaxial electrode. As shown with the figure, without trigger assist, the gun doesn't have discharge stating point. Although we have tried various trigger schemes, we could make uniform current sheet only by using pre-conductor coating on the insulator surface. The pre-conductor coating was made by nano carbon spray (DENSUKE, TOYO DRILUBE), in which, a lot of nano carbon clusters are mixed in squalene.

B. Discharge jitter

The trigger assist also improved the discharge jitter. As the coaxial electrode doesn't have edge, the break-down time has jitters of several hundreds nsec range without trigger assist. With pre-conductor coating, variance in the operation of coaxial electrodes reduced less than 10 percent ($\sim$25nsec) of that of no trigger assist. When we consider the requirement for current sheet collision at the center of the electrodes from the sheet drift speed and electrodes gapwidth, the variance should be less than 50 nsec. This means that the trigger assist by carbon coating can reduce the jitters less than the required level.

As the carbon and hydrogen component in the pre-conductor coating have not in-band spectra, we think these impurities didn't affect the photodiode output.

For a more practical application of the light source, a reproducible inlet mechanism is essential to introduce the selected material into the base of the electrode. By providing liquid Li through a porous ceramics placed between the electrodes, we will be able to make a Li plasma, which is expected to fulfill both high sepectral efficiecncy and low trigger jitter.

C. Plasma dynamics in the plasma gun

Plasma dynamics had 2 patterns depending on the electrode configuration. Framing images of them; connection mode and collapse (no-connection) mode, are shown in Fig.5. The collapse phase emits EUV strongly because the drifting plasma is thermalized by the stagnation in the gap center. On the other hand, the plasma is compressed by connecting current in the connection mode. We could make clear that the formation processes of the connection and collapse modes are effected by electrical conductivity of the current path between facing electrodes. In the collapse mode, current path between the outer-ground electrodes come down because the plasma is moved away by the magnetic pressure. In the connection mode, 4-wires made of copper were set to make the current path, which realize the EUV-plasma confinement.

EUV emission in the connection mode is shown in Fig.6. The light green bar in Fig.6 shows the time of framing images in Fig.5 (c),(d). Multi-EUV emissions have been detected with the discharge. FWHM (Full Width at Half Maximum) of the EUV signal is estimated to be 540 [nsec] on average of initial four half waves, which is much longer than conventional DPP. This result indicates ellipsoidal current distribution (Fig.1) compress the plasma to EUV condition and confine it stably for several μsec. The current sheets push the plasma to the gap of center electrodes, after then compress and confine several times. The compressed plasma condition varies with initial condition, EUV emission repetitively occurs every confinement processes.

The result that the EUV emission decreases along with the discharge current, indicates that the EUV plasma is not disappeared by the instability but just by the decay of discharge current. The plasma lifetime is expected to be prolonged by driving it with longer current waveform.

FIG. 6: Waveforms of discharge current and EUV emission with connection mode

Pulse	FWHM	Total emission	Efficiency	Fluctuation
Short	540 [nsec]	1	1	0.89
Long	1280 [nsec]	7.15	3.47	0.31

TABLE I: Effects of pulse length on the EUV emission, conversion efficiency, and its fluctuation
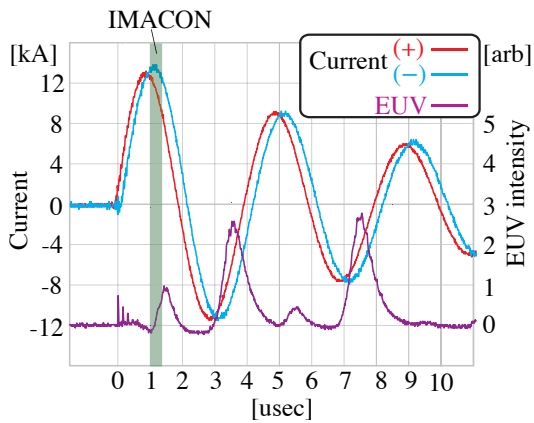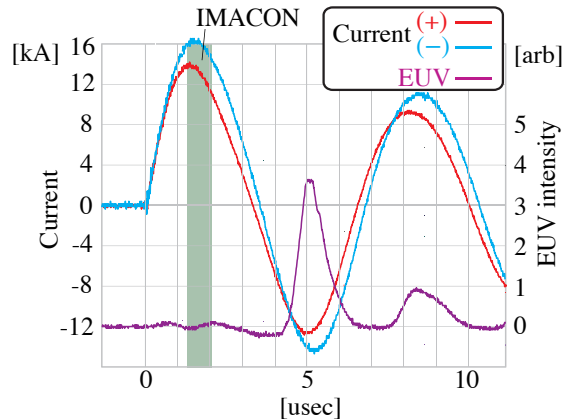
FIG. 8: Discharge current and EUV emission with Collapse mode

FIG. 7: Waveforms of discharge current (long-pulse) and EUV emission with connection mode

connection mode, counter-facing plasma guns are able to compress and confine the EUV plasma stably every halh period of discharge for several μsec duration.

D. Effect of current waveform

We examined effects of current waveform on the EUV emission. When current is driven with PFN (Pulse Forming Network) which has two capacitance units, EUV emission is prolonged as shown in Fig.7. With this modification, the discharge period was extended to 7μsec from 4μsec. Multiple-EUV emissions were also detected with the discharge, which have 1.3 μsec FWHM of EUV signals on average every half period of the discharge. This result confirms the formation of plasma with stably confinement mode. The pulse width effect is summarized in TABLE.I. Total EUV emission and conversion efficiency are normalized with those of the short pulse case, which have been considerably improved in the long pulse mode. Fluctuation of total EUV emission and stability of EUV emission were also improved by driving the focus system with the long pulse current. This result shows that, in the

E. Collapse mode

On the other hand, photo-diode signal in the case of the collapse mode is shown in Fig.8. We took off the ground attachment to make the collapse mode. The framing images of plasma dynamics in the light bar are shown in Fig.5(a),(b). EUV signal wasn't detected in the first current peak as shown in Fig.8. The drift speed of focus plasma was estimated to be about 1.2×10^4 m/sec. The plasma kinetic energy is thermalized by the collision of current sheets. If the plasma stagnate completely, the plasma speed is corresponding to several 10 eV. However, the plasma wasn't compressed and heated enough to EUV region, because current path doesn't connect and the compressed plasma behaved in the collapse mode. After the first pulse, EUV emission was detected for several half of wavelength because plasma was preheated by the previous current sheet, which improve conductivity between electrodes and current path is connected at the electrodes.

V. SUMMARY

We have investigated the plasma dynamics in a plasma focus system composed of couter-facing plasma guns and observed multi-EUV emissions with several μsec time duration. The current sheet driven by magnetic pressure, accumulate the plasma to the center of facing electrode gap, which forms an ellipsoidal contour of current distribution. The current path which compresses and confines the plasma for several μsec in the connection mode. The ellipsoidal current distribution is robust against the instability of high energy density plasma. All of the results indicate that with proper current waveform, this configuration of plasma gun is expected to prolong the EUV plasma lifetime to more than μsec and have a potential for both high power and high efficiency EUV source.

Careful selection of the plasma gun parameters from the current to the pulse driver as well as the plasma source should realize optimum conditions for EUV emission. In the proof-of-principle experiments, a pre-filled Xe gas was used along with the breakdown assist at the base of the electrodes[5]. We are planning to operate the device with Li source in the future works, which will be compatible with both steady breakdown assist and high spectral efficiency.

[1] M. Masnavi, M. Nakajima, E. Hotta, and K. Horioka, "Estimation of optimum density and temperature for maximum efficiency of tin ions in Z discharge extreme ultraviolet sources" J. Appl. Phys. 101, 033306 (2007)

[2] M. Masnavi, M. Nakajima, E. Hotta, and K. Horioka, "Estimation of the Lyman-α line intensity in a lithium-based discharged plasma source" J. Appl. Phys. 103, 013303 (2008)

[3] T. Hosokai, T.Yokoyama, A. Zhidkov, H.Sato, E.Hotta, and K. Horioka, "Elongation of extreme ultraviolet (at 13.5nm) emission with time-of-flight controlled discharges and lateral fuel injection" J. Appl. Phys. 104, 053306 (2008)

[4] T. Hosokai, T.Yokoyama, A. Zhidkov, H.Sato, K. Horioka, and E. Hotta, "High brightness extreme ultraviolet (at 13,5nm) emission from time-of-flight controlled discharges with coaxial fuel injection" J. Appl. Phys. 104, 053305 (2008)

[5] Y. Aoyama, M. Nakajima, and K. Horioka, "Counter-facing plasma focus system as a repetitive and/or long-pulse high energy density plasma source", Phys. of Plasmas., to be published (2009)

[6] V. M. Borisov, A. V. Eltsov, A. S. Ivanov, Y. B. Kiryukhin, O. B. Khristoforov, V. A. Mishchenko, A. V. Prokofiev, A. Y. Vinokhodov and V. A. Vodchits, "EUV sources using Xe and Sn discharge plasmas", J. Phys. D: Appl. Phys., Vol. 37, No. 23, pp.3254-3265 (2004)

[7] M. A. Klosner and W. T. Silfcast, "High-temperature lihium metal-vapor capillary discharge extreme-ultravioletsource at 13.5 nm", Appl. Opt., Vol. 39, No. 21, pp.3678-3682 (2000)

[8] M. A. Klosner and W. T. Silfcast, "Intense xenon capillary discharge extreme-ultraviolet source in the 10-16-nm-wavelength region", Opt. Lett., Vol. 23, No. 20, pp.1609-1611 (1998)

[9] M. A. Kolsner, H. A. Bender, W. T. Silfvast and J. J. Rocca, "Intense plasma discharge source at 13.5nm for extreme-ultraviolet lithography", Opt. Lett. Vol. 22, Issue 1, pp.34-36 (1997)

[10] E. R. Kieft, J. J. A. M. van der Mullen, G. M. W. Kroesen and V. Banine, "Time-resolved pinhole camera imaging and extreme-ultraviolet spectrometry on a holow cahode discharge in xenon", Phys. Rev E, Vol. 68, 056403 (2003)

[11] E. R. Kieft, J. J. A. M. van der Mullen, G. M. W. Kroesen and V. Banine and K. N. Koshelev, "Characterization of a vacuum-arc discharge in tin vapor using time-resolved plasma imaging and extreme-ultraviolet spectrometry", Phys. Rev E, Vol. 71, 026409 (2005)

MHD control of capillary Z-pinch discharge by using a triangular current pulse for lasing a recombination soft X-ray laser

Y. Sakai*, S. Takahashi*, T. Hosokai*, M. Watanabe*, G. Kim** and E. Hotta*

*Tokyo Institute of Technology, Nagatsuta, Midoriku, Yokohama, Kanagawa, 226-8502 Japan

* *Seoul National University, Seoul 151-744, Korea.

ABSTRACT

The capillary discharge soft X-ray laser is a promising scheme with its long plasma of about a few 10s cm in which the radiation is efficiently amplified. In expansion cooling phase of pinched H-like N plasma, it is possible to realize a recombination soft X-ray laser amplification at a wavelength of 13.4 nm by utilizing the population inversion between the principal quantum number $n=2$ and 3. In this collisional recombination scheme, rapid cooling of non-equilibrium plasma is necessary. To realize a rapid cooling of the plasma, it is effective to decrease the discharge current rapidly in order to reduce the magnetic pressure and the additional heating of the plasma as quickly as possible. In this study, shaping of discharge current waveform was done by using a transmission line and its effects on expanding plasma dynamics were investigated through MHD calculation and the framing photographs experimentally taken by using a high speed camera.

I. Introduction

A soft X-ray laser which has the high photon energy shows a strong interaction with matter in a molecular and an atomic level. It is strongly expected to be used in elucidation of solid state physics, nanotechnology and life science. However, it is difficult to realize lasing of a soft X-ray laser, because the pumping power required to amplify a collisional excitation soft X-ray laser is inversely proportional to its wavelength and thus it becomes huge. There has been a great advance owing to the recent progress in pulsed power technology. In 1985, using an ultra short pulsed laser for collisional or recombination excitation, lasing of a soft X-ray laser at a wavelength of around 20 nm has been demonstrated in Lawrence Livermore Laboratory and Princeton Plasma Physics Laboratory, respectively.[1, 2]

In 1994, utilizing a fast capillary Z-pinch discharge to generate a plasma column efficiently, lasing of a Ne-like Ar soft X-ray laser at a wavelength of 46.9 nm was demonstrated by J. J. Rocca et al.[3] In 2001, suppressing the growth of MHD instability by use of a pre-discharge, lasing of a Ne-like Ar laser was reproducibly observed.[4] Moreover, amplification of Ne-like Ar laser with higher coherence was realized using a 45 cm long capillary[5] and after then

demonstration of realizing a capillary discharge soft X-ray laser was successfully reported by several groups worldwide, which leads to improvement of technical bases for capillary discharge scheme.

In this study, we investigate a possibility of lasing the H-like N Balmer α recombination soft X-ray laser at a wavelength of 13.39 nm in anticipation of realizing a shorter wavelength laser pumped by capillary discharge scheme. The wavelength of 13.39 nm is in an extreme ultraviolet (EUV) range so that a Mo/Si multi layer mirror can be used, which will lead to wider application of capillary discharge soft X-ray laser.

As shown in Fig. 1, lasing of a H-like N recombination soft X-ray laser is considered to be
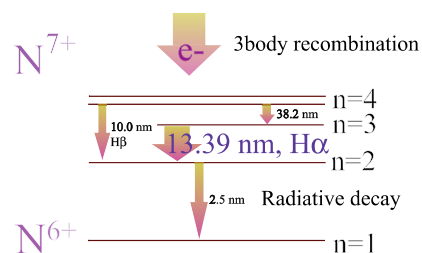
Fig. 1. Balmar α line of H-like N

possible using the population inversion between principal quantum number *n*=2 and 3 generated by three body recombination in rapidly cooled plasma after the generation of NVIII in the maximum pinch phase. For fast capillary discharge scheme, hot and dense plasma column is generated by implosion of current sheet initiated at the surface of the capillary wall toward the capillary axis. After the maximum pinch, a plasma column expands and an electron temperature is rapidly cooled down in several ns. Utilizing these pinch dynamics, it is possible to obtain a small signal gain of over 1 cm^{-1} according to MHD calculation results.[6] Fast decay of discharge current after the maximum pinch instant causes the rapid decrease of the magnetic pressure on the pinched plasma and of the additional Joule heating that possibly leads to the increase of the laser gain. In this paper, rapid cooling of the pinched plasma is attempted by pulse waveform shaping. At first, effects of obtainable current waveform on expansion dynamics were investigated through an MHD calculation. Then, rapid radial plasma expansion was observed experimentally by using a high speed camera in order to validate the MHD calculation results.

II. Experimental set-up

In order to ionize a nitrogen ion up to NVIII in only several ns, it is required to generate a hot and dense plasma with electron temperature of about 150 eV and electron number density of about 1×10^{20} cm^{-3}. Assuming that MHD equilibrium is established at the maximum pinch instant, current amplitude of over 50 kA is necessary to generate such a hot and dense pinched plasma[7]. In addition, a pulsed current with short decay time is necessary to cause a rapid cooling of the plasma. Moreover, pulsed current with high rise time is essential to generate highly-uniform plasma with good reproducibility. The discharge system mainly consists of a water capacitor charging section and a capillary discharge section as shown in Fig. 2. The water capacitor charging system consists of a 2-stage LC inversion generator, a 2:54 pulsed transformer and a 3 nF coaxial water capacitor. Adoption of a pulsed transformer in combination with a LC inversion generator enables to use only one gap switch in the circuit for charging a water capacitor up to about 0.5 MV. Energy transfer efficiency from an LC inversion generator to a water capacitor is about 50 %, which is a few times higher than that obtained in the case of a conventional Marx generator.

The discharge section consists of a relatively low inductance gap switch, a transmission line and a
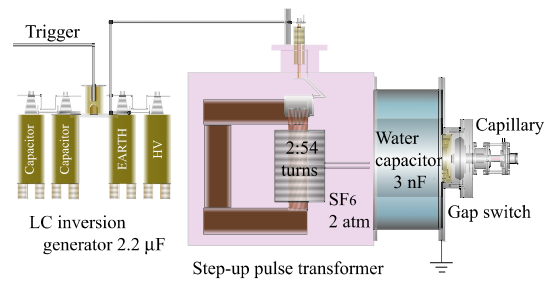
Fig. 2. Pulsed power system

capillary load. Fig. 3 shows a schematic diagram of the discharge section with the gap switch and the capillary. The gap switch is pressurized with SF$_6$ to decrease a gap distance to about 3 cm. Furthermore, several insulating barriers are used to prevent the surface discharge in the gap switch and the capillary section. Resulting inductances of the gap switch and the capillary section are about 75 nH and 50 nH, respectively. A water transmission line is inserted between the gap switch and the capillary as shown in Fig.4. Shaping of current waveform was done by changing the length of the transmission line. Thus, it is possible to control a delay time between a forward and a reflected voltage wave. It enables two kinds of voltage waves to be superimposed or separated, which leads to the shaping of current waveform. Obtainable current waveforms were calculated through a wave equation for a distributed constant circuit. Waveforms shown in Fig. 5 are the calculation results for a transmission line with length of 25-80 cm. The longer the transmission line is, the longer the pulse width of a current waveform becomes. For the transmission line of 25-40 cm, triangular current waveform with higher peak current is generated, because a forward wave and a reflected wave are superposed in phase at the center of the pulse. In this case, when the charging voltage of water capacitor is about 300 kV, the triangular current wave with amplitude of 70 kA and pulse width of about 60-80 ns is efficiently generated. In this paper, a transmission line with a line length of 25 or 40 cm and a surge impedance of about 3 Ω was used.

In experiment, a capillary plasma was pre-ionized to generate an axially uniform plasma in pinch phase by utilizing an RC discharge with an initial current amplitude of 20 A and a decay time constant of 3 μs. An expanding plasma after the maximum pinch was observed from the axial end of the capillary by using a high speed camera, PI-MAX System of Princeton Instruments, with gate time of 2 ns.

III. Effects of current waveform shaping on MHD dynamics in calculation

To investigate the effects of current waveform shaping on rapid expansion cooling of the pinched plasma, 1 dimensional (1D) MHD calculation has been done.[8] Calculated Current density, Magnetic flux, axial velocity in the Lagrangian cells, electron temperature and electron density for the triangular current pulse with pulse width of about 60 ns and for a sinusoidal current with half cycle of 100 ns are shown in Fig. 6 respectively. In Fig. 6, the start time of a current flow is set to 0. The maximum pinch occurs at 40 ns in both cases, where current density and Magnetic flux is nearly the same value. The magnetic flux at the maximum pinch instant to confine the plasma column are about 35 T. And, current density profiles before the maximum pinch instant have a similar trend in both cases. Consequently, the energies dissipated in the plasma before the maximum pinch are nearly the same in both cases, so that the maximum electron temperature and the maximum electron number density reach about 140 eV and 1.4×10^{20} cm^{-3} respectively in both cases, which is required value in order to ionize nitrogen ion up to NVIII. After the maximum pinch in the case of using a sinusoidal current, a peak current amplitude is maintained for about 10 ns. On the other hand, in the case of using a triangular current, the current and current density

decreases rapidly after the maximum pinch. As a result, there is discrepancy of expansion velocity between two cases. In the case of sinusoidal one, maximum expansion velocity is 1.0×10^5 m/s and plasma tends to implode again. However, in the case of triangular one, maximum expansion velocity is increased to 1.5×10^5 m/s. This is ascribed to the fast reduction of magnetic pressure used for plasma confinement which is caused by the rapid decay of a discharge current. Moreover, rapid current decay reduces additional Joule heating of plasma after the maximum pinch. These effects lead to the rapid cooling of the plasma column, which is necessary to generate the non-equilibrium population inversion for lasing.

IV. Experimental results

The discharge current waveforms experimentally obtained are shown in Fig. 7. A solid and a dashed line indicate the discharge current waveforms obtained by using a low inductance load of 125 nH and by using a relatively high inductance load of 250 nH, respectively. In both cases, charging voltage of the water capacitor is 100 kV. Reduction of load inductance from 250 nH to 125 nH reduces the half cycle time from 110 ns to 80 ns and the resulting current amplitude is increased by nearly 1.5 times.

Discharge current obtained by inserting a transmission line of 25 cm long with surge impedance of 3 Ω between the gap switch and the capillary load is shown in Fig. 8. As a result, a sinusoidal current waveform is shaped to a triangular one with a pulse width of about 60 ns and the amplitude is increased 1.5 times higher than that of current obtained using a load of 125 nH, which coincides with the calculation results.
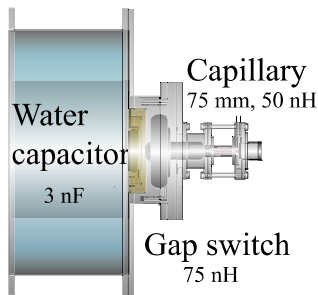
Fig. 3. Discharge section consisted of a gap switch and a capillary.
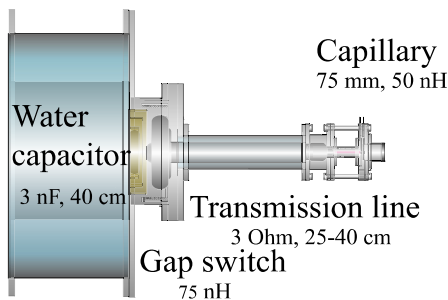
Fig. 4. Discharge section with transmission line
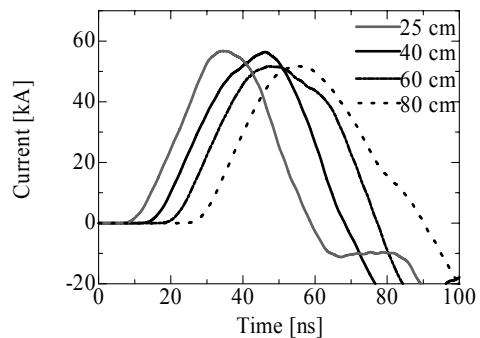
Fig. 5. Calculated discharge current waveform with transmission line length as parameter
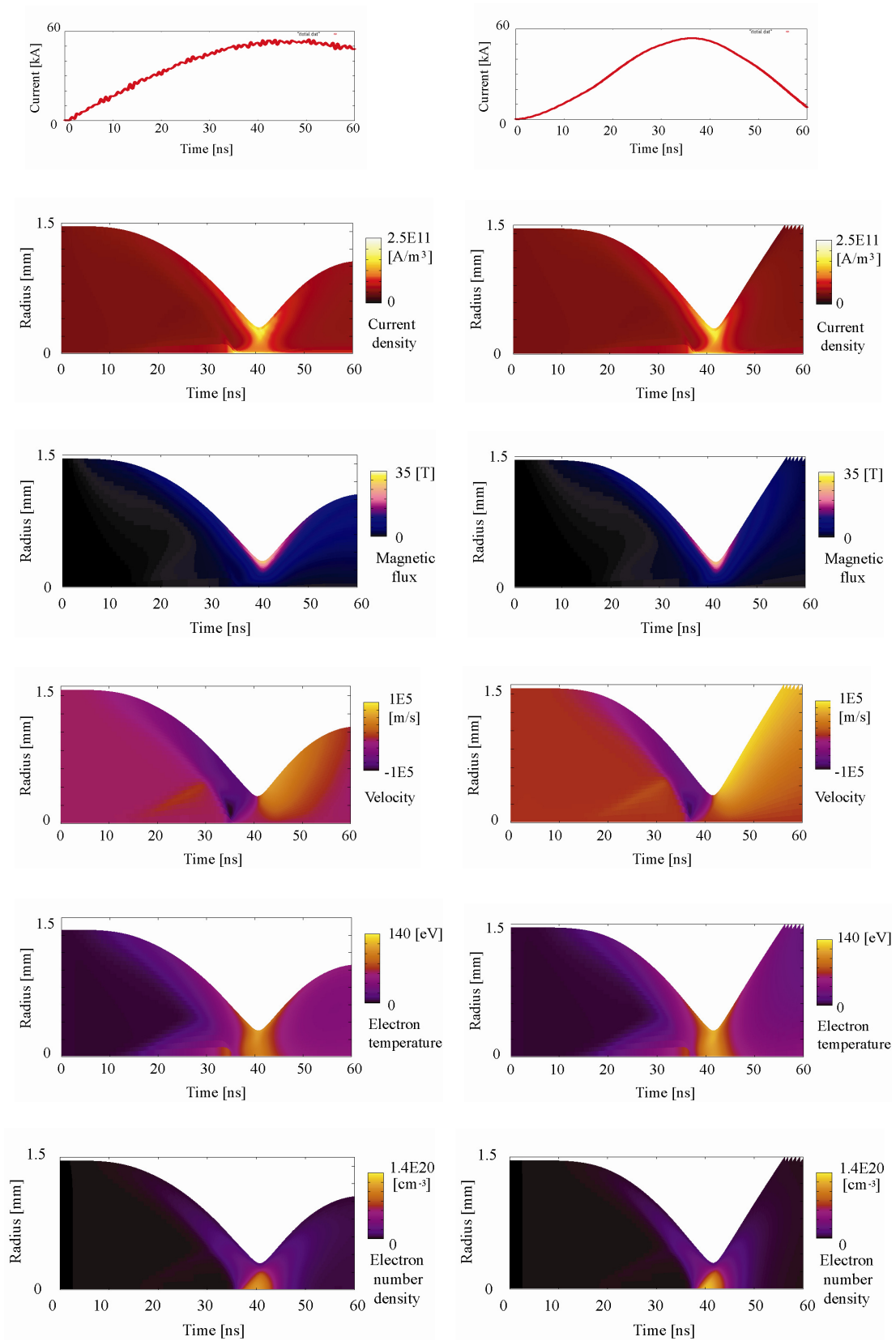
Fig. 6. Effect of current waveforms on expansion phase of plasma in 1D MHD calculation
Left : For sinusoidal current, Right : For triangular current
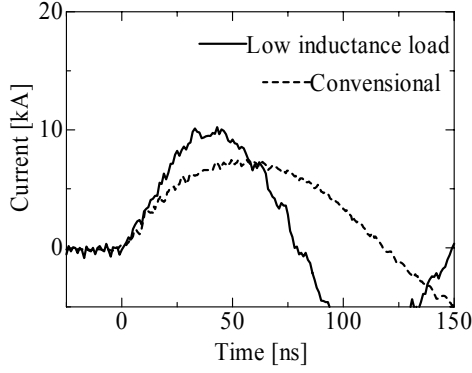
Fig. 7. Current waveform obtained by using low inductance discharge section
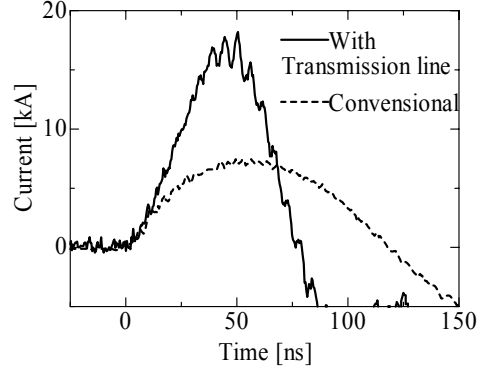
Fig. 8. Current waveform obtained by using a transmission line

To verify the effect of MHD control by current waveform shaping on plasma dynamics, expansion plasma images were taken by using a high speed camera and the resulted framing photographs are shown in Fig. 9. Fig. 10 shows the MHD calculation results of electron temperature, electron number density and Lagrangian cell position being based on experimental condition such as discharge current waveform and initial gas pressure. The discharge current used in the experiment was triangular one with amplitude of 30 kA and a pulse width of about 80 ns which is generated by using a transmission line of 40 cm. The inner radius of capillary was 1.5 mm and an initial NII pressure was 266 Pa approximately. In Fig. 9 and 10, the origin is set to the time when plasma starts to expand. In the experiment, plasma column with 1.5 mm radius is compressed to the maximum pinched plasma column with radius of about 200 μm. After that, plasma starts to expand and reaches the capillary inner wall in about 15 ns. Then, at t=20 ns, ring shaped radiation image is observed due to the strong emission from the ablated capillary inner wall material. Assuming that the plasma, initially composed of NII with uniform pressure of 266 Pa, is compressed to a plasma column with radius of about 200 μm, in which NVI is dominant, electron number density of the maximum pinched plasma is evaluated as

$$N_p = N_e + N_i \approx 2(z+1) \times \frac{r_0^{\,2}}{r_p^{\,2}} \times N_0 = 2.0 \times 10^{19} \quad [\text{cm}^{-3}],$$

where N_0 is the initial number density of nitrogen molecule, N_e is the electron number density, N_p is the electron number density of the maximum pinched plasma, r_0 is the inner diameter of the capillary and the r_p is the radius of the maximum pinched plasma column. Assuming that MHD equilibrium is established at the instant of the maximum pinch, electron temperature is evaluated to be about 150 eV by using following Bennet`s relation.

$$T_e = \frac{\mu_0}{8\pi^2 r_p^{\,2} N_p k} I^2$$

Here, T_e is the electron temperature, μ_0 is permeability and k is the Boltzmann`s constant. After the maximum pinch, if it is supposed that expansion cooling progresses isentropically, adiabatic relation is given by,

$$N_{p,\text{expansion}} / N_{p,\text{pich}} = \left(T_{\text{expansion}} / T_{\text{pinch}}\right)^{\frac{1}{\gamma-1}}.$$

Where specific heat ratio $\gamma = 5/3$ is used. As a consequence, the pinched plasma with an electron temperature of about 150 eV is rapidly cooled down to below 50 eV in approximately 10 ns, which is suitable for recombination pumping of H-like N laser. Furthermore, during the plasma expansion, it was confirmed that the plasma keeps its axial symmetry and relatively expands toward a capillary inner wall uniformly. These experimental results are considerably similar to the 1D MHD calculation results so that it is possible to estimate the dynamics of expansion plasma after the maximum pinch. Thus, the expanding plasma is considered to have a radially uniform density profiles that is similar to the MHD calculation results. In such a uniform plasma column, it is difficult to anticipate the effect of wave guiding for efficient amplification of the X-ray without divergence. However, it is still possible to amplify the soft X-ray radiation in the plasma column with radially uniform electron density profile.
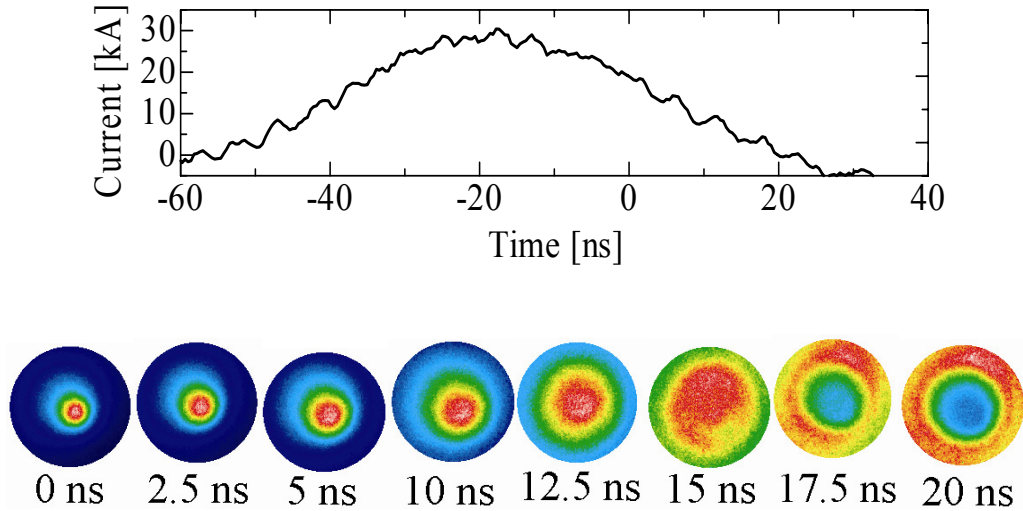
Fig. 9. Framing photographs of expanding plasma. (Plasma begins to expand at 0 ns.)
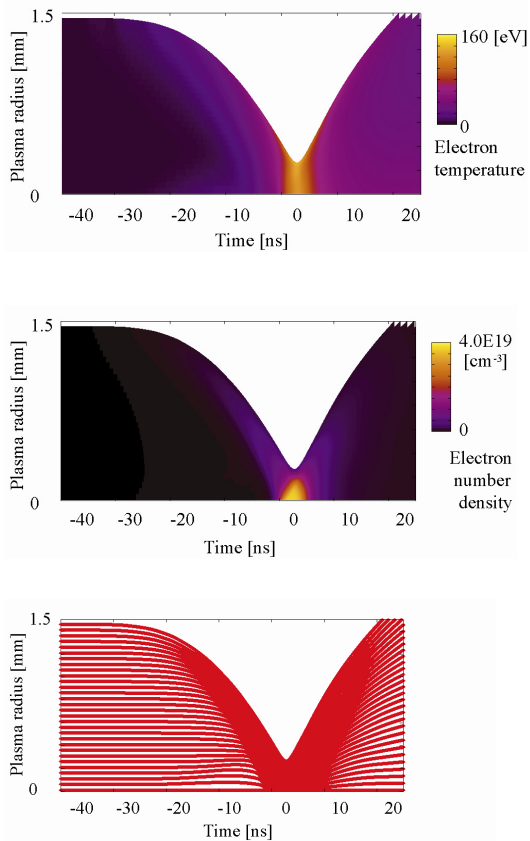
Fig. 10. MHD calculation results by using a
current waveform shown in Fig. 9.
Upper: electron temperature, middle: electron
number density, lower: Lagrangian cell position

In conclusion, using the triangular current pulse with rapid decay after the maximum pinch instant, it is possible to increase the expansion cooling rate of the plasma and the gain for recombination laser. However, for realizing a lasing at shorter wavelength, it is necessary to increase the discharge current amplitude, which will lead to the increase of the amount of ablated plasma from a capillary inner wall. It will result in larger discrepancy between the experimental and the calculation results. Actually, in this experiment, the maximum pinch time is delayed by about a several ns from that obtained in 1D MHD calculation. Increase of the amount of ablated material entered into plasma causes a decrease of an electron temperature at the maximum pinch instant so that the current amplitude required to ionize nitrogen ions up to NVIII will be higher than that estimated by 1D MHD calculation. However, as far as dynamics of expansion plasma after the maximum pinch is concerned, it is expected that plasma expands symmetrically without electron density gradient in which amplification of soft X-ray radiation is possible. The above mentioned results show that it is possible to control the dynamics of the expanding plasma by shaping the current waveform.

V. Conclusion

Control of expansion of plasma after the maximum pinch was attempted by shaping current waveform for realizing a capillary discharge recombination soft X-ray laser. In 1D MHD calculation the triangular current pulse, which rapidly decays after the maximum pinch, is shown to be effective to increase the cooling rate of the plasma. Installing a transmission line between a gap switch and capillary

load, it was demonstrated to generate a triangular pulse with pulse width of about 60-80 ns. In the experiment, using a high speed camera, rapid radial expansion of pinched plasma in 10 ns was observed, which is similar to the MHD calculation result. By utilizing such a rapidly expansion plasma, it is possible to increase cooling rate of the pinched plasma after the maximum pinch where highly ionized NVIII is expected to be generated, which leads to realization of population inversion for H-like N recombination laser before the thermal equilibrium is established.

References

1) D. L. Matthews et al. : "Demonstration of a Soft X-Ray Amplifier", Phys. Rev. Lett. Vol. **54**, 110-113 (1985).

2) S. Suckewer, C. H. Skinner, H. Milchberg, C. Keane, and D. Voorhees : "Amplification of stimulated soft x-ray emission in a confined plasma column", Phys. Rev. Lett. **55**, 1753-1756(1985).

3) J. J. Rocca, V. Shlyaptsev, F. G. Tomasel, O. D. Cortazar, D. Hartshorn andJ. L. A. Chilla : "Demonstration of a Discharge Pumped Table-Top Soft X-ray Laser", Phys. Rev. Lett., **73**, 2192-2195 (1994).

4) G. Niimi, Y. Hayashi, N. Sakamoto, M. Nakajima, A. Okino, M. Watanabe, K. Horioka, and E. Hotta : "Development and Characterization of a Low Current Capillary Discharge for X-ray Laser Studies", IEEE Trans. Plasma Sci., **30**, 616-621 (2001).

5) G. Tomassetti, A. Ritucci, A. Reale, L. Palladino, L. Reale, S. V. Kukhlevsky, F. Flora, L. Mezi, A. Faenov, T. Pikuz and A. Gaudieri : "Toward a full optimization of a highly saturated soft-X-ray laser beam produced in extremely long capillary discharge amplifiers", Optics Communications, 231, 403-411 (2004).

6) P. Vrba, M. Vrbova, N.Dezhda, A. Bobrova and P. V. Sasorov : "Modeling of a nitrogen x-ray laser pumped by capillary discharge", Central European Journal of Physics, 3, 564-580 (2005)

7) Yusuke Sakai, Takanori Komatsu, Yifan Xiao, Inho Song, Gota Niimi, Masato Watanabe, Akitoshi Okino and Eiki Hotta : "Soft X-ray radiation from nitrogen z-pinch plasma produced by capillary discharge", IEEJ Transactions on Fundamentals and Materials, **11**, 675-680 (2007).

8) Y. Sakai, S. Takahashi, T. Hosokai, M. Watanabe, A. Okino and E. Hotta : "The possibility of a capillary discharge soft X-ray laser with shorter wavelength by utilizing a recombination scheme", ELX., P2-203 [714], ICPP2008 : International Congress on Plasma Physics 2008. September 8-12 (2009).

OPTICAL EMISSION CHARACTERISTICS OF ATMOSPHERIC TRANSIENT GLOW DISCHARGES GENERATED BY DOUBLE PULSED VOLTAGES

Jun Kikuchi, Koichi Igarashi, Naoaki Yoshida, Shinji Ibuka, and Shozo Ishii

Department of Electrical and electronic Engineering,
Tokyo Institute of Technology,
2-12-1 S3-9 Ookayama, Meguro-ku, Tokyo 152-8550, Japan.

ABSTRACT

Atmospheric transient glow discharges, suppressing the glow-to-arc transition, were obtained using fast high voltage pulse-trains generated using a nonlinear transmission line. To examine the effect of successive pulse-train on the discharge development, we developed the double-pulsed voltage generator, in which the pulse interval was variable. Spatially and temporally solved optical emission spectroscopy as well as voltage and current measurements were conducted to characterize the discharges. There appeared significant differences between the first and second pulsed discharges. With increasing the pulse interval, the N_2 line intensity and the breakdown voltage for the second pulsed discharge increased. The results show that the double-pulsed voltage technique is effective to investigate the preceding discharge effect on the following one.

I. Introduction

Atmospheric glow discharges, which have the features of operation with a simple and low cost system, are employed in various applications such as destruction of toxic compounds, detection of trace contaminants, depositing of films, surface process [1], [2]. There, however, is a serious drawback of the glow-to-arc transition in the glow discharges under atmospheric pressure. To make atmospheric glow discharges stable, one has to pay attention to the discharge electrodes, the applying power, and feeding gas control. Recently, microplasmas, with the size of $10 - 1000$ μm, are used to generate the stable atmospheric glow discharges powered by direct current (DC) voltages [3], [4]. The DC voltage operations cannot feed high energy and power to the discharges because the amplitude of current is limited within a few mA to avoid the glow-to-arc transition.

If the applied voltage is made zero before the glow-to-arc transition, the transient atmospheric glow discharge develops. The pulsed voltage operation makes the high instantaneous power injection possible. Adjusting the duty ratio of pulsed voltages, one can control the particle number densities of electrons, ions or radicals to be optimum value for the applications. It was reported that radical densities depend on instantaneous input power [5]. Pulsed voltages having a short pulse width of 10 ns can generate high density plasmas with a low power consumption and high efficiency [6]. We previously obtained the atmospheric transient glow discharge between the nozzle and metal plate electrodes with a miniature gas flow using the fast high-voltage pulse-train generated with a nonlinear transmission line [7], [8]. The pulsed voltages with a repetition frequency of the order of MHz are necessary for the stabile glow discharges. Utilizing the fast high voltage pulse-train with a repetition frequency of 20 MHz, we realized stable generation of the transient glow discharge with high power-input in any configurations of the cathode.

The stabilization mechanism of the transient glow discharges with the fast high voltage pulse-train has not been understood yet. In this study, we discussed the evolution of the transient atmospheric glow discharges by measuring gap voltages and discharge currents and conducting a spatially and temporally solved optical emission spectroscopy for the discharges, where their characteristics were affected by the pulse intervals. Owing to the difficulty of controlling the pulse interval of the pulse-train obtained by a nonlinear transmission line, we developed a double pulsed voltage generator, which was composed of two Blumelein type pulse forming networks, with variable pulse intervals

He

Nozzle anode

600 μm

300 μm

Plate cathode

200 μm
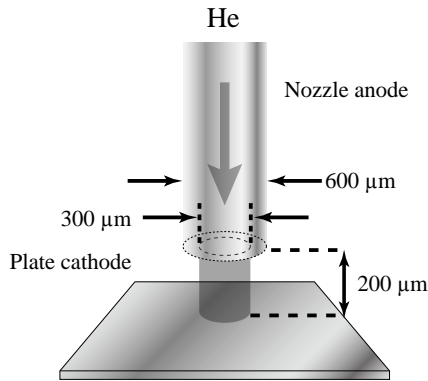
Figure 1 The nozzle anode and the plate cathode.

pulse interval

frequency

pulse charger

PFN 1

PFN 2

LOAD

function generator

Figure 2 The double-pulsed voltages generator.

Figure 3 The waveform of double-pulsed voltages
in the case of matching PFNs and the load.

II. Experimental setup

Figure 1 shows a nozzle-to-plate electrode system for the transient glow microdischarges powered by double-pulsed voltages. These electrodes are made of stainless steel. The inner and outer diameters of the nozzle anode are 300 μm and 600 μm respectively. The surface of the plate cathode was polished with an abrasive compound to suppress the glow to arc transition. Both the electrodes were placed on micro positioning stages, which enabled them to move independently. The separation between the nozzle anode and the plate cathode was 200 μm. The helium gas flow rate out of the nozzle anode was regulated with a mass flow controller, which adjusted the maximum flow rate of 500 sccm.

The double pulsed voltages consist of two successive rectangular high-voltage pulses, which are generated using pulse forming networks (PFNs). We previously reported a stable transient glow discharge in air powered by the fast high-voltage pulse train generated using a nonlinear transmission line [8]. In this method, however, it was difficult to control the pulse width and the pulse interval. We developed a double pulsed high-voltage generator in which the pulse width and the pulse interval were varied easily. The pulse generator has two PFNs, which are connected to the nozzle anode in parallel via semiconductor diodes as shown in Figure 2.

The PFN is a Blumlein type, of which output voltages are equal to the charging voltage. The Blumlein type PFNs were charged up to 2.0 kV in this experiment. The PFNs were designed to have the characteristic impedance of 50 Ω and the pulse width of 600 ns. We adjusted the switching time of the PFNs with a function generator to vary the pulse interval in the range of 0.1–100 μs. The repetition rate of a set of double-pulsed voltages, of which typical waveform for the matched load of 50 Ω is shown in Figure 3, was 100 - 200 Hz.
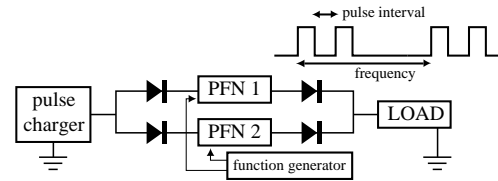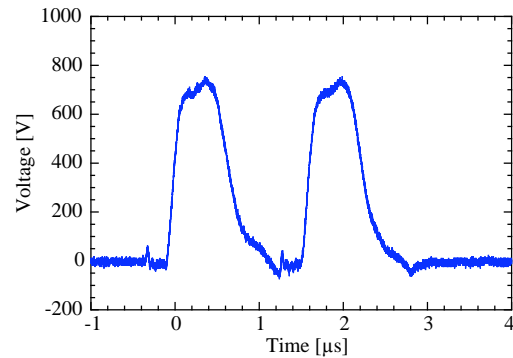
We observed temporal and spatial behavior of the discharges using an image intensified charge-coupled device (ICCD) camera and conducted time and space resolved optical emission spectroscopy (OES). For the OES, we used two optical systems with convex lenses or a concave mirror to magnify the discharge area because the size of atmospheric transient glow discharges is typically less than 1 mm [9], [10]. A pair of convex lenses provides the magnified image of the discharge on the entrance slit of a monochromator with a photomultiplier. Although the measurement system realizes high temporal resolution, the photomultiplier signals contain high frequency random components. The signals were smoothed using the multiple time averaging function of an oscilloscope.

The convex lens's system has a drawback of chromatic aberration, which causes that the image of discharges is in focus for a certain wavelength and out of focus for other wavelengths. Consequently, one has to always adjust the separation between the discharge and the convex lens for a given wavelength to establish the accurate measurement. To avoid the
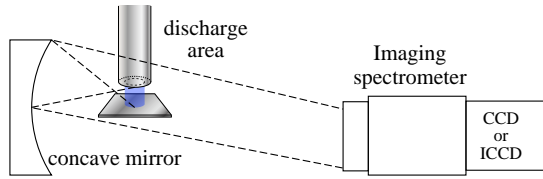
Figure 4 Experimental setup for time and space
resolved emission spectroscopy.

Figure 5 Temporal behaivors of discharge voltage,
current and spectral line intensities in the
discharges with double-pulsed voltages.

messy adjustment of the lens position, we used the optical system with the concave mirror, an imaging spectrometer, and the ICCD camera as shown in Figure 4. The concave mirror magnifies the image of discharges with no chromatic effects. The magnified image was focused on the entrance slit of an imaging spectrometer (SOLAR TII model SL100M), which provide a spectrally-resolved image of the discharge and has a focal length of 100 mm and a grating of 400 lines mm^{-1}. The image through the spectrometer was captured by the ICCD camera, which was mounted on the spectrometer and established spatial distribution of the emission spectra with a highly resolved time scale. The concave mirror with a focal length of 50.8 mm magnified the image of discharges by five times. A part of the reflected light ray was shaded by the discharge electrodes. Spherical aberrations occur with the mirror tilted, however, we can neglect the aberrations appearing in a small tilted angle. The reflected light was focused on the entrance slit of the imaging spectrometer. The spectrum was measured in the range of 360 – 1100 nm and the spectral resolution was < 1 nm for a CCD detector with a pixel size of 26 μm. The spectrally-resolved image was captured by the ICCD camera (Andor Technology model DH734 18U-03) with the minimum gate width of 2 ns. The ICCD had 1024 by 1024 pixels, which had 13 μm of the effective pixel size, corresponding to the spectral resolution of less than 0.5 nm.

III. Results and Discussions
A. Characteristics of the atmospheric transient glow discharges

We conducted the time-resolved optical emission spectroscopy on the atmospheric transient glow discharges powered by double-pulsed voltages. Figure 5 shows temporal changes of the discharge current, the gap voltage, and the spectral line intensities of He, N_2, and N_2^+, a 587 nm line of helium atoms, a 337 nm emission line of the second positive band of N_2 and 391 nm line of the first
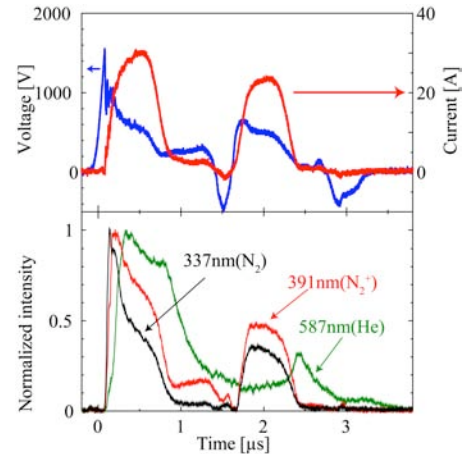
negative band of N_2^+. A pulse interval of double-pulsed voltages was set to be 1 μs. Since the gap voltages for both the pulses appeared to be constant at 500 V after the breakdown, the transient glow discharges developed. The transient steep voltage drop at breakdown, which appeared for the first pulse, was not observed for the second pulse. The negative spikes of the gap voltage were originated due to the impedance mismatching of the PFNs with the discharge load. The second pulsed discharge was affected by the first one, which created ions, electrons, and excited species. They remained at the second pulse phase depending on their life times. Because these particles assisted the discharge evolution, the breakdown process for the second pulse was different to that for the first pulse.

We observed spectral lines that were affected by the discharge development, at the first discharge, the spectral intensity of 337 nm (N_2) increased rapidly after the beginning of breakdown, followed by its gradual decrease. When the gap voltage fell to zero, its intensity became weak. Therefore, the N_2 emission is attributed to the direct excitation by collision of energetic electrons accelerated with an electric field. The intensity of 391 nm line (N_2^+) changed as similar to that of N_2 line, but decayed more slowly. It was reported that the excitation process of N_2^+ was complicated and influenced by metastable helium atoms [11]. In comparison with the intensity of nitrogen lines, that of helium atomic line of 587 nm changed differently. It increased as the discharge current started to rise for the first pulse; then, it decreased more slowly than that of the nitrogen lines.
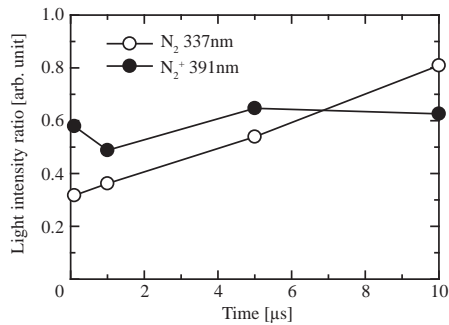
Figure 6 Change in spectral intensities for
pulse interval.

Figure 7 Dependence of the breakdown voltage at
the second pulse on the pulse interval.

Its emission lasted for more than 1 μs after the decay of the discharge current. The helium line emission at the recombination stage with zero applying voltage is originated from the helium in the metastable state with a long lifetime, because the direct excitation by electron collision is not expected.

A significant difference between nitrogen and helium line emissions appeared at the beginning of the first pulse. The helium line emission intensity developed with synchronizing the discharge current, while the nitrogen line emissions reached their peaks immediately after the breakdown and decayed rapidly. This temporal change appeared markedly in the N_2 emission (337 nm). Its intensity decayed to a half of its peak intensity and lasted for 0.3 μs, in which the gap voltage stayed at approximately 500 V and decayed rapidly after then. The temporal change of the N_2 emission coincides with that of the gap voltage. The helium atomic line emission started to rise when the breakdown occurred. The increasing speed of helium emission intensity changed at approximately 120 ns after the breakdown, in which the gap voltage decayed to the discharge-sustaining voltage. The increase of the slope corresponded with the shifts of the excitation and ionization processes. In general, a DC atmospheric glow discharge under helium atmosphere shows not only a strong emission of helium atomic lines but also emissions of N_2 and N_2^+ of impurities [3], [12]. So, we expected that the pulsed discharge exhibited the property of an atmospheric glow discharge after at 120 ns after the discharge began.

Residual active species created at the first discharge affected the discharge for the second pulse. The effect appeared in the temporal change of the spectral line intensities of N_2 and N_2^+, which increased and decayed rapidly at the breakdown for the first pulse, while those for the second pulsed discharges were synchronized with the discharge
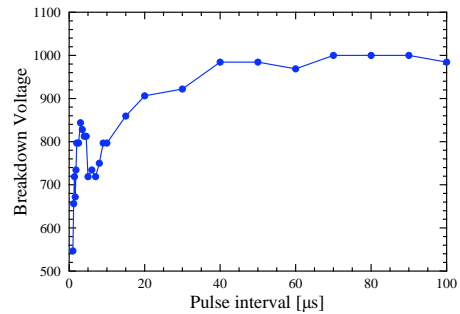
current. On the other hand, the helium atomic line intensity did not show the temporal change as that of the discharge current for the second pulse. It increased only slightly and had its peak after the discharge current became zero because the radicals and metastable species with a long lifetime affected the emission processes.

The effect of preceding discharges was also characterized by changing the pulse interval. When it was increased the ratios of the peak intensity of the nitrogen line emission for the second pulse to that of the first one change as shown in Figure 6. With the pulse interval increased, the ratio of the N_2 line emission increased from 0.3 to 0.8 for the interval of 10 μs. As far as the nitrogen breakdown is concerned, the result suggests that the discharge evolution for the second pulse was similar to that for the first pulse. If the pulse interval became long, the number densities of the nitrogen ions and the excited nitrogen molecules decreased. The N_2^+ line emission, however, shows no significant change in the ratio. The line is related to the processes such as Penning ionization by metastable helium atoms and charge transfer from helium molecular ions to nitrogen molecules. Therefore, the N_2^+ emission is less affected by the discharge than N_2 emission.

The breakdown voltage for the second pulse depends on the pulse interval as shown in Figure 7. It was saturated and stayed at 1000 V for the pulse interval of more than 40 μs, in which the ions and excited species created at the preceding discharge were expected to decay and be lost. However, the critical pulse interval of 40 μs was longer than the residence time, a few microseconds in this experimental condition, of the miniature helium gas flow between the electrodes. Therefore, the radicals and metastable species with a long lifetime are expected to exist in the ambient air, which surrounds the helium gas flow. With increasing the pulse
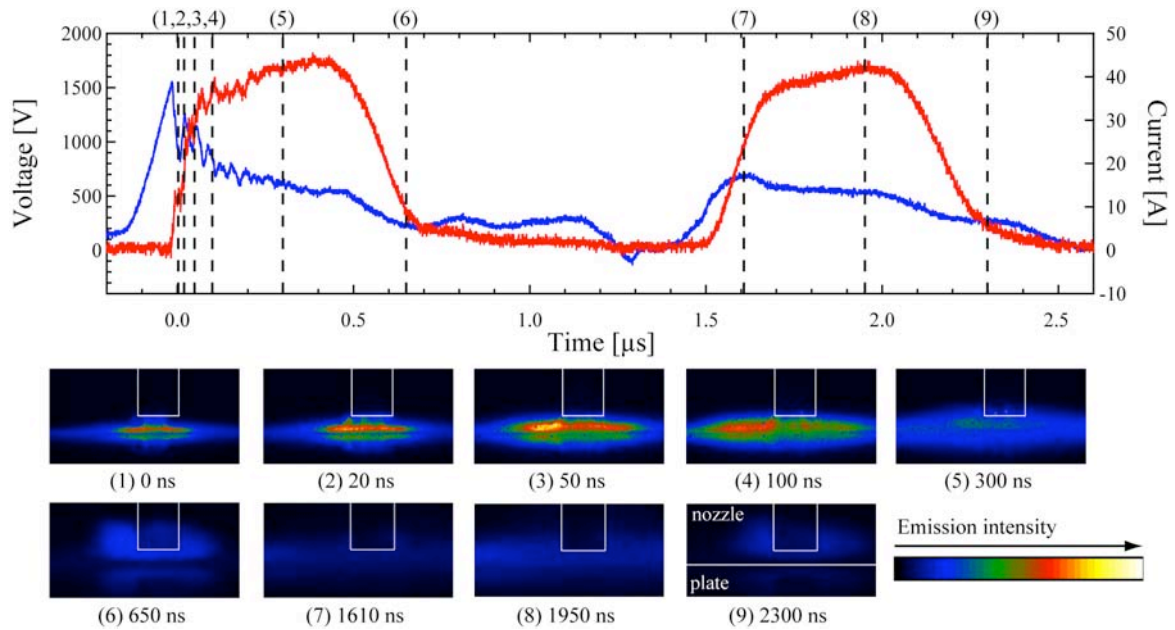
Figure 8 ICCD images of the transient glow discharge powered by double-pulsed voltage

interval, the breakdown voltages suddenly drop at the pulse interval of from 5 to 7 μs, which was about twice of the residential time of the helium miniature gas flow. Thereby, the helium gas flow seems to affect the discharge processes, however, more detailed discussion is necessary to analyze the development mechanism for the lowing of the breakdown voltage.

B. The evolution of the atmospheric transient glow discharge

The temporal and special developments of the transient glow discharges were observed using the ICCD camera with an exposure time of 10 ns. Figure 8 is a set of photographs of the discharges and the voltage and the current waveforms. The timing of the each frame is indicated in the waveforms. The intense light emission appeared and expanded in the radial direction in the frame (1)-(3) for the time of 0-50 ns, in which the spectral emission bands of N_2 or N_2^+ are main components as shown in Figure 5. The expansion of the light emission region ended at 100 ns. The line intensity of helium increased remarkably at 100-300 ns, in which that of nitrogen emission decayed in Figure 5. Consequently, the total light intensity became weak. In the frames of (7) and (8) for the second pulse, the light emission, which was mainly composed of the spectral lines of N_2 and N_2^+, was uniform and no local bright region was observed. Although the transient glow discharges were

generated for both the first and the second voltage pulses, the light emission characteristics were different.

The temporal and spatial changes of spectral line intensities were measured simultaneously using the imaging spectrometer and the ICCD camera. Figure 9 shows the temporal development of the spatial distribution of spectral intensities of N_2^+ line of 391 nm and Figure 10 shows that of He line of 587 nm. Due to the wavelength sensitivity of the imaging spectrometer (wavelength range of 360 – 1100 nm), the N_2 emission line (337 nm) cannot be measured. The exposure time of the ICCD was set to be 50 ns and the times for the data points in Figure 9 and 10 were selected to be close to the shuttering timing in Figure 8. When the discharge was initiated by the first pulsed voltage, the N_2^+ line intensity was intense and its intensity of the cathode side was more intense than that of the anode side. When the N_2^+ line intensity decreased, its spatial distribution became uniform. This situation last for the period of the second pulse as shown in Figure 9(b).

The spatial distribution of the He line intensity was almost similar to that of the N_2^+ line intensity. The intense emission at the cathode side lasted during the period of 100 – 450 ns. The spatial distribution of the He line intensity became uniform during the second pulsed voltage. For the second pulsed voltage, the discharge is affected by the first pulsed discharge significantly because residual particles such as ions,
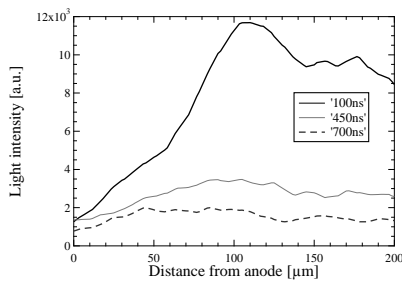
(a) The first pulsed discharge
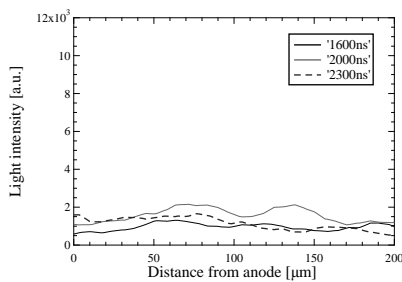
(b) The second pulsed discharge

Figure 9 Temporal and spatial changes in spectral intensities of N_2^+ (337 nm)
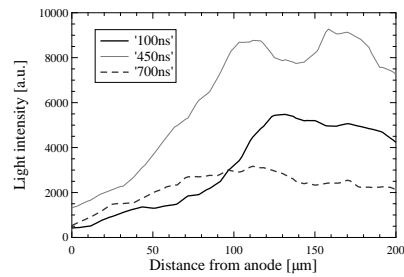
(a) The first pulsed discharge
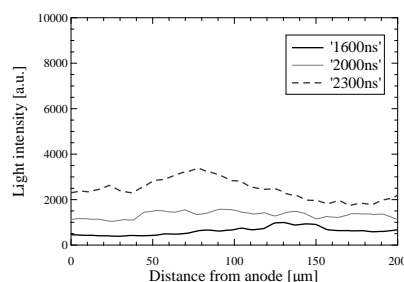
(b) The second pulsed discharge

Figure 10 Temporal and spatial change in spectral intensities of He (587 nm)

electrons, radicals, and metastable species contribute the gas breakdown processes. This is evident from the result of Figure 7 that shows the decrease of the breakdown voltage by the first pulsed discharge.

When repetitive pulsed voltages power the atmospheric transient glow discharges, the discharge characteristics depend on the pulse intervals. The successive discharge develops from the breakdown of neutral gases to the glow, if the pulse interval is sufficiently long. Consequently, the gap voltage is higher than that for the discharges with shorter pulse intervals, because the peak voltage corresponds to the breakdown one. One can control the plasma by varying the pulse intervals according to applications.

IV. Conclusion

We characterized the effect of the preceding discharge on the following one in the double-pulsed transient glow discharge, of which the pulse interval was varied to 100 µs. It was verified that there appeared the significant difference in visible light emission between the two discharges. The spatial distribution of the light emission for the second discharge was uniform. The pulse interval affects the development of the second discharge. The increase of the pulse interval changes the temporal development of the N_2 line intensity and raised the breakdown voltage of the second discharge. The N_2 line emission

and electrical characteristics are good measures for discussing the double-pulsed discharges. The residual particles such as radicals, negative ions, and metastable helium atoms, which were generated by the preceding pulsed discharge, are not examined fully yet. More detailed discussion on the effect on those particles is necessary to understand the discharge processes in the high repetition pulsed discharges.

References

1) K H Becker, K H Schoenbach and J G Eden, "Microplasma and applications", J. Phys. D: Appl. Phys, Vol. 39,pp.55-70 (2006).

2) J. Benedikt, K. Focke, A. Yanguas-Gil, and A. von Keudell, "Atmospheric pressure microplasma jet as a depositing tool", APPLIED PHYSICS LETTERS, Vol. 89, 25104 (2006).

3) T. Yokoyama, S. Hamada, S. Ibuka, K. Yasuoka and S. Ishii, "Atmospheric dc discharges with miniature gas flow as microplasma generation method", Journal of Physics, Vol. 38, pp.1684-1689, (2005).

4) David Staack, Bakhtier Farouk, Alexander Gutsol and Alexander Fridman, "DC normal glow discharges in atmospheric pressure atomic and molecular gases", Plasma Sources Sci. Technol., Vol. 17, 025013 (2008).

5) K H Becker, U Kogelschatz, K H Schoenbach

and R J Barker, "Non-Equilibrium Air Plasmas at Atmospheric Pressure", Institute of Physics Publishing (2005).

6) Michael A. Lieberman and Allan J. Lichtenberg, "Principles of Plasma Discharges and Materials Processing", WILEY INERSCIENCE (2005).

7) S. Ibuka, R. Mikami, F. Furuya, K. Ogura, K. Yasuoka and S. Ishii, "Generation of Atmospheric Pressure Transient Glow Discharge in Microgap Electrode with Nanosecond Pulsed Voltage", IEEJ Transactions on Fundamentals and Materials, Vol. 127, No. 7, pp. 411-416 (2007).

8) S. Ibuka, K. Harada, J. Kikuchi, K. Igarashi, and S. Ishii, "Application for carbon materials production with atmospheric transient glow discharge in microgap electrode", The Papers of Technical Meeting on Pulsed Power Technology, IEE Japan, PPT-07-39 pp.7-12 (2007). (in Japanease)

9) David Staack, Bakhtier Farouk, Alexander Gutsol and Alexander Fridman, "Spatially Resolved Temperature Measurements of Atmospheric-Pressure Normal Glow Microplasmas in Air", IEEE Trans. On Plasma Science, Vol. 35, No. 5, pp.1448-1455 (2007).

10) Qiang Wang, Ivanka Koleva, Vincent M Donnelly and Demetre J Economou, "Spatially resolved diagnostics of an atmospheric pressure direct current helium microplasma", J. Phys. D: Appl. Phys., Vol. 38, pp. 1690-1697 (2005).

11) P Zhang and U Kortshagen, "Two-dimensional numerical study of atmospheric pressure glows in helium with impurities", J. Phys. D: Appl. Phys., Vol. 39, pp. 153-163, (2006).

12) Francisco J. Andrade,* William C. Wetzel, George C.-Y. Chan, Michael R. Webb, Gerardo Gamez, Steven J. Ray and Gary M. Hieftje, "A new, versatile, direct-current helium atmospheric-pressure glow discharge", Journal of Analytical Atomic Spectrometry, Vol. 21, pp. 1175-1184, (2006).

DEVELOPMENT OF THE ELECTRON SPECTROMETER FOR MEASUREING THE ENEGETIC ELECTRON FROM LFEX LASER IN FIREX-I PROJECT

T. Ozaki, M. Koga[1], H. Shiraga[1], H. Azechi[1] and K. Mima[1]

National Institute for Fusion Science, 322-6, Oroshi, Toki 509-5292, Japan
[1] Institute of Laser Eng., Osaka Univ., 2-6, Yamadaoka, Suita, 565-0871, Japan

ABSTRACT

The high energetic electron measurement is one of the most important issues to research the ignition mechanism in the Fast Ignition Realization EXperiment Project. It is also important for the energy spectra with angular distribution because the electron spread is different by the target design. Therefore we have been developed the compact Electron SpectroMeter so as to be installed on different angular potions. We have been preparing the calibration using L-band Linac in the Institute of Scientific and Industrial Research, Osaka University. The analyzer has been tested to measure energetic electrons from the aluminum plain target with 20 μm thickness irradiated by LFEX laser (maximum energy of 10 kJ) of 120 J. The maximum electron energy of 3 MeV could be observed when the laser is collimated up to 75 x 110 μm.

I. Introduction

In the laser fusion, the implosion and the central ignition of the DT micro balloon have been the most popular method to realize the inertial confinement fusion.[1] However they have large inconsistency because the efficient implosion should be performed under the low temperature, but the central ignition which is the final stage of the implosion, produces the high temperature. This means a good implosion cannot be expected near the final implosion stage. In Institute of Laser Engineering, Osaka University, the fast ignition concept which is the imploded core heating using the high energetic electron beam produced by the pulse-compressed laser, has been proposed.[2]

The high-energy electron is generated by a strong electric field based on the interaction between the high intensity laser and the pre-plasma produced by the laser pre-pulse.[3] The electron beam energy spectrum is strongly depended on the pre-plasma scale length and the main pulse intensity.[4] To obtain suitable electron energy less than several MeV for fast ignition, the pre-plasma scale length should be suppressed enough by choosing target materials, the pre-pulse control and the target area density.

In the Fast Ignition Realization EXperimental (FIREX) Project[5], the electron generated from the guided gold-cone irradiated by the heating laser, is utilized to heat the imploded core to initiate the fusion burning. The high energetic electron measurement is one of the most important issues to research the ignition mechanism. It is also important for the energy spectra with angular distribution because the electron spread is different from the target configuration. Therefore we have been developed the compact Electron SpectroMeter (ESM) so as to be set on different angular potions.

The electron spectra obtained by ESM is not reflected directly to the electron profile, which is contributed to the core heating, because the electron is decelerated by electric field due to the virtual cathode which is produced by huge electron emission.[6] Therefore low energy part less than 0.5 MeV cannot be observed due to the virtual cathode potential. However the electron spectrum included the low energy part can be obtained from the high-energy tail of the electron spectrum if we assume the Maxwellian distribution. Although the result should be compare with the result from the X-ray spectroscopy[7] or the Cherenkov radiation[8], ESM is still important tool for investigating the heating mechanism in core region.

II. ESM design

Number and size of viewing ports are limited in

Gekko XII[9] target chamber I. We use the most popular 6-inches port. All equipments should be packed within the virtual conical area created by the center target and 6 inches port flange. The triangle shape of the magnet is chosen due to the compactness and the wide energy range. We can save space since the magnet is hidden by the target chamber. The electron beam enters obliquely into the analyzer in order to obtain the wide observable energy range. Figure 1 shows the drawing of the ESM analyzer.
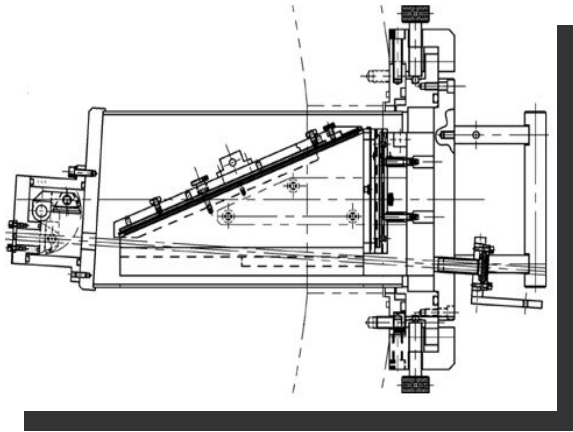
Fig.1. ESM drawing.

All equipment should be packed within the virtual conical area created by the center target and the 6 inch port flange. The triangle shaped magnet is chosen.

A neodymium alloy is used as the permanent magnet.[10] The magnet circuit is determined as to minimize the leakage of the magnetic field. Therefore small leakage of the magnetic field still remains near the top of the triangle. The two-dimensional magnetic field has been measured every 5 mm. The beam orbit has been calculated by using the observed magnetic field. The typical magnetic field strength and the magnet gap are 0.7 T and 8 mm, respectively.

The equation of motion of the relativistic electron beam is given by[11]

$$\frac{d^2 x, y}{dt^2} = \mp \frac{eB_z \sqrt{1 - (v/c)^2}}{m_0} \frac{dx, y}{dt}, \qquad (1)$$

Here, m_0, c, v, B_z, e and μ are the electron rest mass, the light speed in vacuum, the electron velocity, the magnetic field, the electron charge and the sign (minus for x and plus for y), respectively. The equation (1) is solved by using the Ruge-Kutta-Vemer method. The magnetic field at the electron position is estimated from the average of the magnetic fields on nearest mesh points. The electron beam orbits are shown in Figure 2.
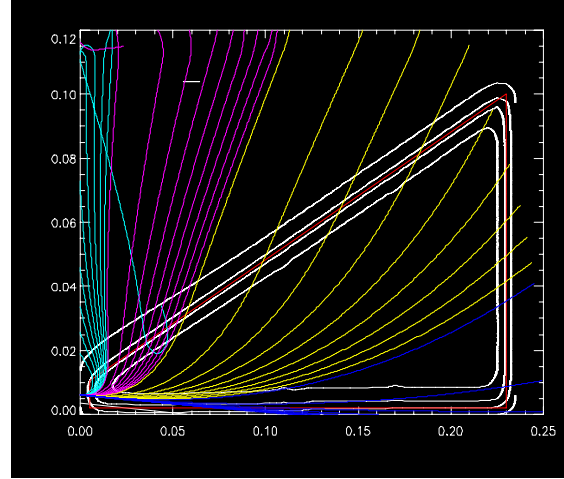
Fig.2. Electron beam orbits.
Cyan, magenta, yellow and blue lines mean 0.1-1, 1-10, 10-100,100- MeV, respectively. The red shows the magnet.

Fig.3. ESM photograph.
Total length and diameter of the main part are 30 cm and 15 cm, respectively.

The inexpensive and commercial based imaging plates (IP, Durr Dental Co.) [12] are used as the beam detector. This has merits about no electrical noise and the wide dynamic range for the intensity. Two IP folders are installed for measurements in high and low energy regions in order to extend observable energy ranges. In Table I, those holder parameters are shown. The lead X-ray shield of 3-10 cm thickness covers the IP holder to avoid strong X-ray irradiation from the target. The IP is also shielded from the lights by the shutter in the holder. The shutter is open just before the

installation. The holders with the light shield are brought to IP reader (Vista Scan, Durr Dental Co., 12.5 micron/step, 40 LP/mm) after the electron irradiation. The data have 16-bit resolution. The IP is irradiated within the 8 mm width. Therefore real signal can be obtained by subtracting signals within 8 mm width from the background in the other area of IP.

The alignment is performed from the viewing port behind the beam line and the two-dimensional adjusting mechanism. The analyzer is separated by the small gate valve so as to take out the holders without the vacuum break of the GXII target chamber. After the installation of IP, analyzer chamber is evacuated by its evacuation system up to the same vacuum level as the target chamber. Figure 3 shows the photograph of the ESM. Total length and diameter of the main part are 30 cm and 15 cm, respectively.

Table I IP holders

Cassette I	25 cm	1 – 40 MeV
Cassette II	10 cm	60 – 150 MeV

Fig.4. ESM calibration setup.

We have performed the calibration of the analyzer using L-band LINAC in the Institute of Scientific and Industrial Research, Osaka University
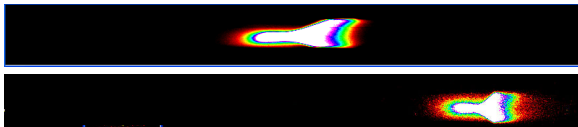
Fig.5. Beam spots on IPs.
Upper: 11MeV
Lower: 27MeV.

III. ESM calibration

The purposes of the calibration are as follows;

(a) comparison of the beam orbit with the calculation, (b) the beam intensity calibration.

We have performed the calibration of the analyzer using L-band LINAC in the Institute of Scientific and Industrial Research, Osaka University. L-and LINAC[13] has an ability of strong and ultra short pulse electron generation of maximum 91 nC and 20 ps. The calibration has been performed using single pulse at two different energy of 11 MeV, 27 MeV. Main energies and charges in the calibration were 11 MeV, 27 MeV and 16 pC, 100 pC, respectively. Electron beam from LINAC passes among air. Own vacuum chamber was prepared because the beam scattering by air should be minimized. The beam size is 5 mm at the exit of the beam line and 10 mm at 13 cm from the exit in air. The energy spreads are 0.2 MeV at 11 MeV and 0.3 MeV at 27 MeV, respectively. Figure 4 shows the photograph of the calibration system.
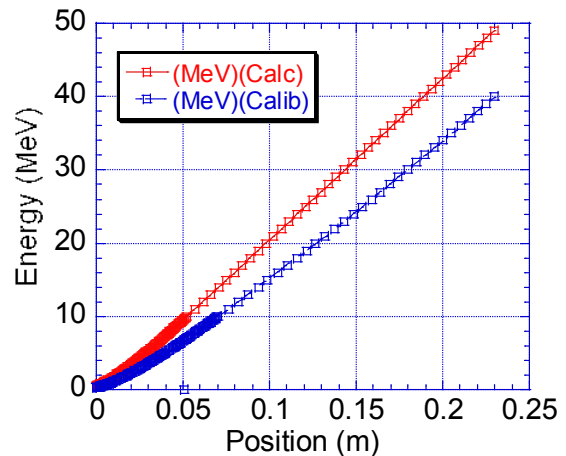
Fig.6. Energy calibration curve.
Red: Calculation
Blue: Experimental fitting by assuming the parabola-like magnetic field strength.

Fig.7. Background on IP.
The background was measured before the irradiation.

Figure 5 shows the beam patterns for 11 MeV and 27 MeV on IPs. Part of the beam hits the analyzer wall due to the beam expansion. The beam intensity, which is required for our purpose, is almost the lower limit of the LINAC. The spot position in calibration was different from that in calculation. The main reason may be due to the magnetic field leakage

near the top of the triangle. We could obtain the calibration curve from those results as shown in Fig 6. In this fitting, a magnetic field strength added parabola-like modification is assumed.

The calibration of the intensity was also obtained by comparison between the incident electrons and the counts on IP. The background (Fig.7) was measured before the irradiation. The real signal is obtained by the elimination of the background from the irradiated signal. Figure 8 shows the result of the intensity calibration.
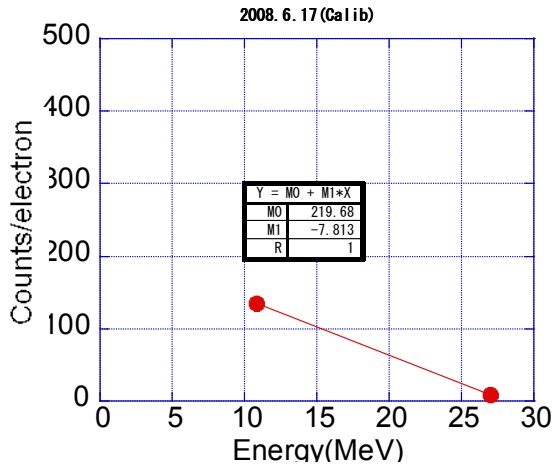
Fig.8. Intensity calibration.
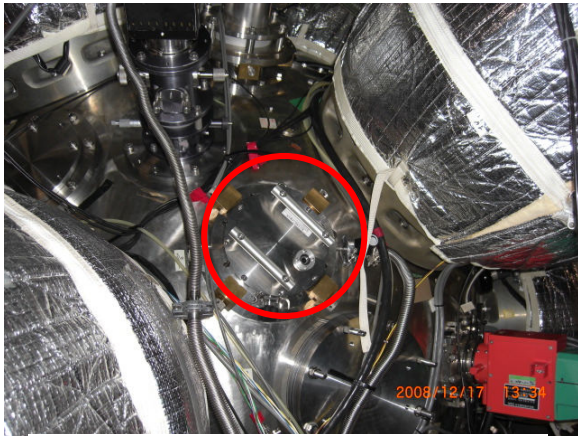
Fig.9. The photograph of the ESM installed Gekko XII.

Right upper and left lower are the laser beam ports. LFEX laser is installed on the opposite side of the ESM

IV. Aluminum target irradiated by LFEX laser

The analyzer was tested to measure energetic electrons from the aluminum plain target with 10 μm thickness irradiated by LFEX laser (maximum energy 10 kJ, the wave length of 1.05 μm, 4 beamlets)[14] with the energy of 120 J and the pulse duration of 4 ps. The analyzer was installed on the Gekko XII Target chamber I at 20.9 degrees against the laser injection direction where was at the rear side of the target. This shot has been done by compression of one beam let LFEX laser. The alignment of the analyzer was performed by viewing the dummy target (illuminated by the He-Ne laser). The maximum electron energy of 3 MeV could be observed when the LFEX laser was collimated up to 75 x 110 μm and the laser intensity of 3.5×10^{17} W/cm^2. Figure 6 shows the energy spectrum of the electron beam. The energy loss of the electron in the Al foil is written by[15]

$$-\frac{dE}{dx} = 0.306 \rho \frac{Z}{A} \beta^2 B$$

$$B = \ln\left(\frac{2m_e c^2 \beta^2}{I(1-\beta^2)}\right) - \beta^2 \qquad (2)$$

where ρ, m_e, c, Z, E, A, I and β are the target density, the electron mass, the light velocity, the target ionization number, the electron energy, the target mass number, the ionization energy and the beam velocity divided by c, respectively. The energy loss can be negligible in this energy target although it is very important in the imploded target. The electron spectrometer only detects the escaped electrons over 0.5 MeV into and the amount of the electrons observed are strongly limited by the high electrostatic potential formation by the electrons.

The irradiated IPs with ESM drawing are shown in Fig.10. The real signal is shown by the blue circle on the upper IP. The light signal circled by a red color is due to the x-ray from the target. Figure 11 shows the extended photograph of the signal on IP and the spectrum. The spectrum is obtained from the energy calibration (Fig.6) and the intensity calibration (Fig. 8). Two different plots, which are derived from the energy calibration factor and orbit calculation using measured magnetic field are shown in Fig. 6. Solid lines in Fig. 11 indicates those Maxwellian fittings as follows,[16]

$$\frac{dN}{dE} = \left(\frac{N_0}{T}\right)\left(\frac{E}{T}\right)^2 \exp\left(-\frac{E}{T}\right), \qquad (3)$$

where N, and T are the beam amount and the effective electron temperature, respectively. Here the relativistic effect is considered because the electron velocity is close to the light velocity. The effective

electron temperatures are 0.55 MeV and 0.80 MeV, respectively.
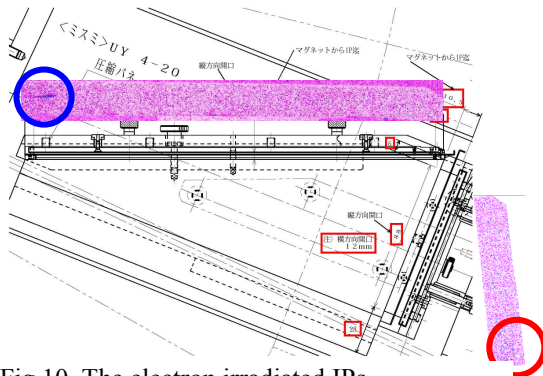
Fig.10. The electron irradiated IPs.
Upper: Lower energy range,
Lower: High energy range.
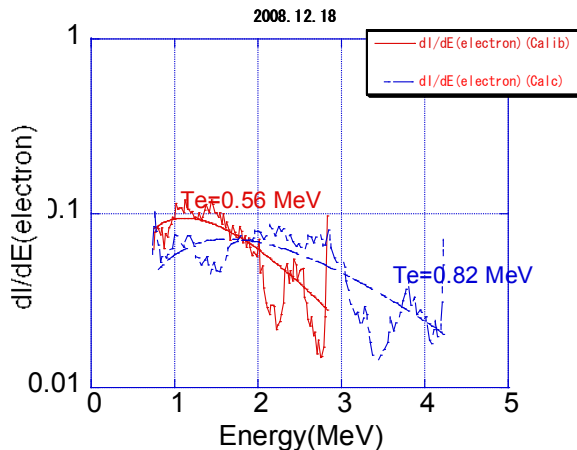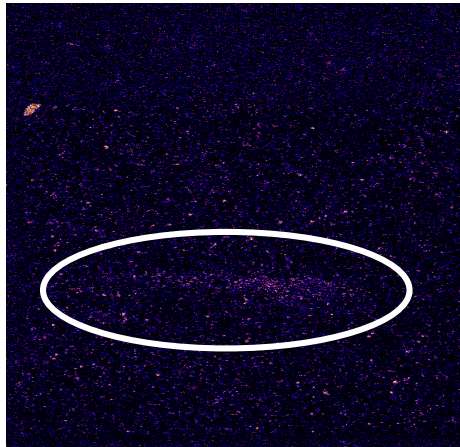
Fig.11.The spectrum.
Upper: the photograph of the signal,
Lower: spectrum.

pulse compression system of LFEX laser was successfully completed.

In different shot, we can obtain the spectrum as shown in Fig. 12. In this shot, the LFEX laser with energy of 100 J and duration of 4ps is collimated to two spots of 24.5 μm x 44.1 μm and 24.5n μm x 29.4 μm. The total power is 1.4 x 10^{18} W/cm^2. The relation between the effective electron temperature and the laser beam intensity is known as the scaling driven semi-empirically.[17]

$$T_e(MeV) = 0.4 \times \left[\left(\frac{I_L(W/cm^2)}{10^{18}} \right) \lambda(\mu m)^2 \right]^{1/3}$$

(4)

where T_e and I_L are the effective electron temperature and the laser beam intensity, respectively. Figure 13 shows the comparison between the experimental temperature and the empirical temperature.

V. Summary

The high energetic electron measurement is one of the most important issues to research the ignition mechanism. We have been developed the compact Electron SpectroMeter so as to be set on different angular potions. ESM is calibrated by using L-band Linac in the Institute of Scientific and Industrial Research, Osaka University. The analyzer was tested to measure energetic electrons from the aluminum plain target irradiated by LFEX laser.

A fast ignition integrated experiment using the imploded core by Gekko XII and the additional heating by LFEX laser has been planed from May 2009. The energy spectral measurement of the electrons from the guided cone can be expected to investigate the heating mechanism.

References
1) H.Azechi, et al, "High density compression experiments at ILE, Osaka. Laser Part. Beams 9, 193-207 (1991).
2) R. Kodama, et al, "Fast heating of ultrahigh-density plasma as a step towards laser fusion ignition", Nature 412, 789-802 (2001).
3) M. Key, et al. Hot electron production and heating by hot electrons in fast ignitor research. Phys. Plasmas 5, 1966-1972 (1998).
4) T. Tajima and J. M. Dawson, "Laser Electron AcceleratorPhys. Rev. Lett. 43, 267 - 270 (1979)
5) H. Azechi, "Present status of the FIREX programme for the demonstration of ignition and burn", Plasma Phys. Control. Fusion Vol. 48, pp. B267－B275 2006.12.
6) Private communication.
7) Private communication.
8) J. Zheng, et al., "Cherenkov radiation generated by a beam of electrons revisited", Phys. Plasmas 12, 093105 (2005).

9) C. Yamanaka, et al., proc. 10th Int Conf. London 1984) vol3., IAEA Vienna (1985) 3.

10) Private communication.

11) Private communication.

12) http://www.duerr.de/

13) http://www.sanken.osaka-u.ac.jp/labs/rl/facility.html

14) N. MIYANAGA, et al., in Proc. of IFSA'03, ThF1.1 (2003).

15) Private communication.

16) T. Phillips, et al., "Diagnosing hot electron production by short pulse, high intensity lasers using photonuclear reactions", Rev. Sci. Instrum., 70 1213 (1999).

17) Private communication.
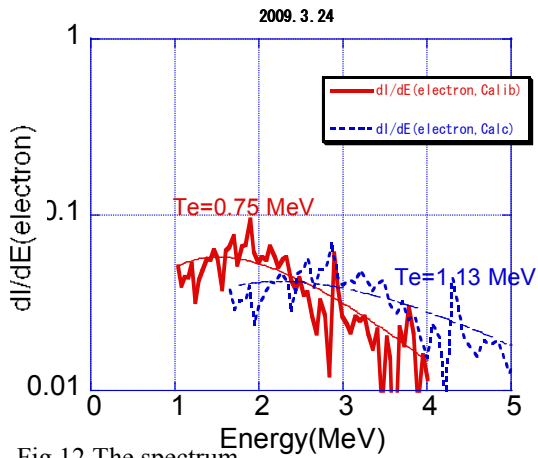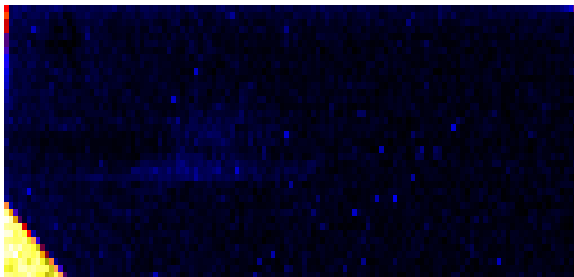
$Te(MeV)=0.4 \times \{I(W/cm^2)/10^{18} \times \lambda(\mu m)^2\}^{1/3}$

Fig. 13. Comparison between the experimental temperature and the empirical temperature.

Fig.12. The spectrum.
Upper: the photograph of the signal,
Lower: spectrum.
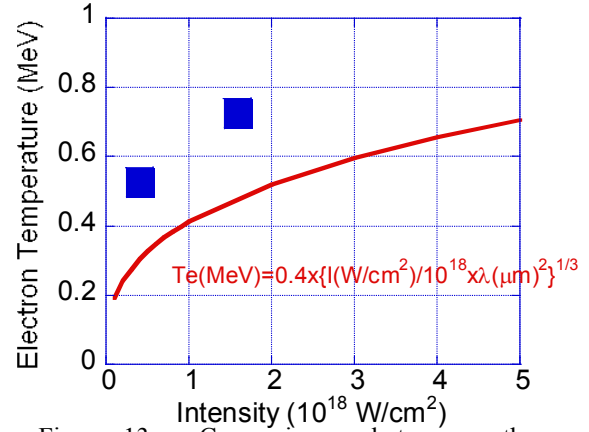
EXPERIMENTAL STUDY ON FREE ELECTRON MASER USING ADVANCED BRAGG RESONATOR

Shuhei Odawara, Fumichika Kondo, Kaori Tamura, Yukihiro Soga
Keiichi Kamada and Naum S. Ginzburg [a]

Graduate School of Science and Technology, Kanazawa University,
Kanazawa, Ishikawa, 920-1192, JAPAN
[a]*Institute of Applied Physics, Russian Academy of Sciences, Nizhny Novgorod,*
603600, Russia

ABSTRACT

New scheme of intense high frequency electromagnetic wave source using an intense relativistic electron beam was proposed and designed. Free electron MASER with an advanced Bragg resonator has an advantage of the frequency selectivity to that with the normal Bragg resonator. An electromagnetic wave with quasi-cutoff frequency is trapped in the advanced Bragg mirror and couples with the propagating wave. The higher frequency selectivity like gyrotron is expected. A proof of principle experiment of the advanced Bragg resonator using an intense relativistic electron beam had started.

I. Introduction

Because of the lack of appropriate radiation sources, the frequency range of 0.1-10 THz is called THz gap. THz gap lies between the upper frequency of classical electromagnetism (electron tubes) and the lower frequency of quantum electronics (LASER). There are three candidates for THz sources, i.e. LASER, large accelerators and electron tubes. THz sources using LASER and large accelerator are developed in advance of those using electron tubes. However, for the practical use, THz source is requested to be compact size, DC operation with output power over 1 W. In this point of view, electron tubes are expected to achieve more convenient powerful THz sources[1-3].

Gyrotron is the most developed electron tube for THz source. The selectivity of the frequency is excellent because the quasi-cutoff frequency was used. The problem for the

Gyrotron for THz source is that the magnetic field over 20 T is necessary to increase the frequency in sub-millimeter range. To solve this problem, new ideas, for example large orbit gyrotron(LOG) etc., are now strongly developed[4]. One of the other candidates of THz source among electron tubes is the free electron maser (FEM). One of the problems for the FEM is the low frequency selectivity. Bragg mirrors are utilized as mirrors in the optical distributed feedback LASER (Fig.1)[5,6]. Many successful results of narrow band FEM are obtained by using the Bragg mirror in mm waveband [7,8]. However, as the frequency increases, the traditional Bragg mirror loses the selective features over transverse indexes. An advanced Bragg resonator (ABR) was proposed by Ginzburg[9]. It utilizes the interaction between a propagating wave and a quasi-cutoff mode to
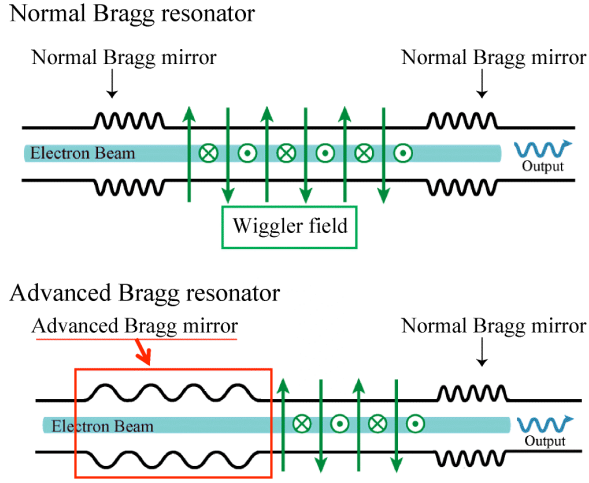
Fig. 1. Schematics of the normal(upper) and advanced(lower)   Bragg resonator.

provide a higher selectivity over the transverse index than a normal Bragg resonator.

The goal of our experiment is to clear the advantage of the newly proposed advanced Bragg resonator. We have no experimental result on ABR   yet.   In this paper, we report the preliminary experimental results of FEM radiation and the design and simulation of normal Bragg resonator.

2. Advanced Bragg resonator.

In the previous scheme, an ABR is located alone at the center of the helical wiggler coil [10]. However, it is predicted by the computer simulation that the Ohmic loss in the ABR used above situation is not negligible. We changed to use the ABR as the entrance mirror as shown in Fig. 1.   At the exit side the normal Bragg mirror is utilized. From now on, the entrance mirror is named an advanced Bragg mirror and the total system including the advanced and the normal Bragg mirror is called advanced Bragg resonator (ABR). An

injected electron beam interacts with the traveling wave at the middle of both mirrors. The normal Bragg mirror reflects the radiated wave with its designed frequency to the upstream side of the drift tube. The advanced Bragg mirror reflects the wave only interacting with its cutoff frequency to the downstream side of the drift tube, so that the higher frequency selectivity is realized by the ABR.

3. Experimental setup.

In Fig. 2, the schematic of the experimental setup is shown. An intense relativistic electron beam (IREB) with energy of around 720keV, current of 200 A and the radius of 3 mm was injected into the drift tube with diameter of 20mm. As a liquid resister was set parallel to the diode as a shunt register to prevent the output impedance for the pulse line from decrease in time, the diode voltage was kept constant during 120 ns as shown in Fig. 3. The energy spread of the IREB was measured to be 720 ± 22 keV by a magnetic momentum analyzer, as shown in Fig. 3. An axial magnet field (Bg) up to 1T was applied by two solenoid coils.   A helical wiggler coil located inside a solenoid coil provided a periodic radial
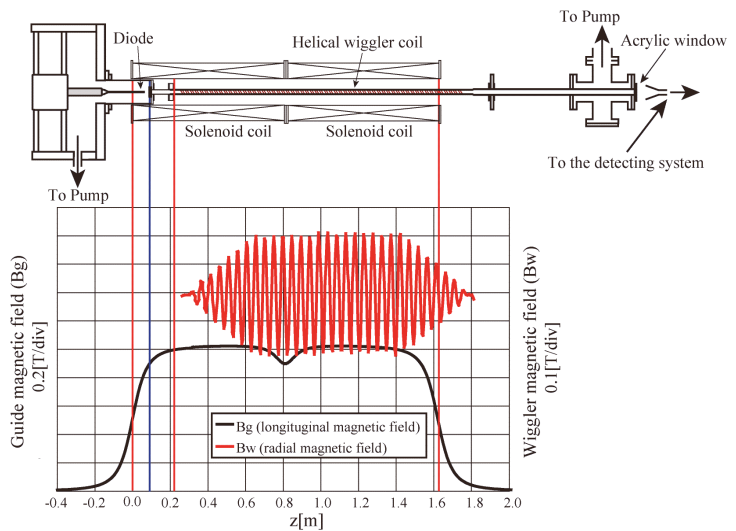
Fig. 2.   Experimental setup
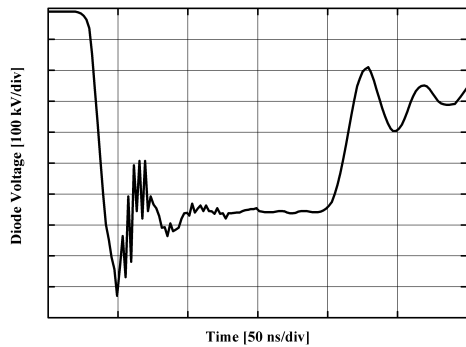
Fig. 3.   Typical diode voltage waveforms.

Fig. 4.   Radiation signals without Bragg resonator. The strength of the radial periodical magnetic field was changed.

Fig. 5. Radiation signals without Bragg resonator.   The strength of the axial magnetic field was changed.

magnetic field (Bw) up to 0.16 T. The axial positions of the strengths of the axial and periodical magnetic field are shown in Fig. 2. The IREB was diverged to the wall at the exit of the axial magnetic field.   A horn antenna was set just behind the acrylic window to observe the radiated electromagnetic wave. The electromagnetic wave was detected through 3 band pass filters, with frequency of 26-31, 30.5-35.7 and 35.5-40 GHz, and high pass filter over 40 GHz. Attenuators were set at each branch. As the FEL radiation with the frequencies of 53.9 and 48.7 GHz were expected with our experimental conditions, simple high pass filters which are made by metal disks with various diameter holes at the center are utilized to check the radiated frequency roughly.

4. Experimental results.

At first, no Bragg resonator was used. An IREB with energy of 720 keV was injected into the cylindrical tube immersed in the helical and the axial magnetic field.   The signals of radiation over 40 GHz were shown in Fig. 4. In this figure, the upper waveform indicated the diode voltage. The radiation signals (lower) with various strengths of the wiggler magnetic field
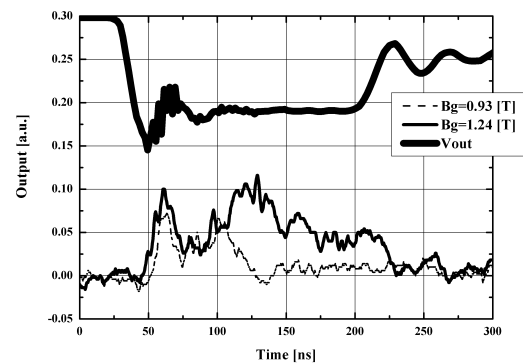
(Bw) are plotted. When the strength of the wiggler magnetic field was changed, the

Fig.6.   High pass filters.

94

radiation power was not changed. Though the beam current and the energy were not changed by the axial magnetic field with the strength of 0.5-1.2 T, the radiation power was changed by the strength of the axial magnetic field as shown in Fig. 5. It was suspected that the radiation from the cyclotron mode was observed and the FEM radiation was covered by the cyclotron radiation.

Simple high pass filters as shown in Fig. 6 were designed to observe the FEM radiation.
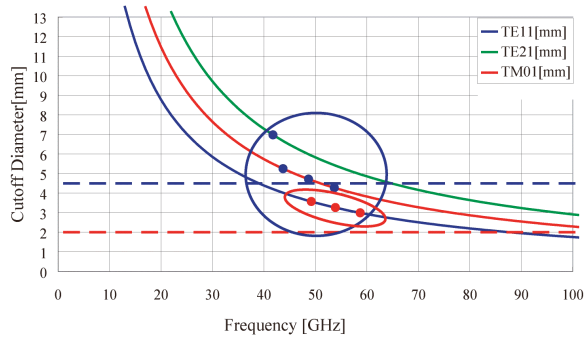
Fig.7. Diameter of the figh pass filters vs cutoff frequency for each radiation mode. Filled circles are the expected radiation frequencies for our experimental conditions.
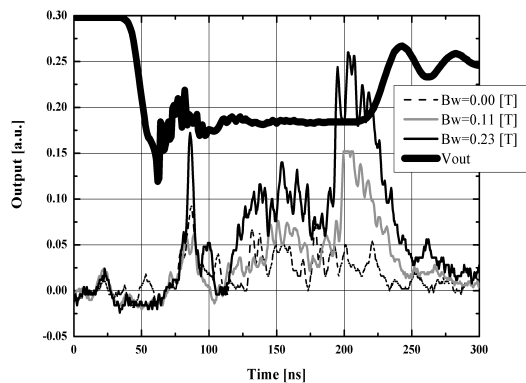
Fig. 8. Radiation signals without Bragg resonator using high pass filter with diameter of 4.5 mm. The strength of the radial periodical magnetic field was changed.

In Fig. 7, the cutoff frequencies of each radiation mode were plotted against the diameters of the hole. The cyclotron radiation cannot pass through a hole with diameter less than 7 mm.

The detected output power of radiation with a high pass filter with diameter of 4.5 mm was shown in Fig. 8. We notice that the radiation started to grow after 110 ns in Fig. 8, as the theoretical prediction of the growth time for FEM was around 100 ns. The radiation power was increased as the strength of the wiggler field was increased. In this case, the radiation power was not changed by the axial magnetic field. And the radiation power was not observed when the wiggler field was not applied. So that, we concluded that the FEL radiation was observed. The mode was estimated to be 54 GHz TE_{11} mode.

There left problems of reproducibility of the radiation. And the output power was roughly estimated to be less than 1 MW. We have not solved this problem yet.

5. Design of the normal Bragg Mirror.

A normal Bragg mirror for the frequency of 54 GHz was designed based on the mode coupling theory[11,12]. The length, the radius and the depth of corrugation were calculated to find the appropriate values for the 54 GHz TE_{11} mode.

For example, the calculated result of the
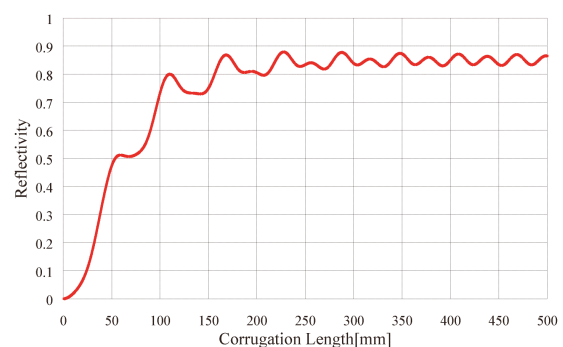
Fig. 9. Mirror length vs reflectivity for TE_{11} mode.

relation between the reflectivity and the length

of the normal Bragg mirror is shown in Fig. 9. A normal Bragg mirror was divided into several parts because of the engineering problems. Therefore, the length of the normal Bragg mirror was decided to be 151.4 mm.

As a result, the calculated reflectivity for 54 GHz, TE_{11} mode with reasonable parameters was shown in Fig. 10. The resolution of the frequency was expected to be around 1 GHz.
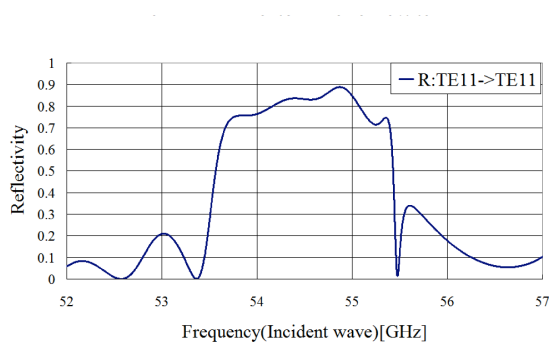
Fig. 10. Frequency vs reflectivity for 54 GHz TE_{11} mode.

6. Conclusion.

We are on the way to the proof of principle experiment of the advanced Bragg resonator. We obtained the experimental results of FEM radiation with a helical wiggler coil using an intense relativistic electron beam. We will continue the experiments to increase the output power of FEL radiation. The advanced Bragg mirrors are now designed and simulated.

References

1) P. H. Siegel, "Terahertz Technology", IEEE Trans. on Microwave Theory Tech. **50**, 910-927 (2002)

2) G. P. Gallerano, and S. Biedron, "OVERVIEW OF TERAHERTZ RADIATION SOURCES", Proceeding of the 2004 FEL Conference, 216-221 (2004)

3) V. L. Bratman, "MILLIMETER-WAVE RELATIVISTIC ELECTRON DEVICES", Radiophys. Quantum Electron., **46**, 769-781 (2003)

4) T. Idehara, H. Tsutiya, La. Agusu, H. Mori, H. Murase, T. Saito, I. Ogawa, and S. Mitsudo, "The 1 THz Gyrotron at Fukui University", Infrared and Millimeter Waves, 2007 and the 2007 15th International Conference on Terahertz Electronics. IRMMW-THz. Joint 32nd International Conference 2-9 Sept. 2007 309 - 311

5) V. L. Bratman, G. G. Denisov, N. S. Ginzburg, and M. I. Petelin, "FEL's with Bragg Reflection Resonators: Cyclotron Autoresonance Masers Versus Ubitrons", IEEE J. Quantum Electron., **19**, 282-296 (1983)

6) C. K. Chong, D. B. McDermott, M. M. Razeghi, N. C. Luhmann, Jr., J. Pretterebner, D. Wagner, M. Thumm, M. Caplan, and B. Kulke, "Bragg Reflectors", IEEE Trans. on Plasma Sci., **20**, 393-402 (1992)

7) T. S. Chu, F. V. Hartemann, B. G. Danly, and R. J. Temkin, "Single-Mode Operation of a Bragg Free-Electron Maser Oscillator", Phys. Rev. Lett., **72**, 2391-2394 (1994)

8) J. Chen, M. C. Wang, Z. Wang, Z. Lu, L. Zhang, and B. Feng, "Study of a Raman Free-Electron Laser Oscillator with Bragg Reflection Resonators", IEEE J. Quantum Electron., **27**, 488-495 (1991)

9) N. S. Ginzburg, A. M. Malkin, N. Yu. Peskov, A. S. Sergeev, A. K. Kaminsky, S. N. Sedykh, E. A. Perelshtein, A. P. Sergeev, A. V. Elzhow, "Improving selectivity of free electron maser with 1D Bragg resonator using coupling of propagating and trapped waves", Phys. Rev. Special topics accelerators and beams, **8**,

040705 (2005)

10) K. T. McDonald 'The Helical Wiggler', Joseph Henry Laboratories, Princeton University, NJ 08544 (Oct. 12, 1986).

11) L. Solymar 'Spurious Mode Generation in Nonuniform Waveguide' R.E. Trans. MTT-7, No.3 (1959).

12) G. Reiter'Genelized Telegraphist's Equation for Waveguide of Varying Cross-section', The Institution of Electrical Engineers Paper No.3028E (1 959)